UNIVERSITÀ
DEGLI STUDI
DI PADOVA

Sede Amministrativa: Università degli Studi di Padova

DIPARTIMENTO DI GEOSCIENZE

SCUOLA DI DOTTORATO DI RICERCA IN SCIENZE DELLA TERRA

CICLO XXV

THE SURFACE OF MERCURY:
INTERPRETING REMOTE SENSING IMAGES AND SPECTRAL SIGNATURES

Direttore della Scuola: Ch.mo Prof. Massimiliano Zattin

Supervisore: Dott. Matteo Massironi

Co-supervisore: Ch.mo Prof. Fabrizio Nestola

Dottorando: Sabrina Ferrari

THE SURFACE OF MERCURY: INTERPRETING REMOTE SENSING IMAGES AND SPECTRAL SIGNATURES.

Ph.D. candidate: SABRINA FERRARI, III Cycle: XXV
Supervisor: Doc. MATTEO MASSIRONI Prof. FABRIZIO NESTOLA

Abstract

Knowing the evolution and composition of the surface of Mercury enables us to discern several processes that operated during the formation of the inner Solar System (e.g. crustal accretion, impact gardening and global cooling of Terrestrial Planets). The elaboration and classification of remote sensing multi-band images allowed the interpretation of the stratigraphy, composition, age and structural evolution of Rembrandt basin and scarp system, i.e. the largest impact basin cross-cutting by contractional structure of the southern hemisphere of Mercury. The interaction of different scale processes has been demonstrated. Since the knowledge of the surface composition of Mercury is based on the interpretation of spectra, Thermal Infra-Red spectra of representative mineral phases have been measured in laboratory at the temperatures of the planetary surface. Significant changes in the high temperature spectra have been detected. Failure to allow for these effects leads to errors in the estimation of chemical compositions by Infra-Red spectra.

Conoscere l'evoluzione e la composizione della superficie di Mercurio permette di distinguere i diversi processi che hanno operato durante la formazione del Sistema Solare interno (es. accrezione crostale, eventi d'impatto e raffreddamento globale dei Pianeti Terrestri). L'elaborazione e classificazione di immagini multi-banda riprese in remoto ha permesso l'interpretazione della stratigrafia, composizione, età ed evoluzione strutturale del sistema composito bacino d'impatto - scarpata chiamato Rembrandt, ovvero il più grande bacino riconosciuto nell'emisfero meridionale di Mercurio tagliato da una scarpata contrazionale. In questo lavoro si dimostrano l'esistenza ed interazione di processi di differente entità sulla stessa area. Dato che la conoscenza della composizione della superficie di Mercurio si basa sull'interpretazione di spettri, in laboratorio sono stati misurati spettri nel campo d'infra-rosso termico per un set di minerali rappresentativi riscaldati a temperature verosimili per la superficie del pianeta, evidenziando notevoli variazioni delle bande caratteristiche rispetto agli spettri misurati comunemente a 25 °C.

1. Introduction

Knowing the evolution of the terrestrial bodies of our Solar System is one of the main focuses for a Planetary Geologist. The most productive approach to obtain an account is beginning with the present state of the Solar System and trying to work backward in time. It generally implies direct observation on Earth and remote observation on faraway terrestrial bodies, inferring their composition, interior properties, exterior environment and still active processes, even providing geological maps useful to fix the sequences of events. Comparing different settings, it is possible to reconstruct the primitive scenario of the Solar System and what were the shallow and deeper processes ruling the differentiation of the terrestrial bodies, as well as their consequent individual development. Nowadays, we can obtain remote information employing ground-base telescopes or committed space probes, which sometimes are able to return samples. At the same time, the development of modern laboratories has allowed us to simulate environments completely different from the Earth's one, obtaining additional information on possible planetary processes and helping to focus the aims of new missions.

In this frame, the knowledge of small less evolved bodies like Mercury represents a standard for the knowledge of the early terrestrial planets history, which very little is known yet. More in general, the geological history of Mercury can explain the roles of planet size and solar distance as governors of magmatic and tectonic history for a terrestrial planet. At this propose, contributes of this work would be interpreting products provided both by current space probe and laboratory simulations. Methods considered here involved (i) the elaboration and interpretation of remote sensing images provided by the on-going National Aeronautics and Space Administration (NASA) MErcury Surface, Space ENvironment, GEochemistry (MESSENGER) mission, and (ii) the interpretation of silicate Thermal Infra-Red spectra collected reproducing the surface environment of Mercury (i.e. low pressure and strongly variable temperatures), in order to provide suitable analogs for next planned mission on Mercury, named BepiColombo.

** Product of the collaboration of the European Space Agency (ESA) with the Japanese Space Agency (JAXA).*

1.1 Mercury: an overview

Mercury is the smallest planet of the Solar System and the closest to the Sun, undergoing to the highest daily temperature excursion among the Terrestrial Bodies. It has also the highest uncompressed density of 5.3 Mg/m^3, which means that it must have a large component of iron. Chapman (1988) defined it as an "end-member" planet, adding that it exists in the most intense solar radiation environment and is most affected by solar tides: "... of all the planets, its present geochemistry may be the most modified, by catastrophic processes, from its primordial state".

The observations of Mercury by Earth-based telescopes have always been difficult. Until the first exploration the planet was considered much like the Moon, except for its proximity to the Sun and the unusual rotational geometry of two-thirds of its 88-days/yr. Then it was explored for the first time in the '70s by NASA Mariner10 mission. The spacecraft completed three flybys of the planet (1974-1975), imaging about 45% of the its surface at an average spatial resolution of 1 km, revealing the internal magnetic field and studying both the tenuous atmosphere and the physical characteristics of the surface materials (Murray 1975, and reference therein). Over the imaged hemisphere, a rock-stratigraphic classification allowed to construct a geological time scale of Mercury (Fig. 1.1, Spudis and Guest 1988) that define a context for the occurrence of all the surface geological activities. The mapping revealed several landforms called *lobate scarps*, which have been interpreted as expression of surface-breaking thrust faults caused by horizontal contraction (e.g., Strom et al. 1975; Dzurisin 1978; Melosh and McKinnon 1988; Watters et al. 1998, 2004; Watters and Nimmo 2010) and allowed the estimate of decrease in planet's radius and the modeling of the elastic lithosphere (see below).

With Mariner10 results, the high inferred uncompressed density has been justified with a high iron core content, which might reach 2/3 of the core mass if alloyed with a light element as sulfur (Harder and Schubert 2001), overlaid by a 600-km-thick rocky shell. Such a metallic mass fraction is at least twice that of the other Terrestrial Planets, raising questions on what was its formational process. At this propose, three models have been put forward: (i) the impoverishment of silicate particles by aerodynamic drag during the planetesimal accretion (Weidenshilling 1978), (ii) the preferential vaporization of silicates by hot-nebula radiations and the removal by strong solar wind (Fegley and Cameron 1987), and (iii) the selective removal of silicate due to a giant impact (Benz et al. 1988). All these hypotheses lead to different predictions for the bulk chemistry of the silicate fraction, hence determining the bulk chemistry offers an opportunity to discern those processes operating during the formation of the inner Solar System that had the greatest influence on producing the distinct compositions of Mercury (Solomon et al. 2007).

The surface composition, however, remained unconstrained beyond the Mariner10 contribution (Boynton et al. 2007). The most significant compositional information derived from ground-based spectra, which showed an average content of FeO lower than 3-4 weight percent (Vilas 1985; Warell et al. 2006; Blewett et al. 2007) and significant variations depending on the longitude (Sprague et al 2002, 2009). In particular, Sprague et al. (2009) found generally Fe-poor, Mg-rich chemistries and intermediate, mafic and ultramafic rock compositions, K-spars, Na-bearing plagioclase and Ca-rich pyroxenes.

Despite the predicted poor iron content, Mercury on average appeared 10-15% darker than the near-side Moon (Warell et al. 2006).

1.1.1 Nature of the surface of Mercury

After three flybys and almost two years of orbital records, the MESSENGER mission has reassessed the dimensions and the physical properties of the Mercury's core, and has documented the structural and compositional variations of the Mercury's crust, relating them to the main activities of the planet (volcanism, tectonism and impact cratering).

The interpretation of spectra provided by different MESSENGER instruments (i.e. X-ray spectra, Gamma-ray spectra and Visible/Near Infra-Red spectra) has confirmed the poor iron content of the surface of Mercury as compared to other rocky planets, but has also revealed 10 times the sulfur content of Earth's rock (Nittler et al. 2011) and a certain abundance of another volatile element as potassium (Peplowsky et al. 2011). These results eliminate each high-temperature formation theories that imply the removal of the volatile content from the surface of Mercury. The radioactive elements content detected by the MESSENGER gamma-ray spectrometer is comparable to that of the chondritic meteorites, suggesting that Mercury could have been build up of the same material as the other Terrestrial Planets. In addition, MESSENGER inference of the gravity field (Smith et al. 2012) suggests that Mercury's solid outer shell may be no more than 400 km thick (vs. 600 km thick of Mariner10 deductions). Those constrain on the chemistry and on the thickness of the silicate fraction (Fig. 1.2) influence the volcanic and tectonic activities of the planet.

1.2.2 Geological processes of the surface of Mercury

The early intense impact gardening and tectonism and a slightly younger widespread volcanic activity are among the main surface geological processes detected by space missions on Mercury. At this regards, the well-preserved heavily cratered terrain of Mercury was highlighted by Mariner10 images (Trask and Guest 1975). Although during the first 0.5 Ga of their history all the terrestrial bodies underwent to a high cratering rate period (Late Heavy Bombardment, ending 3.8 Ga ago), only a few of them have preserved the heavily cratered surface. That period has been proven for the Moon, for which age dating of returned rock samples permitted the establishment of a relationship between crater density and age: the Lunar radiometric chronologies together with the crater-size distributions mapped on the surface have provided the basis for deriving the impactors flux and then estimate the crater-size distributions of other well-preserved cratered surfaces as that of Mercury (Neukum et al. 2001a).

The cratered terrains share the surface of Mercury with a widespread volcanic overlay, recently identified by MESSENGER (Denevi et al. 2009, Head et al. 2011). Extensive evidence of volcanic origin for many plains deposits have been recognized (Head et al. 2009) and the volcanic activity, commonly thought to be favoured by the intense cratering of the Late Heavy Bombardment, seems to have more recent relative ages (Prockter et al. 2010).

The prediction made on the basis of Mariner 10 observations that tectonic deformation has been dominated by horizontal shortening has been confirmed by Watters et al. (2009a) on MESSENGER data. The shrinkage of the planet localized along foreland-thrust belts (FTB), which border blocks of high topography and thick crust (Byrne et al. 2102a). The main responsible for this large-scale crustal deformation seems to be the contraction due to the cooling of the planet's interior and the growth over time of the solid inner core, though a coexistence with other global mechanisms (e.g. tidal despinning and mantle convection) is very plausible (Dombard and Hauck 2008; King et al. 2008). In parallel, the excavation and crustal flow induced by giant impacts might have been able to condition those global and regional stress fields (Spudis and Guest 1988; Fleitout and Thomas 1982; Watters et al. 2005). In turn, the basin's volcanic infilling underwent both to subsidence, global contraction, and intrinsic thermal cooling, forming basin-oriented tectonic patterns (Watters et al. 2012a, Byrne et al. 2013). Indeed, whereas Mariner 10 was not able to view even half of the basin, MESSENGER has now seen the 1500-km-diameter Caloris basin feature in its entirety, documenting how its formation was followed by the widespread emplacement and subsequent deformation of volcanic plains within and exterior to the basin.

Next BepiColombo mission to Mercury (Benkhoff et al. 2010) will launch two different satellites in order to complete the database of Mercury. The module dedicated to probe the surface (Mercury Planetary Orbiter, MPO) will be launch in 2015, carrying on both the SYMBIO-SYS payload (Benkhoff et al. 2010), constituted by three different channels for stereoscopic, high-resolution, hyperspectral observation, and a Thermal Infra-Red spectrometer coupled with a radiometer (Mercury Radiometer and Thermal Infra-red Spectrometer, MERTIS, Helbert et al. 2005, Hiesinger and Helbert 2010). These instruments will be particularly useful to profoundly investigate the geophysical and geochemical properties of the surface of Mercury, helping to solve the still open questions of Mercury.

1.3 The surface of Mercury: still open questions

Insights offered by MESSENGER during the last three years have allowed reassessing shape and dimensions of the planet, unraveling the great extension of volcanism and in general incrementing each statistics of surface features, and proposing brand new compositions for the surface.

Detailed mapping based on MESSENGER MDIS mosaics, instead, currently allow reconstructing the regional stratigraphy and dating the involved units, attempting to understand for how long Mercury was tectonically and volcanically active. The contraction due to the cooling of the planet acting by the end of the Late Heavy Bombardment (3.9 Ga ago), for example, has been considered for long time the main cause of tectonism recorded on the surface of Mercury. This contraction implied a decline of the planetary radius that can be estimated by the discernment and measurement of the surface tectonic structures. Before the MESSENGER update, the cumulative length of all the mapped scarps (e.g., Watters et al. 1998) supported a decrease in the planet's radius that never reached the predictions proposed by thermo-mechanical models (e.g., Hauck et al. 2004, Dombard and Hauck 2008), suggesting that the potential for other mechanisms to generate contraction (e.g., despinning acting prior

to the end of the Late Heavy Bombardment) and then accommodate contraction (e.g. long-wavelength lithospheric folds) remained untested, or at least that several lobate scarps remained unknown. Recent works (Watters et al. 2012b, Di Achille et al. 2012) have notably increased the global contractional strain, taking into account several additional features detected on MESSENGER data. However, the resulting limited amounts of radius decrease (0.7-3 km calculated vs. ~5 km predicted) force models to apply a refractory composition that seems to be incompatible with the amount of volatiles necessary to form the pyroclastic deposits detected by MESSENGER (Kerber et al. 2011). In addition, under those constrain, models predicted an early cessation of crustal production, whereas volcanic activity proposed by MESSENGER appears to last over any other surface activity (Head et al. 2009, 2011). A new update of the Mercury's global tectonic map (e.g. Watters et al. 2012b) and the identification of patterns and kinematics of the mapped structures could place constraints both on the timing and amount of each tectonic activity and consequently on the thermo-chemical evolution of the planet. Seemingly, dating the recognized geological units could help to confine both volcanic and tectonic activities.

On the other hand, spectroscopy remains the useful method to investigate the surface composition. The current knowledge is based on the interpretation of spectra provided by MESSENGER (e.g. Visible and Near Infra-Red spectra, X-ray spectra and Gamma-ray spectra). BepiColombo, as mentioned, will carry on board the Mercury Radiometer and Thermal Infrared Spectrometer (MERTIS) (Helbert et al. 2005, Hiesinger and Helbert, 2010) that will be able to provide spectra from 7 to 14 μm. This range of wavelength is very effectively to identify the fine-scale structural properties of silicates, allowing a good interpretation of most of minerals. For the time being, the Thermal Infra-Red (TIR) spectra of the surface of Mercury are provided by ground-based telescopes and airborne instruments capable of getting above much of the Earth's atmosphere, and then regard only circumscribed locations on that surface. The interpretation of these spectra suggested the presence of feldspar, pyroxenes and possibly olivines (e.g., Emery et al. 1998; Sprague et al. 2000, 2002, 2009). However, these interpretations seem to neglect the possible effect of thermal gradients on spectra of particulates measured in vacuum (Hamilton 2010), as long as the possible effects induced on those particulates by the extreme daily temperature range that the surface of Mercury experiences. Hence, the investigation of the behaviour of minerals under the most likely environment of the surface of Mercury should be currently a priority.

1.2 A multiple approach for still open questions

During its second and third flybys, the Mercury Dual Imaging System (MDIS) (Hawkins et al., 2007) of MESSENGER imaged a previously unseen, well-preserved basin named Rembrandt in Mercury's southern hemisphere. With a diameter of 715 km, Rembrandt is among the largest and youngest impact basins recognized on Mercury (Watters et al. 2009b; Fassett et al. 2012). Its interior is partially resurfaced by smooth plains interpreted to be of volcanic origin (Denevi et al., 2009) and is crossed by a 1000-km-long reverse fault system (Watters et al., 2009a; Byrne et al., 2012a). Notably, the Rembrandt basin area recorded most of the activities that modified the surface of Mercury (e.g. basins formation and impact gardening, global and basin-related tectonics

and resurfacing) and represents a good case study for understanding length and sequence of such processes. The further recognition of unusual kinematic indicators of strike-slip motion along the cited fault system (Massironi et al., 2012) motivated a more detailed work focused on the complex relationships between the Rembrandt basin and the scarp. To this end, MESSENGER MDIS mosaics and derived Digital Terrain Models (Preusker et al., 2011) have been used to map in fine detail the basin units and the structures of Rembrandt Basin area, in order to obtain better insight in the kinematic development of the Rembrandt scarp system and whether its development was influenced by the interaction between global- and basin-scale processes. Then, crater counts have been performed on each unit, in order to estimate the ages by applying the Model Production Function (MPF) of Marchi et al. (2009). The dataset has been constantly integrated with fresh images thus the morphological interpretations have been ever-improved.

As modeled by Vasavada et al. (1999) and Bauch et al. (2011), the temperature of the surface of Mercury can range in 44 earth-days between 70 and 725 K. Assuming that such variations can cause significant crystal structure changes, X-ray diffraction and Thermal Infra-Red spectroscopy have been conducted in laboratory in order to verify the influence of the thermal expansion on the spectral signatures. The range of wavelength considered in laboratory (7-14 μm) is the same that will be investigated by MERTIS on the surface of Mercury. As mentioned, this range is functional to identify the fine-scale structural properties of silicates (e.g. stretching and bending motions in the silicon-oxygen anions, metal-oxygen and lattice vibrations, Hamilton, 2010 and reference therein). In addition, for mineral families as olivines and pyroxenes, the emissivity peak positions are diagnostic of the composition. All these properties, well-studied at Earth ambient conditions, should be strongly influenced by thermal expansion induced by variations of temperature on minerals, modifying their characteristic spectra. To provide an example, starting from the available density data on olivine, an increase of temperature by 700 K causes the same increase in density of that caused by an increase by 30% of iron. This could drive to important misinterpretations and limit our capability of inferring compositions and rheological properties of materials from remote sensing acquisition. Then measures of crystal lattice and spectra have been collected in vacuum, up to 725 K on minerals assumed to be present on the Mercury surface (Warell et al., 2010). The main purpose of this multi-methodological approach is highlight the spectral variations occurred on the heat-treated samples that could induce to misinterpretation of their chemical composition. In this research project single mineral phases will be investigated with the aim to monitor how their specific spectral features change as a function of temperature. The simultaneous presence of different minerals, each one with its characteristic thermal expansion coefficient, will results in a more complex behaviour and in an even more difficult interpretation of the spectra.

1.4 Aim of this work

Knowing the evolution and composition of the surface of Mercury enables us to discern several processes that operated during the formation of the inner Solar System (e.g. crustal accretion, impact gardening and global cooling of Terrestrial Planets). The elaboration and classification of remote sensing multi-band images allowed the interpretation of the stratigraphy, composition, age and structural evolution of Rembrandt basin and scarp system, i.e. the largest impact basin cross-cutting by contractional structure of the southern hemisphere of Mercury. The interaction of different scale processes has been demonstrated. Since the knowledge of the surface composition of Mercury is based on the interpretation of spectra, Thermal Infra-Red spectra of representative mineral phases have been measured in laboratory at the temperatures of the planetary surface. Significant changes in the high temperature spectra have been detected. Failure to allow for these effects leads to errors in the estimation of chemical compositions by Infra-Red spectra.

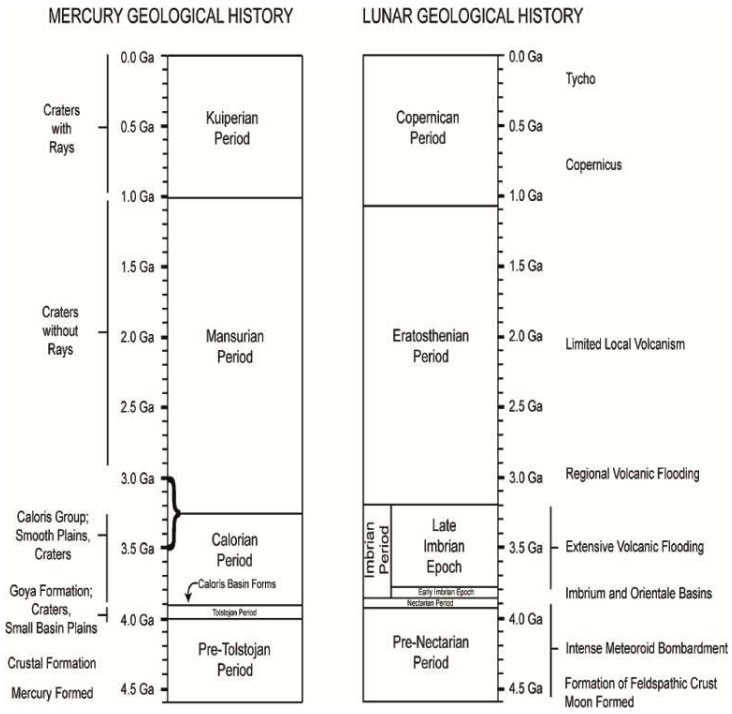

Figure 1.1: The geological time scale of Mercury compared with that of the Moon. The absolute ages for Mercury are assumed to be tied to the lunar time scale but are not independently known. Adapted from Head et al. (2007).

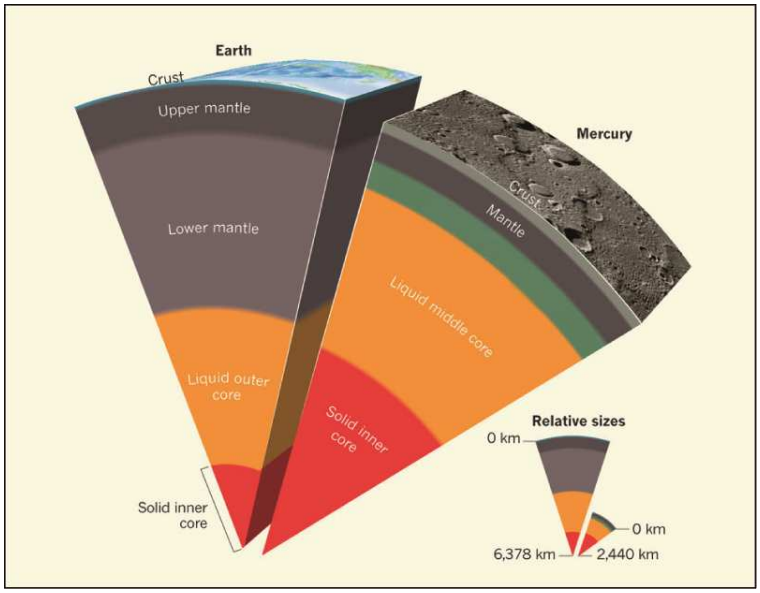

Fig. 1.2: Comparison between Earth and Mercury, adapted from a figure by NASA/Johns Hopkins Univ. Appl. Phys. Lab./Carnegie Inst. Washington.

2. The evolution of Rembrandt Basin and scarp system

2.1 Tectonism (and volcanism) on the Surface of Mercury

Mercury's tectonic activity was confined to its early history as a planet and several kinds of phenomena have been commonly invoked as global mechanisms of formation. The most ancient tectonic pattern consists of a fabric of fractures that have been attributed to the tidal despinning acting on the planet lithosphere (Fielder 1974; Dzurisin 1978). Wide arcuate scarps (i.e. *lobate scarps*) that randomly affect the surface of the planet have been interpreted as thrusts and reverse faults supposed to be the result of the shrinkage of the planet due to secular cooling (Murray et al. 1975; Strom et al. 1975; Dzurisin 1978, Watters et al. 2004). Sets of laterally contiguous lobate scarps and prominent ridges have been recently interpreted as systems analogous to terrestrial fold-and thrust belts (FTB, Byrne et al. 2012a) that might record an ancient pattern due to mantle convection in addition to global contraction (King 2008).

Furthermore, the formation of 1 500-km-diameter Caloris impact basin on the northern hemisphere of the planet strongly conditioned the pre-existent global stress fields, inducing basin-oriented tectonics within and surrounding the basin (Byrne et al. 2012b and reference therein, Fleitout and Thomas 1982) and hilly and lineated terrains near its antipode - by focusing the impact seismic waves (Strom et al. 1975).

In contrast to the widespread evidence of contractional deformation, normal faults that are so common elsewhere in the solar system are rare on Mercury, or rather concentrated within basin smooth plains of Caloris, Raditladi and Rembrandt (Strom et al., 1975; Dzurisin, 1978; Melosh and McKinnon, 1988) and expressed as a complex pattern of basin-radial and basin-concentric grabens. Strike-slip faults remain to be recognized on Mercury, except along the giant lobate scarp of Beagle Rupes (Rothery and Massironi 2010). A recent work of Massironi et al. (2012) investigates on this apparent lack, proposing several structures that display a strike-slip kinematics.

The volcanic history of Mercury was also confined to its early history, near the end of the Late Heavy Bombardment (Trask and Guest 1975; Spudis and Guest 1988). Its decline has been recently confirmed by MESSENGER Gamma-Ray Spectrometer (GRS) measurements (Peplowsky et al. 2011) as a marked decay in heat production. The volcanic style of Mercury implies widespread smooth deposits that cover heavily cratered terrains and basin floors (Head 1976, Head et al. 2009, Denevi et. al. 2009 in Fig. 2.4, Head et al. 2011). Younger volcanic deposits tend to fill the inner parts of the basins, embaying the older marginal deposits and suggesting earlier phases of basin-related volcanism. Indeed, smooth plains flooding giant impact basins as Caloris represent the last phases of volcanic activity. No major shield volcanoes such as on Mars have been detected yet. On the other hand, MESSENGER images displays candidates of vents and pyroclastic deposits, which are homogeneously distributed on the planet's surface and located principally on the floors of craters, along rims of craters, and along the edge of the Caloris basin (Kerber et al. 2011).

The resulting low degree of activities has been attributed to Mercury's small size. But, in spite of this apparent simplicity, many morphological features (i) cannot be explained by single previously mentioned geological processes and (ii) implies long-lasting activities of some of these processes. The southern hemisphere of Mercury hosts

the second largest well-preserved basin of the planet, which seems to comprehend most of the activities described above. Indeed, it is a giant impact feature filled by volcanic material and cross-cut by a prominent scarp. New observations on the development of the scarp with respect to the basin and very fresh dating of the involved geological units reveal a more complex scenario for origin, succession and duration of tectonic and volcanic activity on Mercury.

2.2 Experimental methods

2.2.1 MESSENGER images and data processing

Considering the extended mission approved in 2012, the MESSENGER spacecraft has just orbit Mercury for two Earth years after completing three flybys of that planet. Its payload comprehend the Mercury Dual Imaging System (MDIS), a narrow-angle and wide-angle multispectral imager that provide data for mapping landforms, surface spectral variations, and topographic relief (Gold et al. 2001). The wide-angle camera (WAC) has a 10.5° field-of- view (FOV) and consists of a refractive telescope having a collecting area of 48 mm. A 12-position multispectral filter wheel provides color imaging over the spectral response of the CCD detector. Ten spectral filters are defined to cover wavelengths diagnostic of different surface compositions and have bandwidths from 10-40 nm over a range of 415 nm to 1020 nm. A medium-band filter provides short integration for high-resolution imaging when the spacecraft is close to the surface (~300 km), and the last filter is panchromatic. The narrow angle camera (NAC) has a 1.5° FOV and uses a reflective design with a single medium-band filter with a passband identical to the one used in the WAC (650-850 nm). Each image will include four columns of dark reference pixels in order to correct for changes in background signal due to variations in operating temperature. Due to thermal constraints, only one camera will operate at a time.

MDIS instrument reached its first scientific goal producing a global monochrome map at 500 m/pixel resolution and a global color map at 2 km during the Mercury flybys. Each flyby viewed a different hemisphere of the planet, whereas both flybys passed the equator and enabled excellent mapping of the surface from ~50° S to 50° N latitude. During this phase, ~90% of the planet has been imaged, including the previously unseen hemisphere.

Then MESSENGER spacecraft has been placed in a highly elliptical orbit that resulted in a 10x difference in image resolution between the southern and northern hemispheres for a single camera. The NA camera has been used to image the southern hemisphere at a resolution comparable to imaging of the northern hemisphere acquired by the WA camera, thus resulting in a global basemap with nearly uniform resolution. In addition, MDIS imaged the planet two times as close as possible to nadir, allowing for analysis of the same areas with identical illumination to facilitate stereo matching. The NA camera has been also used in the northern hemisphere to obtain swaths at very high resolution down to scales of 20 m/pixel. During the primary orbital mission, the Polar Regions have been mapped.

Recent MESSENGER MDIS orbit coverage (Sept. 2012 release, average resolution of 250 m/pixel, Fig. 2.1) allowed us a detailed mapping of the geological units of the

Rembrandt area, providing a better resolution and covering the shadowed zones present in the flyby mosaics. The orbit images provided from the Narrow Angle Camera (NAC) for specific targets as the Rembrandt area - with a spatial resolution better than 200 m/pixel - have been particularly useful to highlight different textures of the geological domains and analyze the overlapping relationships between landforms.

Despite the worst average spatial resolution of ~500 m/pixel, single flyby images have been also used since they have been capture at high solar incidence angles and then stress the shallow reliefs. These sets of Experimental Data Records (EDS) returned by MESSENGER needed a preliminary processing to be usable by common cartography software. The EDS of the interested area have been converted and calibrated using the Integrated System for Imagers and Spectrometers (ISIS), which has been specifically developed by the United State Geological Survey for processing data originated by NASA spacecraft missions. The 28 obtained images are listed in Tab. 2.1.

We integrated the geological observation on NAC with the analysis of a red-green-blue (RGB) color composite product derived from 11-band WAC mosaics, combining 3 bands to enhance the reflectance of the planet surface (band 8 at 947.0 nm, band 5 at 628.8 nm, and band 3 at 479.9 nm for red, green, and blue, respectively).

For the structural analysis, the Digital Terrain Model (DTM) of Preusker et al. (2011) has been used. This DTM is derived from stereo pairs of flybys MESSENGER NAC images at spatial resolutions ranging from 450–550 m/pixel and covers more than half of the Rembrandt basin at a resolution better than 1 km/pixel.

Utilized products are listed in Tab. 2.2. Single images and mosaics have been analyzed in the ESRI ArcMap Geographic Information System (GIS) as equiangular projections, in order to provide a geological and structural map of the Rembrandt area.

2.2.2 Cross-cutting and overlapping relationships interpretation

With the inability to verify a unit's character in the field, the definition of *geologic units*, as well as the hypothetical nature of most unit contact relationships, assumes a slightly different meaning if applied on planetary geologic maps. *Geologic units* separated by various contacts are then characterized by what are interpreted to be primary morphologies, textures, or other attributes, distinguishing lithologies and/or formation ages. Ages can be attributed as 'relative' to adjacent units, and/or by cross-cutting or buried structures or landforms. In addition, the presence of secondary morphologic features yielding little or no information or similar "lithologies" without strong evidence for intervening hiatuses can generate the misrepresentation of planetary geologic units that complicates and biases the geologic story (Skinner and Tanaka, 2003).

Lithostratigraphic units, however, can be inferred through morphologies interpreted to have formed from emplacement processes. These types of materials form *rock-stratigraphic units*. Examples of rock-stratigraphic units of the surface of Mercury include lava flows, based on very smooth texture and possibly lobate flow margins, and impact breccias, based on variously degraded crater morphologies. Lithostratigraphic units are defined based on the lateral extent of characterizing primary surface features, the edge of which may be variably expressed by embayment, burial, and truncation relations (Wilhelms 1987; Tanaka, 1992). The second unit type useful for planetary

mapping is the *allostratigraphic unit*, which may be composed of multiple lithologies interpreted to have formed during a single continuous (or relatively continuous) event or episode, encouraging the recognition and correlation of genetic packages of materials rather than lithologically similar material units (Oviatt 1994). Discontinuities can be identified in remotely sensed datasets by cross-cutting relationships with bounding structures. Examples of potential allostratigraphic units of the surface of Mercury include mixtures of impact melt and breccias or volcanic overlays related to discrete eruptive episodes.

On the other hand, planetary structures provide the framework for determining the character and sequence of crustal deformation as well as geodynamic formational hypotheses. The geometry and kinematics of common planetary structures such as joints, deformation bands, faults, and folds can be determined from their distinctive morphologic and topographic signatures. In addition, the use of field-based Earth structures studies as analogs enables to infer their structural histories and deformation magnitudes. The surface of Mercury, for example, is mainly affected by systems of thrust faults having both blind and surface-breaking components. The nature and sequence development of these tectonic systems can thus be revealed interpreting their segmentation, displacement profiles, relay ramps and footwall anticlines (Schultz et al. 2010).

2.2.3 Crater counting

Statistical analysis of crater size-frequency distributions (SFDs) for the age determination of terrestrial planetary surfaces have been largely used during the last 50 years (e.g., Opik 1960; Shoemaker et al. 1962; Baldwin, 1964; Hartmann 1965). Based on the simple idea that older surfaces accumulate more craters, it was possible to infer relative ages of surface units by measuring the crater SFD on remote sensing images. The main stride for this technique was the radiometrically age determination of rock samples obtained by the Apollo and Luna missions, which allowed to develop a relative and absolute chronology for the Moon (e.g., Shoemaker et al. 1970a, 1970b; Baldwin 1971; Neukum, 1971; Hartmann 1972; Soderblometal 1974; Neukum 1977; Neukum and Wise 1976). The fluxes of crater-forming impactors observed for different parts of our solar system made it possible to calibrate this lunar chronology function for different terrestrial planets and satellites (e.g., Neukum et al. 2001a; Ivanov 2001; Hartmann and Neukum 2001). Hence the determination of ages of different planetary surfaces is currently possible without obtaining samples, by using image data of remote sensing missions. This methodology, hereafter referred as the Neukum Production Function model, permits the transfer of the Lunar chronology to Mercury (Neukum et al. 2001b). The Model Production Function (MPF) method proposed later by Marchi et al. (2009) applies the same cross-calibration with the Lunar chronology, but estimates the impactor flux to Mercury *a priori*, using dynamical models that describe the formation and evolution of the asteroids in the inner Solar System. The main advantages of this method are (i) avoiding a multiple use of scaling laws, (ii) simulating a non-constant impactors flux through time, and (iii) using a variable crustal layering of the target body (see *P.2.5* for details).

The determination of crater SFDs of surface units requires the accurate measure of the area selected for the count, which should belong to an homogeneous geological unit, and of the crater diameters included in that area (e.g., Wilhelms et al. 1987 and *P.2.2.2* above). To this end, the right choice of map projection becomes paramount. To resolve distortion problems introduced by different map projections, we used an extension for ESRI's ArcGIS suite developed by Kneiss et al. (2011) that measures the diameters of impact craters independently of the particular map projection of the image basis.

EN0108828250M	EN0108830673M	EN0108830197M	EN0162744436M
EN0108828255M	EN0131766385M	EN0108830635M	EN0131766417M
EN0108828302M	EN0162744327M	EN0131766422M	EN0131766438M
EN0108828307M	EN0131766380M	EN0162744300M	EN0162744290M
EN0108829060M	EN0131766401M	EN0108828156M	EN0162744295M
EN0108828307M	EN0162744354M	EN0108828198M	EN0162744317M
EN0108829111M	EN0162744431M	EN0108828203M	EN0162744322M

Table 2.1. Experimental Data Records (EDS) returned by MESSENGER NAC used in this work (centered on Rembrandt basin at 88°E, 33°S).

Products	**Instrument**	**Mission stage**	**av. spatial res.**
PAN images	MDIS NAC	2^{nd}, 3^{rd} Fybys	450-600 m/px
PAN images	MDIS-NAC	orbit	150-250 m/px
PAN mosaic	MDIS NAC, WAC	orbit	250 m/px
Multispectral mos.	MDIS WAC	orbit	500 m/px
DTM - Stereo images	MDIS NAC	2^{nd}, 3^{rd} Fybys	450-650 m/px

Table 2.2. MESSENGER MDIS products and derived products used in this work.

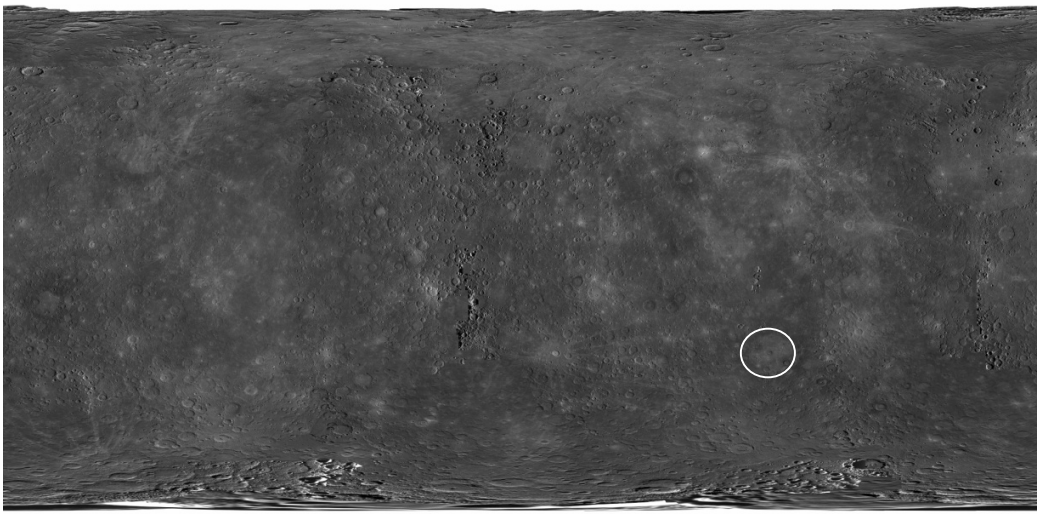

Figure 2.1. MDIS 750 nm mosaic – including Mono (NAC and WAC) and Color (750nm filter) images collected after orbit insertion and included in PDS delivery 8 (September 2012), NASA/Johns Hopkins Univ. Appl. Phys. Lab./Carnegie Inst. Washington. Rembrandt basin (white line) showed in Fig. 2.2.

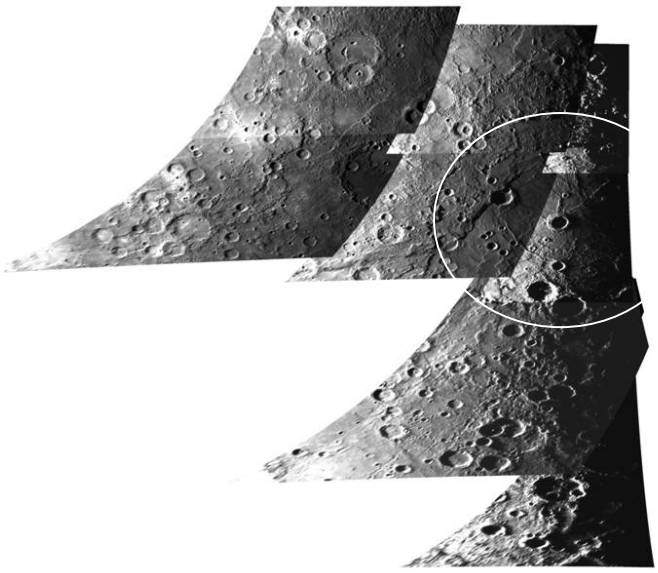

Fig. 2.2. Overlapped single sinusoidal NAC flyby images (average spatial resolution of~500 m/pixel) centered on Rembrandt basin (white line, 88°E, 33°S) and captured at high solar incidence angles.

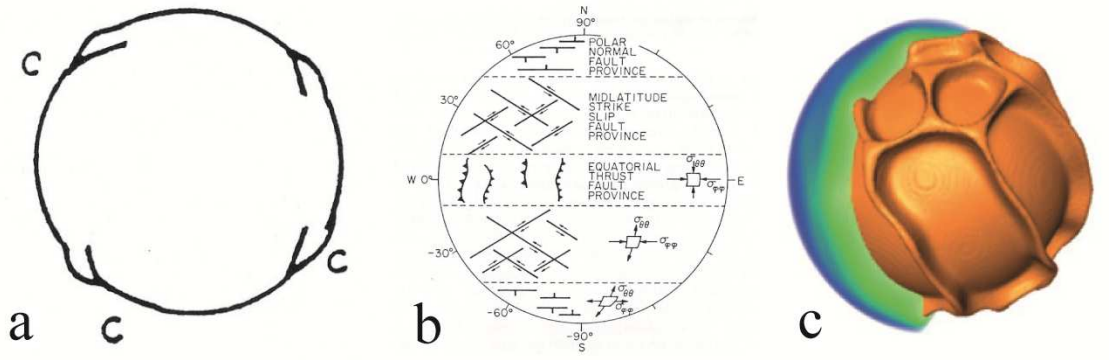

Figure 2.3. Global tectonic mechanism and relative features hypnotized for Mercury. a) Contraction due to the global cooling of the planet with randomly distributed lobate scarps (Strom et al. 1975). b) Despinning of the planet with oriented contractional features at the equator and oriented extensional features at the poles (Melosh 1977). c) Mantle convection with heterogeneous distribution of contraction (King 2008).

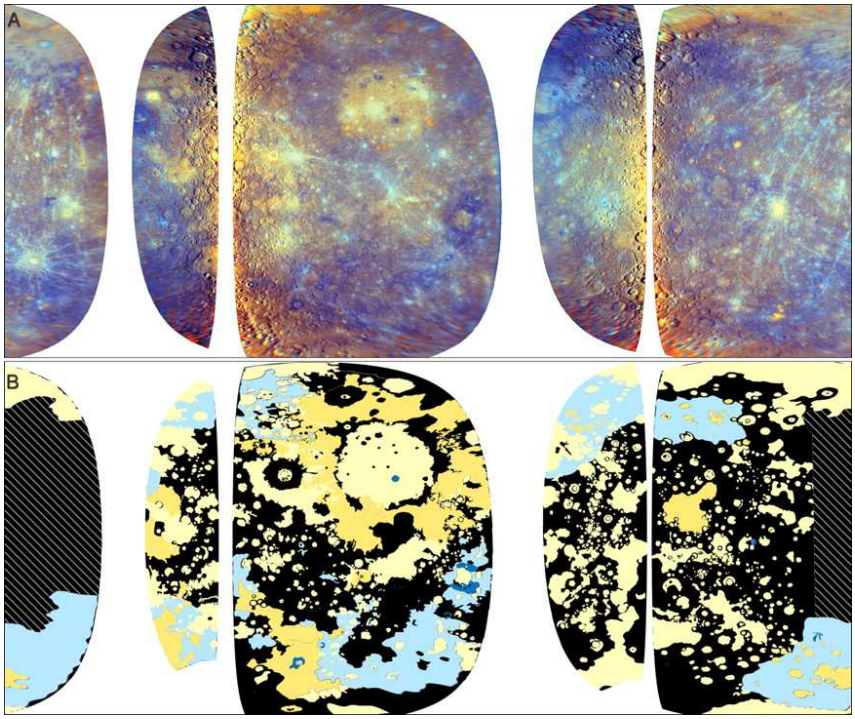

Figure 2.4. Simple cylindrical views of Mercury over ±75° latitude, 0° to 360°E longitude. (A) Enhanced color MDIS WAC mosaics. Areas in white are regions not yet imaged by MESSENGER. (B) Geologic map of Mercury from MESSENGER WAC and NAC mosaics and Mariner 10 clear-filter mosaics. Light yellow, HRP and IP; dark yellow, LBP; light blue, regional LRM; dark blue, LRM center; black, other (fresh crater ejecta or IT); and white, no data. Adapted form Denevi et al. 2009.

2.3 Results and conclusions

Results and conclusions of chapter 2 are presented in two manuscripts in submission. The first manuscript - entitle "*The Structural Evolution of Rembrandt Basin and Scarp System, Mercury"* (par. 2.3.1) - presents a detailed geological and structural appraisal of a specific area of the surface of Mercury, the Rembrandt basin area. The occurred interpretation suggests that the action of global contractional tectonism on Mercury might be strongly influenced on local scales by the stress fields induced by impact craters and basins. This study has been conducted with the essential collaboration of Matteo Massironi[1,2], Christian Klimczak[3], Paul K. Byrne[3], Gabriele Cremonese[2] and Sean C. Solomon[3,4].

The second manuscript - entitle "*The long-lasting activity of Rembrandt Basin and scarp system, Mercury*" (par. 2.3.2) - report the age determination of the geological units determined for Rembrandt basin area by applying the Model Production Function of Marchi et al. (2009). This study has been conducted with the essential collaboration of Matteo Massironi[1,2], Simone Marchi[5], Paul K. Byrne[3], Christian Klimczak[3] and Gabriele Cremonese[2].

Concerning both manuscripts, we thank Elena Martellato for her advice on crater counting methods and data plots. This research was supported by the Italian Space Agency (ASI) within the SIMBIOSYS Project (ASI-INAF agreement no. I/022/10/0).

[1]Department of Geosciences, University of Padua, Padova, Italy
[2]Astronomical Observatory of Padua, INAF, Padova, Italy
[3]Department of Terrestrial Magnetism, Carnegie Institution of Washington, Washington DC, USA
[4]Lamont-Doherty Earth Observatory, Columbia University, Palisades, NY USA
[5]NASA Lunar Science Institute Center for Lunar Origin and Evolution, Southwest Research Institute, Boulder, CO, USA

2.3.1 The Structural Evolution of Rembrandt Basin and Scarp System, Mercury

Abstract

Detailed structural mapping of the Rembrandt basin and scarp system, based on MErcury Surface, Space ENvironment, GEochemistry, and Ranging (MESSENGER) spacecraft flyby and orbital images, reveals new insights into the geological evolution of the region. Cross-cutting relationships show that the development of the Rembrandt scarp was affected by tectonics related to the basin's evolution. Evidence suggests that the impact event caused a dramatic change to the regional stress field, influencing the propagation direction of the pre-existing Rembrandt thrust. Subsequent tectonism and volcanism formed the complex array of structures within the basin and a late-stage lava flow proximal to the northern rim. Our study shows that the tectonic development of the basin occurred in parallel to that of the through-going scarp.

Introduction

During its second and third flybys, the MESSENGER Mercury Dual Imaging System (MDIS) (Hawkins et al. 2007) imaged a previously unseen, well-preserved basin named Rembrandt in Mercury's southern hemisphere (Fig. 2.5a). With a diameter of 715 km, Rembrandt is among the largest impact basins recognized on Mercury (Watters et al. 2009b; Fassett et al. 2012). It is also one of the youngest major basins of Mercury having formed near the end of the Late Heavy Bombardment (LHB) approximately 3.8 Gyr ago (Watters et al. 2009b). Much of the basin interior has been resurfaced by smooth, high-reflectance plains interpreted to be of volcanic origin (Denevi et al. 2009). This unit hosts sets of landforms interpreted to be contractional and extensional tectonic structures, which generally have radial and concentric orientations with respect to the basin centre. This pattern resembles the arrangement of structures observed within the Caloris basin (Murchie et al., 2008; Watters et al. 2009c; Byrne et al. 2012b), with individual sets of landforms most likely due to multiple episodes of deformation (Strom et al. 1975; Melosh and McKinnon 1988; Watters et al. 2005; Watters et al. 2009b). The contractional features are primarily comprised of wrinkle ridges, which are believed to have formed from flexural slip folding of the surface units as a response to reverse faulting at depth (Watters 1988; Golombek et al. 1991; Schultz 2000). The extensional structures are troughs interpreted to be graben (Watters et al. 2009b; Watters et al. 2009c), which are characterized by two antithetic, inward-dipping normal faults.

Of particular note in the area within and surrounding Rembrandt basin is a 1000-km-long reverse fault system (Watters et al. 2009b; Byrne et al., 2012a) that trends ~E–W as it cross-cuts the basin's western rim, and bends toward the North within the basin before tapering into the impact material (Fig. 2.5a). Based on this morphology, Watters et al. (2009b) characterized the fault system as a lobate scarp (Watters et al. 2001; Watters and Nimmo 2010) and attributed its formation, localization, and orientation to crustal shortening resulting from global contraction as Mercury's interior cooled. More generally, this process has been regarded as responsible for lobate scarps, wrinkle ridges, and high-relief ridges that were observed on Mariner 10 images (e.g. Strom et al. 1975)

and have been shown to occur planet-wide by MESSENGER data (Watters et al. 2001 and 2004). In addition to the many thrust fault related landforms, topographic data from the Mercury Laser Altimeter instrument (MLA) (Cavanaugh et al. 2007) aboard the MESSENGER spacecraft and from stereo imaging (Preusker et al. 2011 and 2012) have revealed long-wavelength topographic undulations (Zuber et al. 2012) that also occur in association with some of the larger tectonic structures and may be evidence of large-scale contraction of Mercury's lithosphere (Byrne et al. 2012a; Watters et al. 2012a).

Recent recognition of several kinematic indicators of strike-slip motion along the Rembrandt scarp (Massironi et al. 2012) and the location of the large scarp system cutting inside and outside the Rembrandt basin motivates a study to investigate the complex relationships between the Rembrandt basin and the scarp. In this paper, we mapped the structures in the Rembrandt basin area in fine detail using MESSENGER images from fly-by and orbital campaigns in order to obtain better insights in the kinematic development of the Rembrandt scarp system and whether its development was influenced by the interaction between global- and basin-scale processes.

Material/Data

MESSENGER MDIS orbital coverage (Fig. 2.5a) allowed us a detailed mapping of the geological units of the Rembrandt area at resolutions better than 200 m/pixel. Mainly collected at low solar incidence angles, it allowed us to interpret also previously shadowed areas. Orbital MDIS wide-angle camera (WAC) images were supplemented by targeted narrow-angle camera (NAC) images, which are particularly useful for highlighting different textures of geological units and for morphological analyses. We integrated this MDIS orbital dataset with flyby NAC images, which have been collected at high solar incidence angles and then can stress the shallow reliefs. We also used a red-green-blue color composite product derived from 11-band WAC mosaics (ref?), combining 3 bands to enhance the reflectance of the planet surface (band 8 at 947.0 nm, band 5 at 628.8 nm, and band 3 at 479.9 nm for red, green, and blue, respectively). For our structural analysis, we also used the Digital Terrain Model (DTM) of Preusker et al. (2011), which is derived from stereo pairs of flyby MESSENGER NAC images at spatial resolutions ranging from 450–550 m/pixel. The DTM covers more than half of the Rembrandt basin at a resolution better than 1 km/pixel. The whole dataset has been processed with the Integrated Software for Imagers and Spectrometers (ISIS) developed by the United States Geological Survey, and analyzed in the ESRI ArcMap geographic information system (GIS) environment. The morphological, textural, and kinematic analysis is shown in the map of the Rembrandt area (Fig. 2.5b), which includes basin-related geological units as well as the basin and scarp tectonic structures.

Geology and structure in and around Rembrandt basin

In order to characterize the sequential development of the basin and scarp, we identified the primary geological units, mapped the tectonic patterns within the basin, and subdivided the Rembrandt scarp according to the kinematic expression of each segment.

Main geological units of Rembrandt basin

We subdivided Rembrandt basin into three main units, based on different primary morphological characteristics: the *Hummocky Material* (HM) and the *Interior Plains* (IP) fill the basin, and the *Proximal Ejecta* (PE) lies just outside the basin rim (Fig. 2.5b). The HM consists of a mixture of impact melt and ejecta deposits (breccias) that formed during the impact event and stand out for the thick alternation of hills, depressions and higher knobs, which are characteristic features for such large basins (e.g., Cintala and Grieve, 1998; Watters et al., 2009a). In the case of Rembrandt, HM is mostly buried by widespread smooth IP but is still visible along the northern margin of the basin (Fig. 2.5b), where the knobs are massive and rise above the surrounding terrain (white arrows, Fig. 2.6a). Because of this difference in elevation, the exposed HM appears as an inner ring partially reworked by subsequent impact events (white arrows, Fig. 2.6b). The smooth IP are brighter than the ring of impact HM, and Denevi et al. (2009) associated the high reflectance they show to a volcanic origin. IP unit covers most of the basin floor with two distinct exposures, whose the most extensive IPa blankets the central portion of the basin, extending to both the western and the eastern rims (Fig. 2.5b). IPa fills also the eastern sector of the basin floor, unseen in flyby data, and superposed the hummocky annulus as it reaches the rim (Fig. 2.6c). In the same spot, a pit-floor crater (cf. Gillis-Davis et al., 2009) aligned sub-parallel to the basin rim may represent a possible source of volcanic material (crater C8, Fig. 2.6c). In the southwest sector of the basin, the MDIS WAC multispectral mosaic shows color variegation within the smooth plains: IPa maintains the same smooth texture but becomes darker in spectral reflectance, coming to resemble the adjoining outer-basin material (black arrow, Fig. 2.6d). The color variation of the smooth plains units on Mercury has been alternatively attributed to a different stage of surface maturity or a different composition (Robinson and Lucey, 1997; Blewett et al., 2007; Robinson et al., 2008; Murchie et al., 2008). Notably, beyond the southwestern rim the now darker inner smooth plains (IPa) become texturally indistinguishable from the surface exterior to the basin.

The second, less extensive smooth layer IPb fills the northern margin of the basin floor (Fig. 2.5b), embaying the basin rim wall (white arrows, Fig. 2.6e). Despite the similarity in texture and reflectance, there is no evidence of a spatial connection between IPb and IPa, which may imply two discrete emplacement events. In addition, IPb is present at a higher average elevation than IPa (-440 m vs. -1 290 m; see Fig. 2.8c). It is therefore unlikely that a single volcanic event at the basin centre is responsible for both IPa and IPb units.

Beyond the basin rim, the ejecta deposit extends for hundreds of kilometers, and includes several troughs radial to Rembrandt, which are the result of impact sculpting. The *Proximal Ejecta* (PE) unit is composed of thick, coherent ejecta following the rim crest, and is likely coeval with the HM unit. These deposits are comparable to the outcrops of the Caloris Montes (Fassett et al., 2009), and assume different morphologies locally, with a blocky texture on the basin rim and single domes collapsed toward the basin interior, and a radially lineated or smoothed appearance outside the basin (white arrows, Fig. 2.6c).

Primary geological structures of the Rembrandt area

The Rembrandt basin displays a large variety of tectonic patterns (Watters et al. 2009b). The interior of the basin is characterized by both extensional and contractional tectonic landforms. Entirely confined within the central IPa, extensional features are as primarily basin-related graben, whereas contractional landforms are either basin-localized structures, predominantly in the form of wrinkle ridges, or form part of the wide Rembrandt thrust and back-thrust system.

Basin-interior landforms

Families of radial and circumferential features, both extensional and contractional, have been identified on the smooth plains of Rembrandt basin (Fig. 2.5b). We mapped over 250 radial wrinkle ridges and graben of variable lengths (5 to 60 km), which describe a partial fan-like pattern within the IPa unit; these structures extend outward ~100–200 km from the basin center and are mainly bounded by a prominent ring of concentric wrinkle ridges approximately half a basin radius from the center (Fig. 2.5b). A set of circumferential graben appears parallel to the concentric ridges along the northern part of the fan-like pattern (Fig. 2.5b). Structural mapping reveals a major difference in structure within the Interior Plains of the Rembrandt basin, with far more structures in the northern portion of the basin than in the south one. This uneven distribution of wrinkle ridges and graben is not an artifact of poor lighting geometry, since all the studied images have been acquired at different illumination conditions and show the same paucity of basin-related structures in the southern part of the basin. In the southern interior, the lack of basin-oriented structures could be due to a possible thickening of IPa together with the masking effect of superposed craters ejecta.

The Rembrandt basin area also displays local clusters of contractional features, including a complex set of wrinkle ridges and scarps between the wrinkle ridge ring and the pit-floor crater at the eastern rim (red arrows, Fig. 2.6c), a group of lobate scarps between the Rembrandt scarp and the basin-related features (red arrows, Fig. 2.6d), and wrinkle ridges radial to the superposed craters C9 in Fig. 2b and C13 in Fig. 2.6f (45 km and 70 km in diameter, respectively; red arrows point to the radial wrinkle ridges).

Most of the morphologies of the basin-related structures of Rembrandt Basin are similar to those of the Caloris basin (Watters et al. 2009c; Byrne et al., 2012b) and the lunar maria (Strom, 1972; Bryan, 1973; Maxwell et al., 1975). Whereas the overall structural map-pattern differs from that of Caloris basin, where graben start almost immediately from the basin center (Murchie et al. 2008; Watters et al. 2009c), as well as from that commonly observed within lunar maria, where extensional structures developed outside concentric wrinkle ridge rings (Solomon and Head 1980; Watters et al. 2005).

The Rembrandt scarp and global-scale landforms

Although formed originally as a coherent, single scarp system, also described as fold-and-thrust belt (FTB) by Byrne et al. (2012a), the Rembrandt scarp appears to have

undergone a complex deformational history that was profoundly influenced by the Rembrandt basin in terms of surface heterogeneity and crustal layering. We regard the eponymous scarp as the surface expression of a large-scale thrust fault system, which features a back-thrust and displays several kinematic indicators of lateral movements along its length. We divided the structure into two main branches on the basis of the lateral shear indicators. Outside the basin, the ENE-trending western portion of the scarp (S1, Fig. 2.7a) shows a set of sharp "S-shaped" restraining bends (white arrows, Fig. 2.7a) (Mann, 2007 and reference therein) that suggests a right-lateral strike slip movement. This kinematics is consistent with the eastward deformation of the ejecta of the 70-km-diameter nearby crater C2 (dashed arrow, Fig. 2.7a). Within the basin, the SW-NE trending segment (S2, Fig. 2.7b) comprehend a sigmoidal positive-relief resembling a positive flower structure product by a left-lateral strike-slip component (red arrows, Fig. 2.7b). The overall kinematics is inferred from the convergence of the opposite strike-slip senses of movement of these two branches, and suggests a SE-vergent thrust acting in response to NW–SE oriented compressional forces.

The S1 and S2 branches of the scarp system have morphological characteristics that possibly reflect independent evolutions. S1 consists of a homogeneous thrust and back-thrust system similar to high-relief ridges (Ruiz et al. 2012), with a prominent leading edge across which there is more than 2 500 meters of relief (Fig. 2.8b). This scarp faces a parallel structure, termed RS2 by Ruiz et al. (2012), which is located to the southwest of the Rembrandt basin (Fig. 2.8a). The Rembrandt scarp system is well-developed inside the basin, whereas the RS2 scarp described in Ruiz et al. (2012) appears to end outside the basin. The two scarps bound a topographically low-lying area similar to a foreland basin between two converging thrust systems, such as the Kura basin between the Greater and the Lesser Caucasian belts (Philip et al. 1989).

The S-shaped restraining bends due to dextral lateral shear (white arrows, Fig. 2.7a) locally enhance the elevation of the S1 scarp by several hundred meters. The ESE strike of S1 ends exactly at the Rembrandt basin rim, where the structure bends toward north and forms the SSW–NNE S2 scarp and the shallow back-scarp. Further along strike, both scarps form a sigmoidal positive-relief flower structure (red arrows, Fig. 2.7b). Beyond that, S2 strikes N–S and cuts the HM unit with a basin-radial orientation; nearby, a similarly orientated scarp developed parallel to S2 (white arrow, Figure 2.7b).

Using the DTM of Preusker et al. (2011), we obtained a set of topographic profiles crossing the Rembrandt scarp (Fig. 2.8a). We took profiles across the scarp leading edges of both S1 and S2 at sites free of superposed craters and their ejecta deposits. The elevation of each profile, along with the extrapolated vertical displacement (throw), has been plotted along the length of the scarp (Fig. 2.8b) displaying the change in elevation along both branches. The vertical relief of 3 100 m across S1 is stressed by the deep depression at the scarp bottom and the sharp restraining bends on its top, whereas S1 rises in elevation close to the basin perimeter, but decreases in relief to 2 300 m; from immediately inside the basin to the flower structure, the S2 scarp maintains similar throws, before reducing dramatically as it encounters the structural pop-up and then the HM unit. A 55-km-diameter crater is superposed on the kink between S1 and S2 (C3 in Fig. 3b, corresponding with the basin rim), obscuring any information on the nature of the connection between the two branches.

Cross-cutting relationships

By determining the size-frequency distribution (SFD) of superposed impact craters on the Rembrandt basin rim using MESSENGER fly-by data, Watters et al. (2009b) estimated that Rembrandt and Caloris basins have a similar relative age. We applied the same method using MESSENGER orbit data in order to compare the relative ages of the two major domains of Rembrandt basin, the impact-forming material (HM and PE) and the central smooth plains (IPa). We collected and elaborated crater counting using the ESRI ArcMap CraterTools extension developed by Kneissl et al. (2011). The differences between the crater densities displayed in the R-plot of Fig. 2.10 are almost negligible, and so the two domains cannot be definitively said to be different in age. Therefore, crater statistics cannot discriminate whether the IPa unit is impact melt formed during basin formation, or volcanic material emplaced soon after the basin formation. However, we note that both IPa and IPb appear to have resurfaced several craters that postdate the Rembrandt basin (e.g., craters marked with yellow arrows in Figs. 2.6a and 2.6c), and IPb clearly embays the basin rim wall (Fig. 2.6e) postdating the basin floor formation. These observations support a volcanic origin for the IPa and IPb units. Moreover, the color variegation of IPa (Fig. 2.6d) may also reflect resurfacing by, or at least a change in composition of, volcanic material. Since IPa and IPb seem not to be spatially connected, we cannot definitively assume a common source; this may imply the existence of several volcanic sites within the Rembrandt basin (though such sites may have been buried during subsequent volcanism). Both units have been clearly cross-cut by parts of the Rembrandt scarp (S2) however, and thus their emplacements predate the formation of the scarp. Similarly, the wrinkle ridges and graben, which exclusively developed within the IPa unit, postdate the smooth planes emplacement. In addition, radial graben appear to cross-cut the ring of wrinkle ridges in the southwest sector of the basin (e.g. white arrow in Fig. 2.7b); without clear offsets of marker units or structures the age relationship here is uncertain, but if the graben postdate the ridges then at least local extension occurred subsequent to a phase of contraction within the basin as also noted by Watters et al. (2009a).

Of particular note is the parallel alignment of the S2 scarp to the concentric wrinkle ridges on the basin floor in the northwestern sector (Fig. 2.7b), indicative of a direct influence by structures related to basin tectonism upon the development of the scarp. However, a 9-km-diameter crater (Cm in Fig. 2.7b) obscures any potential evidence of relative timing between these features. Even so, the positive flower structure along S2 (red arrows, Fig. 2.7b) is accompanied by narrow wrinkle ridges (red dashed arrows, Fig. 2.7b) that appear related to basin tectonism, suggesting again that the Rembrandt scarp was influenced by followed and uplifted pre-existing basin-related structures. In addition, topographic profiles across S2 show lower cumulative throws than those of S1 (Fig. 2.8b), indicating that the basin-interior branch accumulated lower strain, and/or was active for a shorter period of time, than that portion outside Rembrandt.

In the southwestern sector of the basin, between the Rembrandt scarp and the basin-related structures, lies a set of minor lobate scarps with orientations ranging from orthogonal to the scarp to basin-radial and parallel to the S2 branch (i.e., mainly NE-SW striking) (white dashed arrows, Fig. 2.7b). These scarps cannot be considered entirely basin-related structures, for there is at least a radial component to their orientation, such

as those that cross-cut the basin rim and extend to the outer units beyond (Fig. 2.6d). These structures have previously been suggested to be a continuation of the southern giant scarp RS2 (Ruiz et al. 2012) within the basin, such that their formation has been attributed to global contraction. However, this inference appears uncertain, because the similar strikes of the S1 and RS2 scarps suggest a common NNW–SSE-orientated regional stress field that does not support the development of RS2 branches with strikes toward North. Instead, these minor scarps could have been induced by a perturbed regional stress field and nucleated along orientations similar to those of basin-related structures.

Finally, we noted that every superposed crater along the entire Rembrandt scarp hosts minor contractional structures (e.g. crater C3, 60-km-diameter crater C4a and subsequent smaller 25-km-diameter C4b in Fig. 2.7b) that parallel the main strike of the S1 and S2 branches. We regard these observations as evidence for the sustained accumulation of strain by the main Rembrandt FTB over an extended period of time, unaffected by subsequent impact events. In particular, craters C4a and C4b along the S2 branch have been substantially modified by the thrust, displaying a 1 800-m-high scarp within the older C4a crater, whereas crater C3 displays a shallow structure thrust-aligned but with opposite vergence; both these craters seem to be not affected by the basin-related structures, neither their ejecta, postdating the basin-related stress field activities.

Timing of the Rembrandt basin and scarp

Unlike smaller lobate scarps elsewhere on the planet, the Rembrandt fold-and-thrust belt shows unusual structural and morphological characteristics, particularly in terms of its two branches, S1 and S2, which are characterized by different strikes and vertical displacements, and by indicators for lateral movement of opposite sense. We regard these differences as evidence that the basin affected the growth of the scarp. This influence could have been active or passive, depending on the relative timing of the basin-forming impact event with respect to the scarp development.

If the impact preceded the initiation of thrust faulting, it would have passively influenced the development and final geometry of the scarp through the generation of basin-related structures due to basin-scale stresses, and via inhomogeneous crustal layering within the basin itself. Spudis and Guest (1988) suggested that several ancient buried basins in Mercury’s crust form structural weaknesses that can control the subsequent geologic evolution of the surface. Moreover, Watters et al. (2001, 2004, 2012) and Fassett et al. (2012) directly observed that pre-existing mechanical discontinuities such as basin slopes and rims may have constrained the shape of several lobate scarps.

Under such a scenario, we could suppose that the (well-preserved) large Rembrandt basin affected the later development of a contractional ridge system. The excavation of a giant impact could induce lateral lower-crustal flow toward the basin, resulting in uplift of the basin centre and promoting the development of basin-related structures within the crater (Fleitout and Thomas 1982; Watters et al. 2005). Sustained global contraction of a cooling planet would result in the formation of contractional landforms, with basin-localized stresses producing radial contractional features around it (Fleitout and Thomas 1982). The subsequent development of the Rembrandt scarp could have been controlled

by these pre-existing features, which acted as horizons of weakness. In fact, the S1 Rembrandt branch is radially oriented with respect to the center of the basin, whereas the S2 branch is tangential to basin-related concentric wrinkle ridges. This scenario accounts for the change of orientation from S1 to S2, though does not predict differences in vertical displacements between each segment.

An alternative interpretation involves the Rembrandt-forming impact event occurring during the thrust activity responsible for the scarp system. The impact could have led to a local reworking of the structure and a substantial change in the regional stress field. This scenario requires a pre-existing ridge (essentially a primitive S1, Fig. 2.10a) with an overall WSW–ENE strike facing a wide foreland basin, together with a parallel belt (RS2, Ruiz et al. 2012), both developed in response to a NNW–SSE-orientated maximum horizontal stress. The subsequent formation of the Rembrandt basin (Fig. 2.10b) partially erased S1 and most likely supported a multiple but short stage of volcanism that recorded the basin-related tectonism. The giant impact may have also promoted lower crustal flow toward the basin centre, causing a perturbation of the regional stress field with a consequent change in the S1 vergence from NNW–SSE to NW–SE and the development of later strike-slip structures (Fig. 2.10c). Sustained development of the Rembrandt scarp (i) led to the formation of the transpressive S2 branch, whose growth was passively controlled by the basin structure (Fig. 2.10c) and accumulated less strain than the older S1 branch, and (ii) lasted enough to form secondary structures within the basin and the superposed craters. Proximal basin ejecta would have contributed to the sharp elevation contrast between the branch outside the Rembrandt basin and that within the basin (Fig. 2.8b). This scenario satisfies each of the observations we described in this study, and may be the most likely process through which the complex Rembrandt basin-and-scarp system formed.

Conclusions

Using different MESSENGER MDIS data, we performed a detailed geological and structural appraisal of the Rembrandt area, characterizing the relationship between the basin and the scarp and investigating the evolution of the overall basin and scarp system. Our proposed sequence of events places the Rembrandt basin-forming impact event during the thrust activity. The formation of the basin thus influenced and complicated the growth of a pre-existent transpressive structure, which developed as a result of global contraction of Mercury as its interior cooled. In a broader sense, this sequence suggests that the action of global contractional tectonism might be strongly influenced on local scales by the stress fields induced by impact craters and basins.

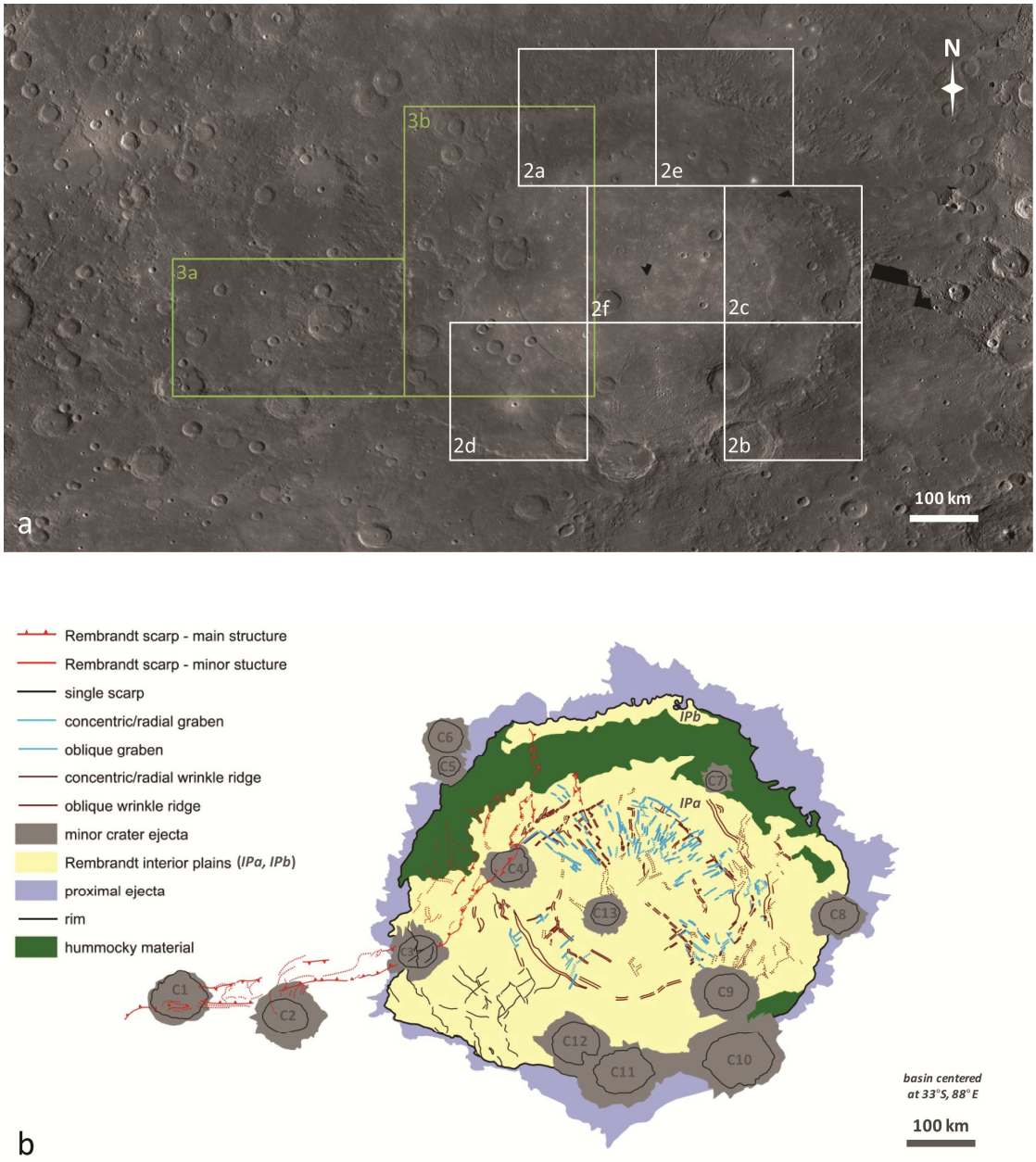

Figure 2.5. (a) MESSENGER MDIS monochrome base map centered on the Rembrandt basin (33°S, 88°E). White boxes outline areas shown in Fig. 2.2, whereas green boxes outline areas shown in Fig. 3. (b) Geological and structural map of the Rembrandt basin and scarp system.

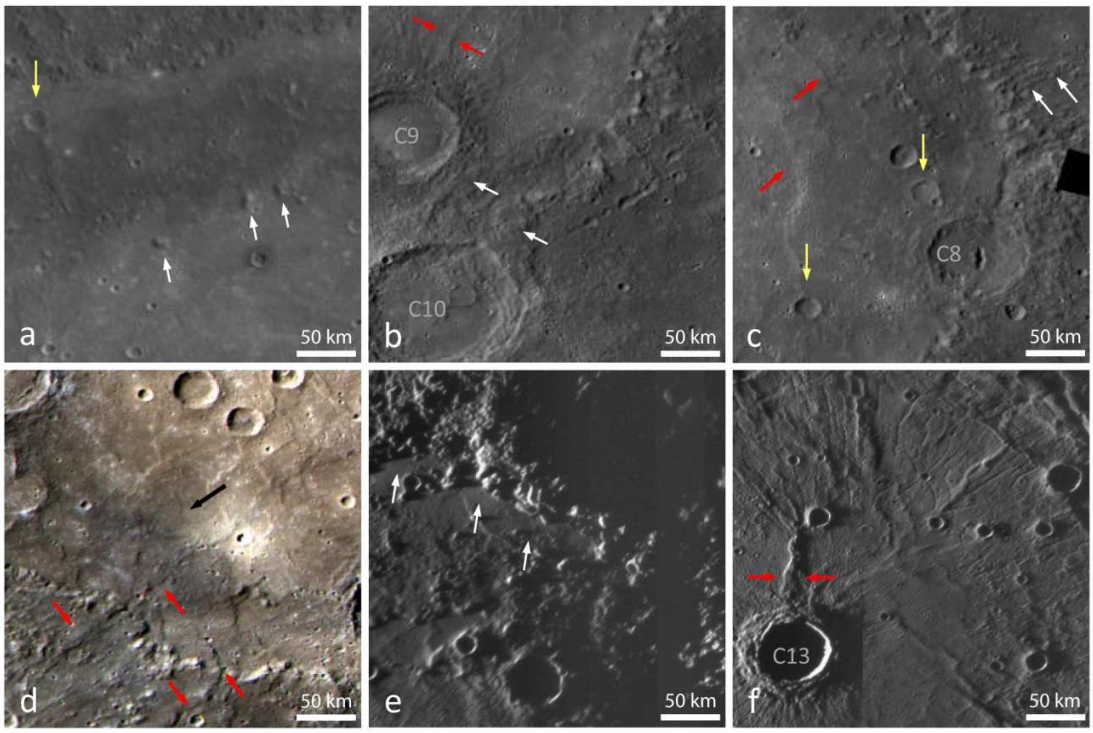

Figure 2.6. Close-up view of areas of interest within Rembrandt basin, extracted by flyby and orbital MESSENGER MDIS mosaics. (a) Hummocky Material (HM) displays large blocks (white arrows) that stand higher than the surrounding lighter, smooth Interior Plains (IPa). A partially filled crater (yellow arrow) suggests resurfacing and a volcanic origin for the IPa unit. (b) HM of the southern Rembrandt basin is partially reworked (white arrows) by subsequent impact events C9 and C10; a secondary set of wrinkle ridges have formed (red arrows) radial to crater C9. (c) Along the eastern Rembrandt basin rim, a pit-floor crater (C8) represents a possible eruptive site; IPa reaches the basin rim, covering the basin floor and pre-existing craters (yellow arrows), but subsequently contraction has formed a set of scarps (red arrows). Beyond the rim, proximal basin ejecta and impact-sculpted terrain extend radially from the basin (white arrows). (d) MDIS WAC multispectral mosaic showing color variegation within IPa: while retaining the same texture, the unit becomes darker toward the basin rim (black arrow). A set of scarps cuts through this unit and extends beyond the basin rim and into the proximal ejecta (red arrows). (e) The smaller IPb unit within the northern margin of Rembrandt basin embays the basin rim wall and ejecta of a 200-km-diameter superposed basin (white arrows). (f) A prominent wrinkle ridge developed radial to the superposed crater C13 (red arrows).

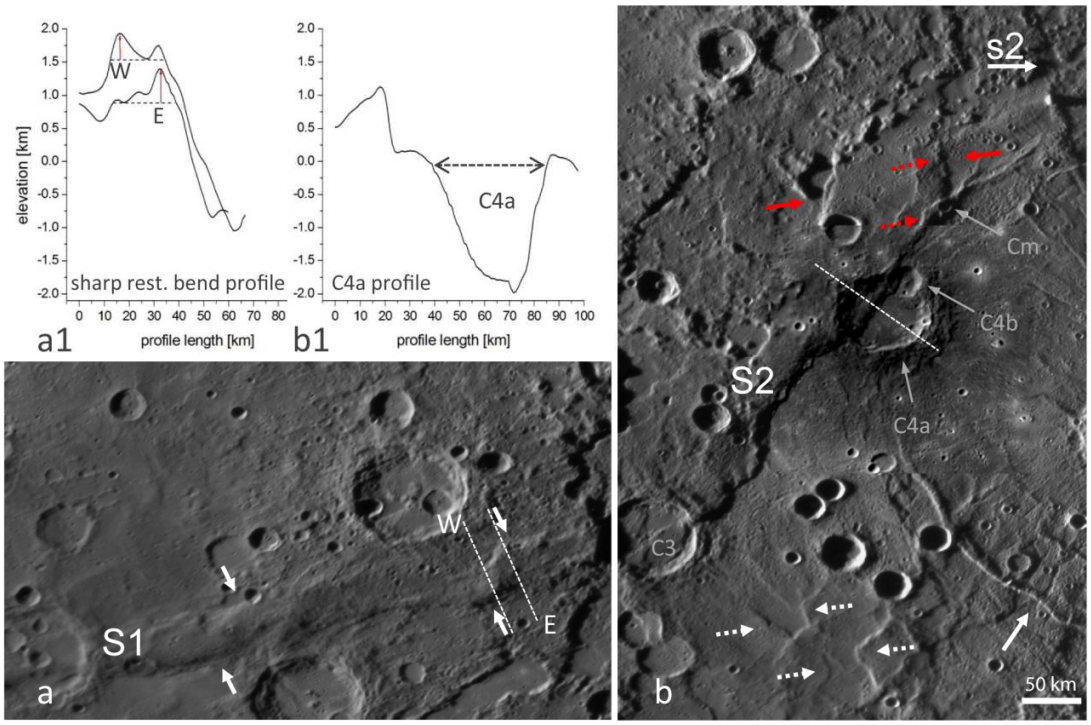

Figure 2.7. Detailed views of the S1 and S2 branches of the Rembrandt scarp. (a) Outside Rembrandt basin, the S1 branch strikes WSW–ENE and verges SSE; its elevation is enhanced by transpressional features (white arrows), as shown by two topographic profiles that cross a sharp right-lateral restraining bend (dashed lines and inset a1). (b) Within the basin, the S2 branch strikes SW–NE, bending northward as it approaches the northern basin rim. This branch also shows evidence of lateral movement in the form of a positive flower structure (red arrows). Between the scarp and the basin-related structures, a set of minor lobate scarps has developed (white dashed arrows). Concerning basin-related features, the ring of wrinkle ridges seems to predate radial graben (white arrow). Superposed craters C3, C4a, and C4b host minor contractional structures that may reflect later phases of thrusting, as shown in the topographic profile across crater C4a (dashed line and inset b1). Crater Cm masks the cross-cutting relationships between S2 and the basin-related features. A shorter thrust parallel to the upper portion of S2 is shown as "s2" with a white arrow.

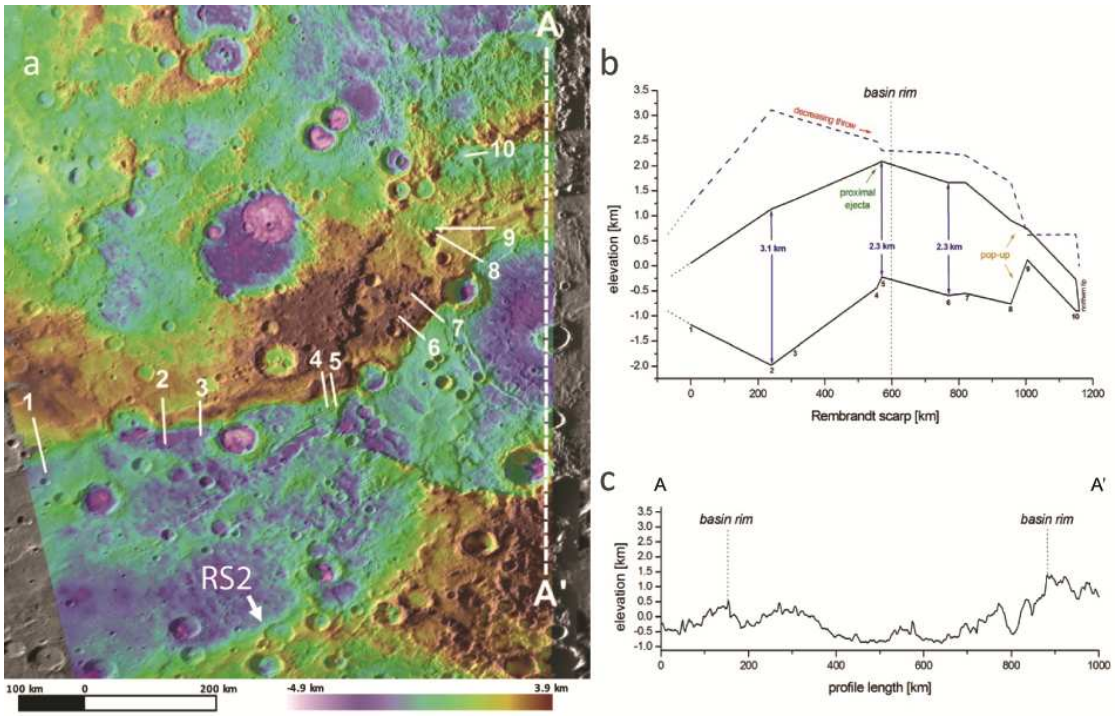

Figure 2.8. The topography of the Rembrandt basin and scarp system. (a) A flyby DTM (Preusker et al., 2011) of the Rembrandt basin overlaid upon a MDIS monochrome flyby mosaic. The topographic profiles shown in (b) are indicated in white. (b) Interpolation of maxima and minima values of the topographic profiles shown in (a), displaying the elevation of the scarp and the related vertical displacement. The calculated throw (blue dashed line) increases to a maximum along S1, and then decreases toward the basin rim, before flattening along S2 and newly decreasing toward the tip. (c) Topographic profile along the basin diameter (transect A-A' in a).

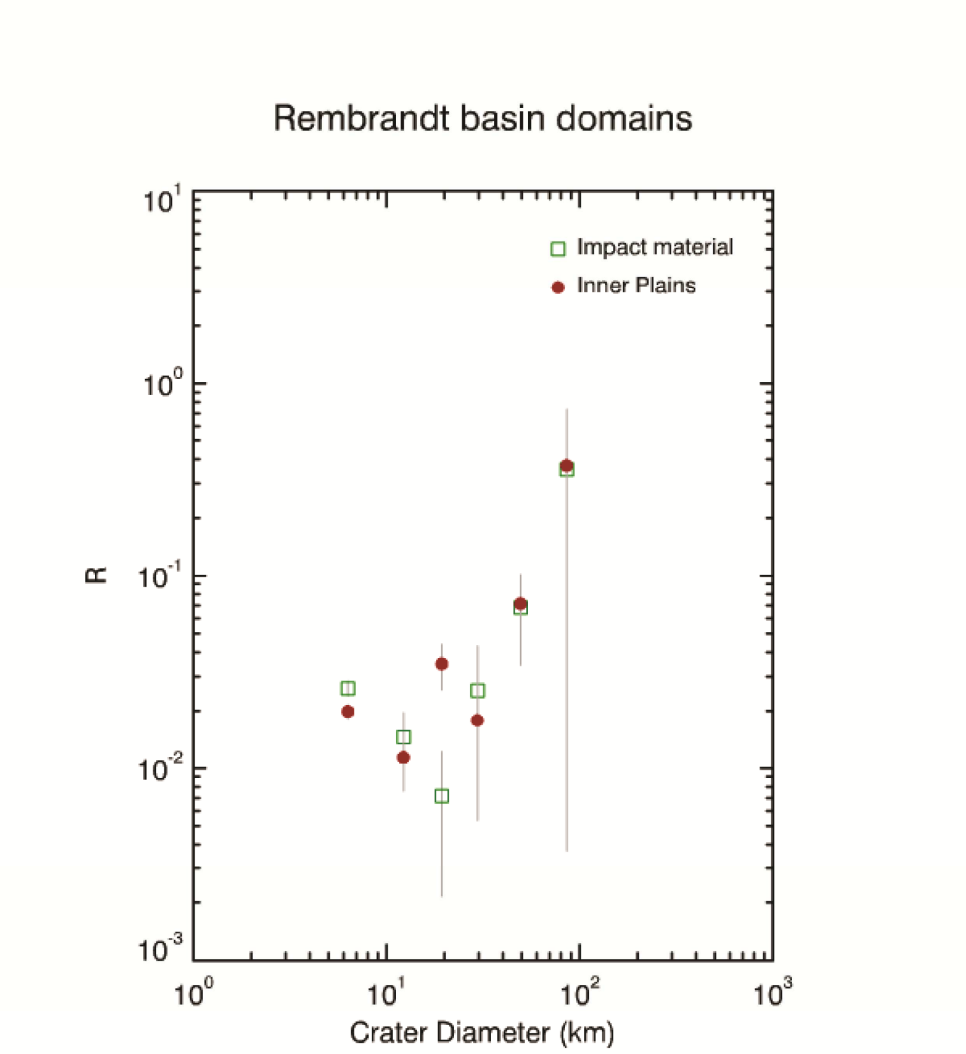

Figure 2.9. *R*-plot of Spatial Density Distributions (SDFs) of craters in the impact and interior units within Rembrandt basin, using crater diameters greater than 4 km (Crater Analysis Techniques Working Group, 1973). The SDF of IPa (red filled points) is compared to that of HM and PE (green squares), both binned by diameter increments of a factor of √2. Errors shown for each point are from counting statistics alone ($R/\sqrt{n}$, where n is the number of craters counted in each diameter interval). The relative ages of the two domains are not statistically resolvable, since in most cases the bins lie within the error bars. An exception is centered at 20-km-diameter craters, and represents a greater density for such sized craters in IPa than for HM and PE. This effect may be due to the fact that the resurfacing cannot completely bury and hide carters larger than about 20 km, which have been collected within IPa as they postdate the resurfacing.

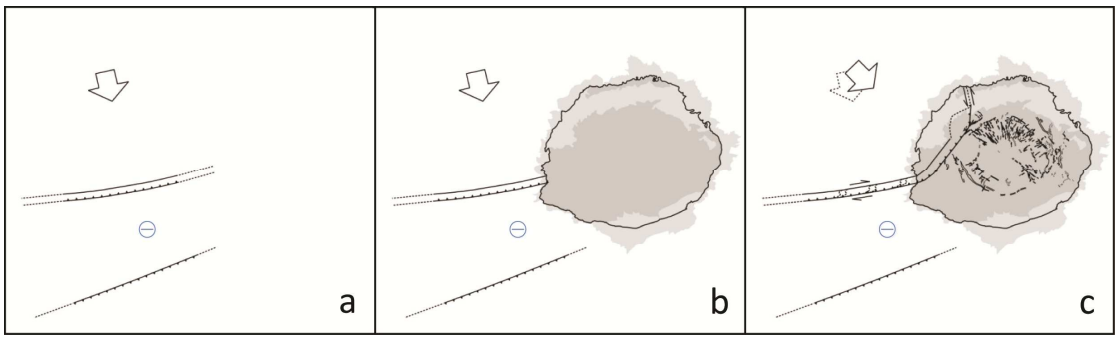

Figure 2.10. Our preferred formation scenario for the Rembrandt basin and scarp system. (a) A pre-existing ridge (an early S1) with an overall WSW–ENE strike faces a wide foreland basin and a parallel scarp with opposite vergence (RS2 in Ruiz et al. 2012). (b) The formation of the giant Rembrandt basin erases part of the ridge. (c) Crustal flow toward the basin center induces a perturbation of the regional stress field, influencing the strike and growth of the subsequently formed S2 scarp segment.

2.3.2 The long-lasting activity of Rembrandt Basin and scarp system, Mercury

Abstract

Rembrandt basin is the largest well-preserved impact feature of the southern hemisphere of Mercury. Its interior shows a wide smooth high-reflectance infilling, which is characterized by an intense basin-related tectonic pattern along cut by a prominent contractional scarp. The emplacement of the interior smooth plains, interpreted to be volcanic material, predates both the basin-related tectonism and the final development of the giant scarp, which is suggestive of either short-lived volcanic activity immediately after the basin formation or a later volcanic phase set against prolonged tectonic activity. Several basin-related structures maintain the same strike or even lay on the top of the giant scarp, predating its complete development.

In order to quantify the duration of volcanic and tectonic activities in and around Rembrandt basin, we determined the crater count-derived ages of the involved terrains. On the basis of age determination via Model Production Function crater chronology, our analysis on the basin-related material (i.e., hummocky terrains and proximal ejecta) confirmed the formation of the Rembrandt basin during the end of the Late-Heavy Bombardment, at 3.78±0.03 Ga. We also constrained the smooth plains emplacement between 3.72±0.05 and 3.52±0.10 Ga, applying a distinction between the primary population and the smaller craters that occurred after the resurfacing of the basin floor. These ages place the oldest smooth layer formation during or soon after the impact event, and so we cannot definitively determine from our crater counts whether those plain are impact melt or volcanic material; conversely, the youngest smooth covers (3.52±0.10 Ga) result temporally unrelated to the basin formation, and should be attributed to volcanism. We detected the same chronological relationship for the terrain bordering the basin at the foot-wall of the giant scarp, where the primary crater population of the older layer predates the basin formation at least of 100 Myr, while the younger unit (3.59±0.14 Ga) revealed by smaller craters is temporally similar to the interior smooth plains of Rembrandt basin. Hence, the volcanic activity affected both the basin and its surrounding, but ended prior to some basin-related and regional faulting. If the giant scarp formed before the Rembrandt basin formation, the regional tectonic activity along this structure might have lasted for more than 300 Ma.

Introduction

The known picture of the early surface of Mercury implies a thin crust accreting planet that undergoes to an intense cratering period (Late Heavy Bombardment, 4-3.8 Ga). The global contraction of the surface due to the cooling of the planet was probably the main cause of formation of the giant mercurian lobate scarp (e.g. Watters et al. 2004), whose activity began during the Late Heavy Bombardment and continued until and after the emplacement of the youngest smooth plains (Strom, 1975; Melosh and McKinnon 1988; Watters et al. 2009b). Other mechanisms inducing compression could

have coexisted with thermal contraction: early tidal despinning (Dombard and Hauck, 1988), mantle convection (King et al. 2008; Watters and Nimmo 2010; Michel et al. 2012) and regional stress field induced by giant impacts (Thomas et al., 1988). In parallel, the structural patterns related to basins and buried craters on Mercury (Watters et al. 2009a; Head et al. 2011; Freed et al. 2012) seems to result from the emplacement of low-viscosity lava flows that rapidly accumulated thick cooling units in a global contractional system (Watters et al. 2012a; Klimczak et al., 2012). Within the largest basins, the load of volcanic overlays could have induced subsidence and the consequent formation of radial and concentric wrinkle ridges (Watters et al., 2009c, Watters et al. 2012a). Vertical motions (Dzurisin 1978; Melosh and Dzurisin 1978; Blair et al. 2012) or inward flow of lower crustal material (Watters et al. 2005; Watters and Nimmo 2010) triggered by the basin formation could have promoted following uplifts of the basin centers and the formation of graben. Alternatively, regular extensional features can be induced by the thermal contraction of rapidly emplaced lava flow on the basin floor (Byrne et al. 2013 and reference therein).

Under this scenario, the 715-km-diameter Rembrandt basin formed in the southern hemisphere (Watters et al. 2009b), reaching tens of kilometers in depth and undergoing to the resurfacing of the floor by volcanic material along a prolonged compressional system. Rembrandt basin was imaged for the first time during the second flyby of the MErcury Surface, Space ENvironment, GEochemistry, and Ranging (MESSENGER) spacecraft. As described by Watters et al. (2009b), much of the basin interior is covered by smooth, high-reflectance plains interpreted to be of volcanic origin (Denevi et al. 2009) that hosts sets of contractional and extensional tectonic structures (Fig. 2.11). This pattern resembles the arrangement of structures observed within the Caloris basin (Murchie et al. 2008; Watters et al. 2009c; Byrne et al. 2012b), with individual sets of radial and concentric landforms most likely due to multiple episodes of deformation (Strom et al. 1975; Melosh and McKinnon 1988; Watters et al. 2005; Watters et al. 2009c). Notably, Rembrandt basin and its smooth plains are cross-cut by a 1 000-km-long reverse fault system (Watters et al. 2009b; Byrne et al. 2012a) that trends ~E–W, bending toward the North within the basin (Fig. 2.11). The individual faults of this system accommodated crustal shortening that resulted from global contraction as Mercury's interior cooled (Watters et al. 2009a). The current shape of the reverse fault system may have been influenced by the formation of the Rembrandt basin (Ferrari et al. 2012).

As the Rembrandt basin area was affected by many commonly found processes that modified the surface of Mercury (i.e., basin formation and impact gardening, global and basin-related tectonics, and volcanic resurfacing) it is well suited for understanding the sequence and duration of such processes. This work attempts to establish a chronological order of events, dating the involved objects. Hence crater counts have been performed on each terrain, in order to estimate the ages by applying the Model Production Function (MPF) of Marchi et al. (2009), whereas cross-cutting relationships have been assessed for terrains and structures. The aim is understand where, when and how volcanism coexisted with contractional tectonism in the Rembrandt basin area.

Geological units and cross-cutting relationships in and around Rembrandt basin

Geological map of Rembrandt basin and scarp system in Fig. 2.11 was mainly derived by the work of Ferrari et al. (2012) on MESSENGER images. The overall units have been identified on the base of the surface texture pattern and their stratigraphic relationships: the *Hummocky Material* and the *Interior Plains* fill the basin, whereas the *Proximal Ejecta* surround the basin rim. The Hummocky Material consists of a mixture of impact melt and ejecta deposits (breccias) that formed during the impact event and stand out for the thick alternation of hills, depressions and higher knobs, which are characteristic features for such large basins (e.g., Cintala and Grieve 1998). In the case of Rembrandt, the Hummocky Material is mostly buried by widespread smooth Interior Plains or appears strongly reworked by subsequent impact events that involved the Proximal Ejecta, erasing the basin rim and making difficult a clear discrimination of the two units. The Proximal Ejecta unit is composed of thick, coherent ejecta following the rim crest, and is likely coeval with the Hummocky Material unit. The smooth Interior Plains are brighter than the basin-formed materials, and Denevi et al. (2009) associated the high reflectance they show to a volcanic origin. This unit covers most of the basin floor with two distinct exposures (Fig. 2.11), whose most extensive blankets the central portion of the basin, extending from the western to the eastern rims. A first size-frequency distribution (SFD) of superposed impact craters on the Rembrandt basin rim were determined using MESSENGER orbit data (Ferrari et al. 2012), in order to compare the relative ages of the major domains of Rembrandt basin. In that study, the differences in crater densities between the impact-forming material and the central Interior Plains are almost negligible and cannot discriminate whether these latter are impact melt formed during basin formation, or volcanic material emplaced soon after the basin formation. In addition, on MESSENGER multispectral mosaic these smooth plains show color variegation (Ferrari et al. 2012), which has been alternatively attributed to a different stage of surface maturity or a different composition (Robinson and Lucey 1997; Blewett et al. 2007; Robinson et al. 2008; Murchie et al. 2008). On the SW rim, the darker Interior Plains become also texturally indistinguishable from the surface exterior to the basin, suggesting a common origin or the same stage of maturity. Interior Plains and this exterior terrain, from here onward named *Outer Plains*, however, display several partly buried craters (e.g. craters marked with black arrows in Fig 2.12), suggesting a partial or overall volcanic resurfacing. In addition, the proximal ejecta of Rembrandt basin placed within the Outer Plains seem to be smoothed with respect of the rest of basin proximal ejecta (Fig. 2.12).

Both the basin-oriented pattern and the giant lobate scarp affect the Interior Plains (Fig. 2.11), (at least) partially postdating their formation, whereas the Outer Plains seems to be limited to the foredeep at the foot-wall of the scarp. In the SW sector of the basin, several scarps nucleated along orientations similar to those of basin-related structures and two of them cross-cut the basin rim and extend into the Outer Plains (white arrows in Fig. 2.12), postdating both the adjoining smooth units (i.e. Interior Plains and Outer Plains). We regard these observations as suggestions of a sustained tectonic activity that hold over the volcanic emplacement in and around Rembrandt basin.

The Model Production Function chronology applied on the surface of Mercury

Age determination of geological units using crater Size Frequency Distributions (SFDs) is based on the fact that older surfaces have accumulated more craters than younger ones. The ages of the Rembrandt basin units have been obtained by means of the Model Production Function (MPF) chronology of Mercury (Marchi et al. 2009; Massironi et al. 2009), which relies on the knowledge of the impactors flux on the planet. The flux is converted into the expected crater Size Frequency Distribution (SFD) per unit time per unit surface by the crater scaling law of Holsapple and Housen (2007) that takes into account the properties of the target material (strength, density, etc.). The absolute age calibration is provided relating the Apollo and Lunar landing site radiometric ages with the corresponding cumulative number of 1-km-diameter craters.

The *hard-rock* crater scaling law or the *loose-materials* one can be adopted, depending on the recognized properties of each unit, since as demonstrated by Marchi et al. (2009) target parameters like bulk structure, density and strength affect the deformation of the hit terrain. These parameters are tabulated for several material like cohesive soils, hard-rock and porous materials (e.g. Melosh 1989; Holsapple and Housen 2007). Since sizable craters can involve more than a single crustal layer (Massironi et al. 2009; Marchi et al. 2011), it is crucial to identify the local geological history (stratigraphy). Then the so-called Pi-scaling law has been adopted in the formulation by Holsapple and Housen (2007), which allows computing the transient crater diameter as a function of impact conditions (i.e. impactors size and velocity) and target properties (density, tensile strength, cohesion and porosity). In addition, a transition of the crater scaling law from loose-materials to hard rock materials can be considered according to the size of the impactors, since the coherence of the terrain may considerable increase with depth, in agreement to what seen in seismic profiles of the lunar crust (Toksoz et al. 1973). The upper crustal layers of a mature planetary surface remain profoundly fractured by the continuous bombardment, then craters affecting only the upper layers of older terrains form in cohesive-soil regime, whereas larger craters form in hard-rock regime. The depth of transition (H) - and therefore the crater size - from one regime to the other is reflected by a step in the crater SFDs, which can be fitted by the appropriate MPF curves (Massironi et al. 2009, Marchi et al. 2011).

On the other hand, considering the crater SDFs collected on *lunar* surfaces, Neukum and Horn (1975) assumed that the observable steps are always markers of resurfacing by endogenic lava flow processes, even in those cases where the morphological recognition of the flows has not occurred. In this case, the steps are indications of *composite* SFDs in which smaller craters reflect the age of the younger units, whereas larger craters reproduce the age of the older units. According to this view, Hiesinger et al. (2002) suggest that the step of crater SFDs of several *lunar* nearside basins indicates the presence of two lava flows units separated in time, and that the diameters at which this bend occurs are related to the thickness of the overlaying units. The deflection of the step that occurs at higher diameters corresponds to the extinction of the smaller craters of the primary craters population. The deflection that occurs at smaller diameters corresponds to the post-flooding craters population (Hiesinger et al. 2002 and reference therein). Considering the rim height/diameter (h/D) relation fixed for Mercury by the power laws of Pike (1988), the crater diameters where these deflections occur can be

used to estimate the minimum and maximum thickness of the younger unit. The h/D relation of Pike (1988) depends on the interior morphology of the craters themselves, thus the relative near-isometric trends have been distinguished in size classes as below

(1) $h = 0.052\ D^{0.930}$ *bowl shaped craters* with $2.4\ km \leq D \leq 12\ km$

(2) $h = 0.150\ D^{0.487}$ *immature-complex craters* with $13\ km \leq D \leq 43\ km$

The minimum ($h_{min)}$ and maximum thicknesses ($h_{max)}$ of the younger unit can be estimated using the diameters (D) at which the crater SFD deflections occurs (Hiesinger et al. 2002).

Neukum and Horn (1975), however, consider that the crater SFD step depends on the resurfacing by endogenic lava flow processes *a priori*, whereas the use of MPF imply the attribution of the step to the rheological layering (fractured material over hard rock) or alternatively to the resurfacing. Thus, for deriving a more accurate age estimate, it is fundamental adapting the crater production function to the nature of the terrains investigated.

MPF applied on Rembrandt area

We performed crater counts on each geological domain of Fig. 2.13a on MESSENGER mosaics (Sept. 2012 release of NASA/Johns Hopkins University Applied Physics Laboratory/Carnegie Institution of Washington; average spatial resolution of 250 m/pixel), using the ESRI ArcMap CraterTools extension developed by Kneissl et al. (2011) that allows neglecting the distortion of circular shapes related to utilized map projection. Since crater age determination is based on the primary craters (bonafide craters, i.e. those formed by impacts with objects in heliocentric orbits; Melosh, 1989), we avoided considering cluster and chains of craters during the collection. The contribution of far-field secondaries, which are normally not distinguishable from primary craters (e.g. McEwen and Bierhaus, 2006), has been neglected.

The cumulative bonafide crater SFDs for the considered areas are shown in Fig. 2.14, along with the MPF model ages. The old age of the Rembrandt basin suggested by Watters et al. (2009b) has justified the use of the Main Belt Asteroids (MBA) population as prime source of impactors for MPF, since it best represents the cratering on the oldest terrains of Mercury (Strom et al. 2005; Marchi et al. 2009). The age assessment has been performed assuming a specific rheological layering for each considered terrain. For instance, the volcanic infilling of Rembrandt basin partly strengthened or even completely replaced the pre-existing fractured layer, thus the fractured horizon can be confined within a very thin negligible regolith cover. Conversely, the ejecta of Rembrandt basin can be considered as deeply fractured material. Applying MPF, we decided to consider resurfacing where buried craters and embayment relationship on likely unfractured geological unit (i.e. smooth plains) were recognizable.

We firstly performed the primary craters count of the Rembrandt basin-formed material (Fig. 2.13a), in order to confirm the Calorian age suggested by previous works (Watters et al. 2009b; Fassett et al. 2012). The basin-formed unit corresponds to the hummocky material along with the coeval proximal ejecta. Craters considered for this

unit are shown in Fig. 2.13b. The resultant crater SFD shows a distinct step for crater diameters between 17 and 30 km (Fig. 2.14a). The occurrence of few very large craters in a relatively small area might cause a statistic effect that appears as a step along the SFD curve, which in the MPF context may lead to misleading conclusions on the target rheology and layering. In order to exclude this effect, we removed from the relative crater SFD the two major craters present in the counting area of the basin-related material (C11 and C12 in Fig. 2.13, respectively 79 and 97 km of diameter). As shown in Fig. 2.14b, the step in the crater SFD still persists, therefore it can be taken into account as a stratigraphic marker. This is consistent with the fact that hummocky material and proximal ejecta of Rembrant basin are most likely made up of fractured-over-harder material and have no evidence of resurfacing that harden the upper layer. The resulting S-shape of the MPF curve finds a correspondence in the crater-SFD step (Fig. 2.14a) and suggests a thickness of 3.5 km for the upper heavily fractured layer and provides an age of 3.8±0.1 Ga (Fig. 2.14a). We applied the same counting method on the smooth plains located within the Rembrandt basin rim (Fig. 2.13a). For the purposes of age determination, we considered only the more extended of the two Interior Plains exposures (Fig. 2.13), neglecting the northern slice that embays the basin rim. Craters counted for this unit are shown in Fig. 2.13b. We detected several craters partially buried (e.g. Fig. 2.13a), attributing their infilling to the resurfacing of the basin floor. Since this infilling have a hardening effect on the upper fractured layer of the basin, we assumed the hard rock scaling low (Holsapple and Housen 2007) for the MPF application. The crater SFD of this central Inner Plains (Figs. 2.14c and 2.14d) shows a step for crater diameters between 8 and 15 km. Because of the detected resurfacing, we interpreted this step as the product of a *composite* crater SFD that describes both the younger cover and the older underlying unit. Hence, we fitted MPF curves both for the larger craters and the smaller ones. The MPF best fit for larger craters correspond to an age of 3.7±0.1 Ga (Fig. 2.10c) and for the smaller craters at 3.5±0.1 Ga (Fig. 2.14d), indicating two distinct smooth layers within the same unit. This result does not clarify the origin of the older layer, which according to its MPF age (3.7±0.1 Ga) could be either melt formed during the impact event or volcanic material emplaced soon after the basin formation. On the contrary, considering its 3.5±0.1 Ga MPF age, the younger smooth layer should be attributed to the later resurfacing of the basin floor by volcanic materials. Hence, the crater population formed on the basin floor soon after its formation defines the primary production size-frequency fitted in Fig. 2.14c; a subsequent resurfacing event was able to completely cover several of those craters with a direct proportion between thickness of the flow and diameter of the covered craters (the thicker is the flow the larger are the erased carters). Using the rim height/diameter relation fixed for Mercury by Pike (1988), for the younger Interior Plains we obtained a minimum thickness $h_{min\text{-}IP}$ of 0.36 km considering the first crater SFD deflection at 8 km (1) and a maximum thickness $h_{max\text{-}IP}$ of 0.56 km considering the second crater SFD deflection at 15 km (2).

We performed an additional crater count on the Outer Plains bordering the Rembrandt basin at the foot-wall of the giant scarp (Fig. 2.13a), in order to verify a possible relationship between the Interior Plains and the outer ones, which display textural and reflectance similarities. Craters considered for this unit are shown in Fig. 2.13b. Within this unit, we should take into account the presence of largest secondary carters originated by the giant impact. Since the Outer Plains manifest resurfacing (e.g. black arrow in Fig. 2.12) and their crater SFD shows a step for carter diameters between

5 and 15 km (Figs. 2.14e and 2.14f), we applied the same constraints used for the Interior Plains. We assessed the MPF best fit for larger craters at 3.9±0.1 Ga (Fig. 2.14e) and for smaller craters at 3.6±0.1 Ga (Fig. 2.14f). Using the rim height/diameter relation fixed for Mercury by Pike (1988), for the younger Outer Plains we obtained a minimum thickness $h_{min\text{-}OP}$ of 0.23 km considering the first crater SFD deflection at 5 km (1) and a maximum thickness $h_{max\text{-}OP}$ of 0.56 km considering the second crater SFD deflection at 15 km (2). Hence the results are comparable with the thickness estimates related to the younger volcanic unit of the Inner plains.

Discussion and Conclusions

On the basis of MPF results, the terrains set outside Rembrandt basin at the foot-wall of the scarp (i.e. older Outer Plains dated at 3.9±0.1 Ga) possibly represent a pre-basin unit and could be considered Heavy Cratered Terrain (Trask and Guest 1975). The basin formation has been defined at 3.8±0.1, hence the Calorian age suggested by previous works (Watters et al. 2009b; Fassett et al. 2012) is now well-fixed by a specific model age. Since younger materials have been dated both in the central Interior Plains and in the Outer Plains, we conclude that a later stage of volcanic resurfacing involved the basin floor and its surrounding, covering the basin rim and ejecta at its south-western margin and ending approximately 3.5±0.1 Ga ago. The emission sources responsible of this later volcanic stage can localized both within and outside the basin. MESSENGER has revealed volcanism within and surrounding the Caloris basin that appears to be younger than the basin itself, and thus cannot be impact melts (Head et al. 2009). At this regards, the thermo-chemical convection models of Roberts and Barnouin (2012) suggest that the thermal impulse due to large impacts as the Caloris can alter the underlying mantle dynamics, producing subsequent (younger) volcanism far from the impact site. However, on Mercury as long as on the Moon, it is likely that the emission sources formed inside the basin, in particular along the margins of the basin floors, because of its intense fracturing that favors the uprising and effusion of deeply generated pre-existing magmas (Melosh 2011). In this case, we should suppose that lavas generated within basin may have spread toward pre-existed topographic lowers as the foredeep located outside the basin at the giant scarp foot-wall. This preferred flow direction would imply that part of the scarp predate the last lava flow emplacement. Within the basin, the depletion of magma chambers combined with the load of lava flow may have caused the subsidence of the floor. The collapse could have reactivated the rim margins and induced a first stage of contractional features in the central Interior Plains (i.e., concentric wrinkle ridges). In addition, this event could have likely provided horizons of weakness for the nucleation of the scarps developed across the rim in the SW Outer Plains spilling area. The emplaced lava flows within the basin may have rapidly cooled undergoing thermal contraction that could have produced basin-oriented graben.

The recognized volcanic resurfacing affected Rembrandt basin and the surroundings long after the basin formation and ended before the declining of the basin-related and regional tectonic activities. Taking into account that the giant scarp might nucleated before the basin formation (Ferrari et al. 2012) at the end of the Late Heavy Bombardment and that the younger plains might be cross-cut by the scarp itself, the

global tectonic activity could have been active from 3.8±0.1 to at least 3.5±0.1 Ga, lasting long over 300 Ma. A similar extent (1) would confirm inferences resumed by Fassett et al. (2012) on the longer coexistence of volcanic and tectonic activities and (ii) would imply an average slow strain rate that is congruent with thermo-mechanical models predicting a contractional tectonism longer than 0.5 Ga (e.g. Dombard and Hauck 2008).

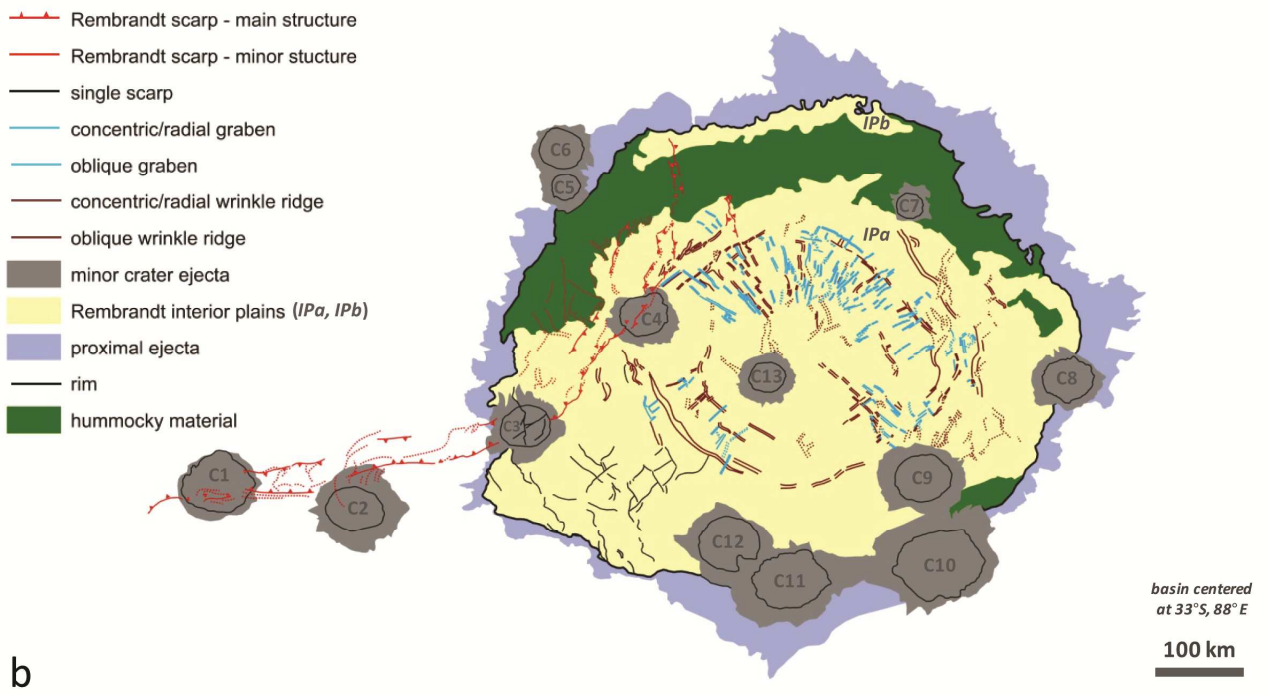

Figure 2.11. Geological and structural map of the Rembrandt basin and scarp system.

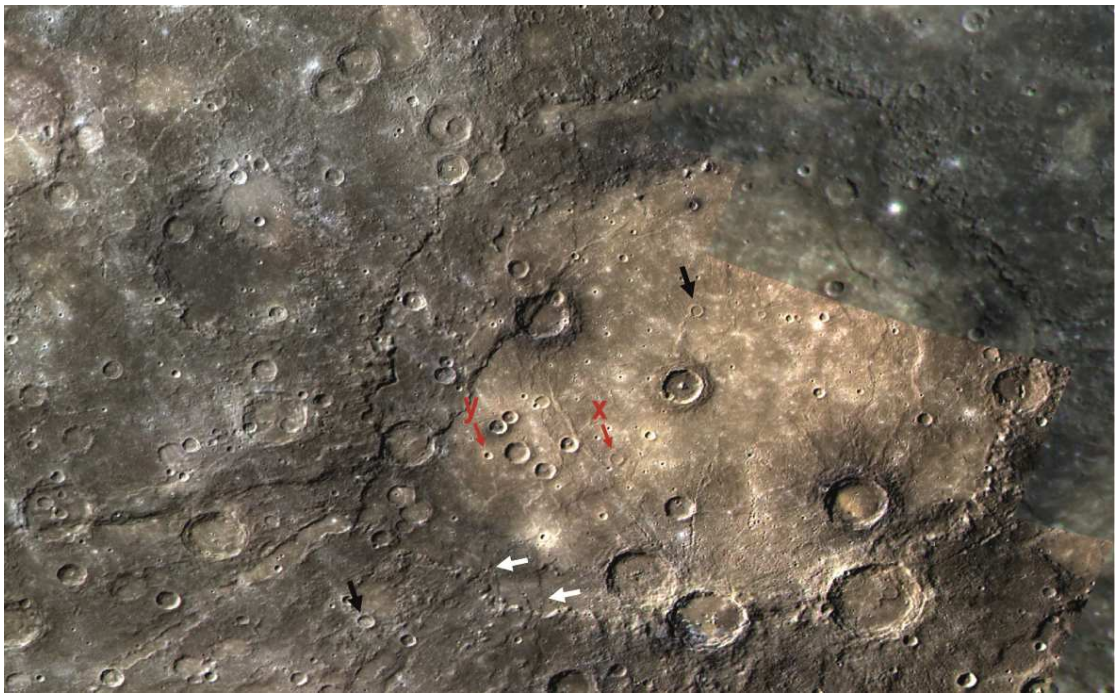

Figure 2.12. MESSENGER Mercury Dual Imaging System (MDIS) wide angle camera multispectral mosaic (band 8 at 947.0 nm, band 5 at 628.8 nm, and band 3 at 479.9 nm for red, green, and blue, respectively) showing color variegation within IPa: while retaining the same texture, Interior Plains become darker toward the basin rim. A set of scarps cuts through this unit and extends beyond the basin rim and into the Proximal Ejecta that in this area are less manifest. Several craters (e.g. crater X) within Interior Plains remain partially covered and then countable despite the flows emplacement. The continuing impact cratering forms a new craters population on the top of the younger smooth overlay (e.g. crater Y) that can be used to estimate the end time of the last resurfacing event (Hiesinger et al. 2002). Partially filled craters (e.g. black arrow) are present also outside the basin.

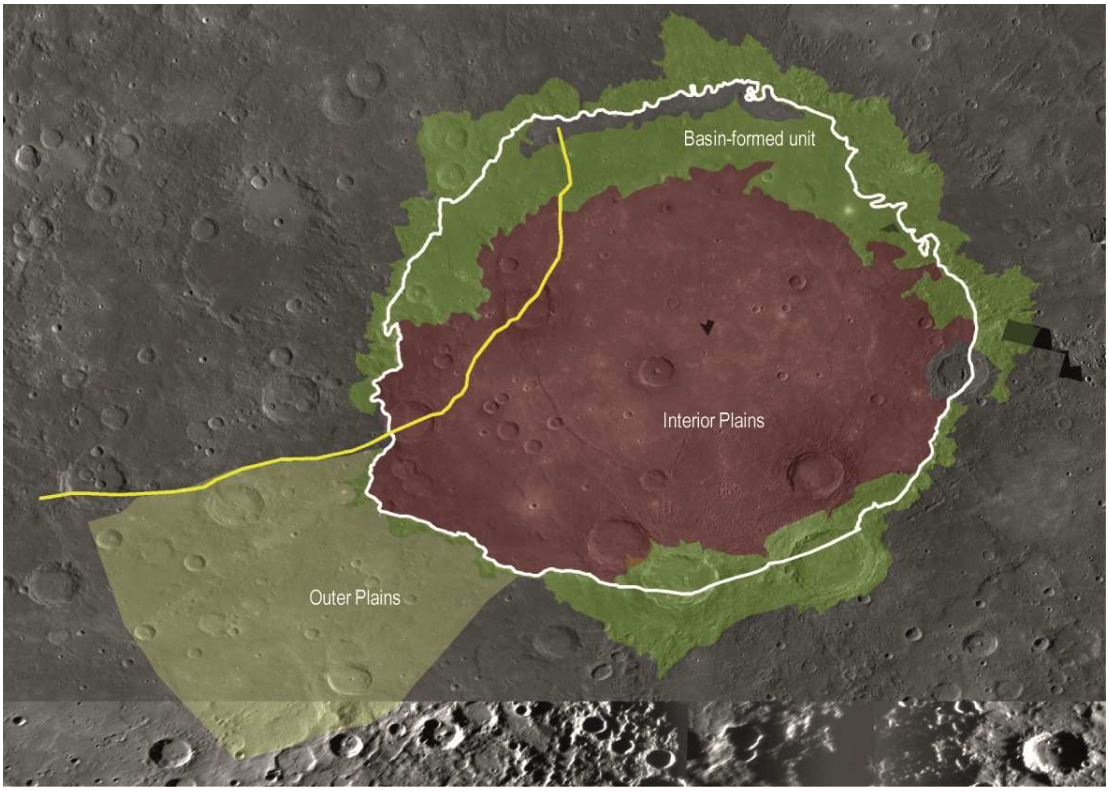

Figure 2.13. Units of the Rembrandt basin region on which crater-counts were performed displayed on the MESSENGER Mercury Dual Imaging System (MDIS) 750 nm mosaic (average spatial resolution: 250 m/pixel): green line bounds the crater-counting area of basin materials (i.e. Hummocky Material and Proximla Ejecta), red lines bounds the crater-counting area of Interior Plains, yellow line bounds the crater-counting area of Outer Plains.

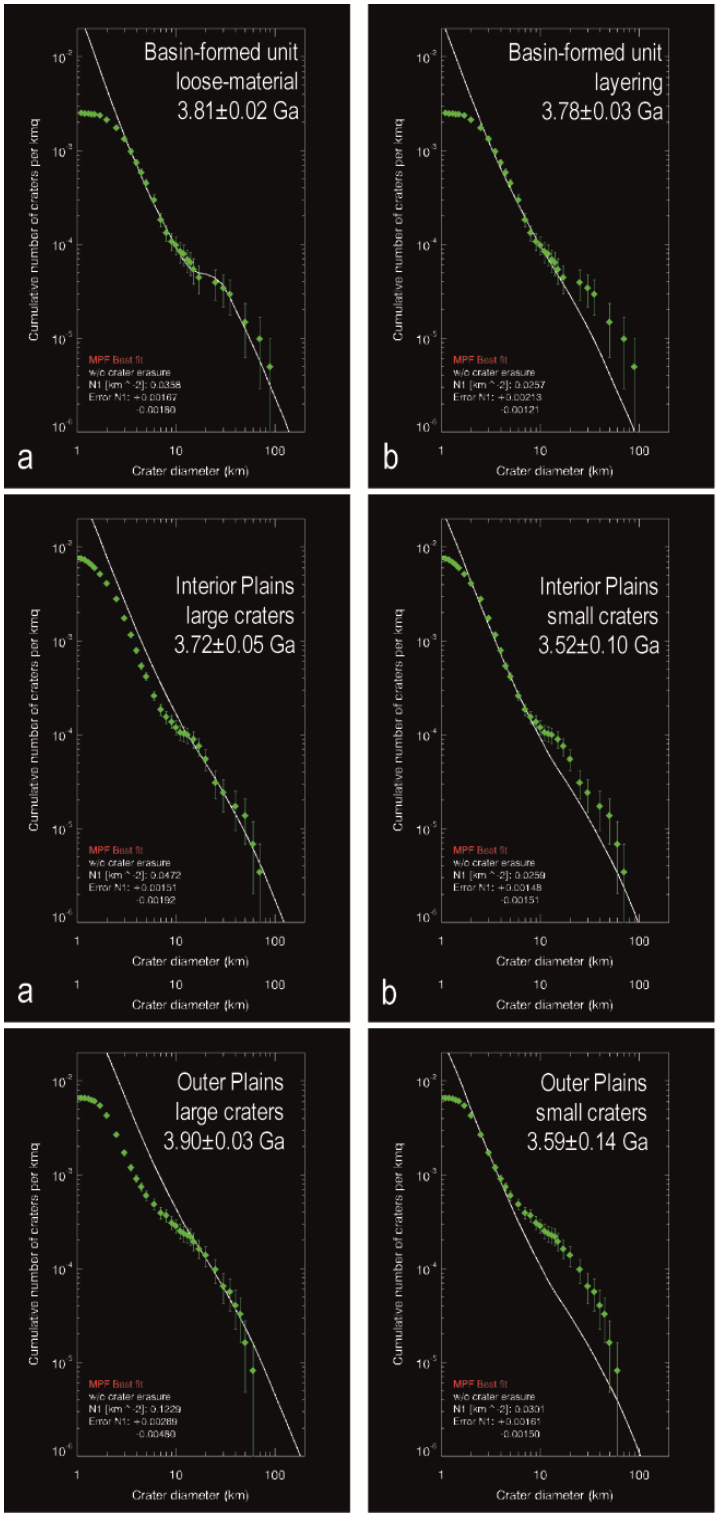

Figure 2.14. MPF minimum χ^2 best fit of the cumulative crater count distributions determined for Rembrandt Basin. For each unit we report the age assessment for Main Belt Asteroids populations. Error bars correspond to a variation of the minimum χ^2 of ±xx%. a) Basin-related materials (i.e. Hummocky Material and Proximal Ejecta) best fit obtained considering fractured layer (i.e. loose-material) of 3.5 km (H) over hard rocks. b) Basin-related materials best fit obtained subtracting craters and area related to the two major craters (see text for explanation) and considerenig the same target constrain of (a). c) Interior Plains MPF best fit of larger craters obtained using hard rocks as target material. d) Interior Plains MPF best fit of smaller craters obtained using hard rocks as target material. e) Outer Plains best fit of larger craters obtained using hard rocks as target material. c) Outer Plains best fit of smaller craters obtained using hard rocks as target material.

3. Composition of the surface of Mercury: high-temperature and minerals

3.1. Thermal Infra-red (vibrational) spectroscopy

Spectroscopy in the Thermal Infra-red (TIR) region (~8.50-50 μm) is based on the principle that the interaction of photons with molecules, atomic groups and even the whole lattice in crystals produces absorption at specific wavelength (e.g., Farmer 1974). It is also is referred to in the literature as vibrational spectroscopy, because within this range spectral features arise from the fundamental vibrational modes of the material. Because all minerals, by definition, have unique structures and/or compositions, virtually every mineral has a different suite of vibrational absorption characteristics and thus a unique spectrum in the thermal infrared. In silicate minerals the primary spectral absorptions (reststrahlen bands) are due to the stretching and bending motions in the silicon–oxygen anions. Additional absorption features result from metal–oxygen and lattice vibrations. The exact frequencies, shapes, intensities, and number of features in a mineral's spectrum are dependent on the relative masses, radii, distances, and angles between atoms and their bond strengths. These parameters are determined by the structural arrangement of the anions (i.e., their polymerization), and the location and composition of the cations associated with them (Hamilton 2010). Thus the spectral "signature" of each mineral serves as a means of identifying that mineral. Furthermore, the spectra of a rock's constituent minerals add approximately linearly in the thermal infrared to produce the rock's spectrum because very high absorption coefficients result in few multigrain interactions. Therefore the composition of a rock may be determined by linear deconvolution (Christensen et al. 2000, and reference therein).

Beyond emission spectroscopy, several spectroscopic techniques are capable of measuring the fundamental vibrational modes of minerals, including transmission, reflection, attenuated total reflection (ATR), and Raman. Emission spectra, however, are currently used for determining the composition of planetary materials and surfaces, since it acquires spectra in a similar manner to remotely sensed data. This similarity allows for direct, quantitative comparison of laboratory spectra to remote sensing data sets. Although a significant number of minerals have been well-characterized by means of TIR spectroscopy (e.g. Christensen et al. 2000) in our knowledge no data on in situ TIR measurements have been published so far with the exception of those of Herbert and Maturilli (2009) on a labradorite plagioclase. On the other hand, previous works (e.g, Bowey et al. 2001; Chihara 2001; Koike et al. 2006) investigated the effect of temperature on Near Infra-Red spectra of olivine. In particular, Koike et al. (2006) and Chihara et al. (2001) investigated the effect of temperature on the spectra of olivine circumstellar and interstellar dust particles (crystal size < 1 μm), therefore they are out of target with respect to the investigation of the Mercurian surface.

3.2 Experimental method

3.2.1 Samples overview

High-purity mineral samples considered among the most likely constituents of the hermean surface regolith (Warell et al. 2010) were used for mineralogical determination. We report below the families for which we completed the analysis set.

Olivines [solid solution between forsterite (Fo). Mg_2SiO_4, and fayalite (Fa), Fe_2SiO_4]. These minerals constitute about 60% of the Earth's upper mantle and are a very common phase in several meteorites. The presence of olivine has been considered in several petrological models of Mercury (e.g., Brown and Elkins-Tanton 2009; Riner et al. 2010) and should likely be a primary mineralogical phase in the wide volcanic plains recently discovered on its surface (Head et al. 2011), particularly if MESSENGER X-ray observations pointing to basic and ultra-basic compositions (Nittler et al. 2011). Although MESSENGER spectra were not able to definitively solve the presence of olivine, Sprague et al. (2009) detected magnesium-rich olivine by ground-based Mid-infrared spectroscopic measurements.

Na-free clinopyroxenes (cpx) [$(Ca,Fe,Mg)_2Si_2O_6$] Together with orthopyroxenes, these minerals constitute about 20% of the Earth's upper mantle and are again a very common phase in several meteorites. These minerals can be characterized by a strong chemical complexity. Concerning Mercury, several ground-based observations pointed out that Ca-rich (and low-Fe) clinopyroxenes could be common constituent minerals of its surface, with diopside and augite considered as good possible candidates (i.e. Sprague et al. 2002; Sprague et al. 2007; Sprague et al. 2009).

3.2.2 Planetary Emissivity Laboratory (PEL)

The facilities available at Planetary Emissivity Laboratory (PEL, Institute of Planetary Research, Deutsches Zentrum fuer Luft- und Raumfahrt, Berlin) allow measurement of the emissivity of heat-treated samples under vacuum (Herbert and Maturilli 2009). The selected crystals were firstly polished in order to eliminate surface oxidations and deposits. Each single mineral phase was fully characterized at room conditions by X-ray powder diffraction and single crystal X-ray diffraction, and analyzed by electron microprobe (Wavelength-Dispersive System method, which allows high-accuracy chemical analysis thanks to its high peak resolution). Subsequently, each single mineral phase was reduced toward the largest end-members suggested by Emery et al. 1998 for the regolith of Mercury (i.e. 30 µm and 100 µm, Fig. 3.1). See *P3*.3 for details.

The instrument used is a Bruker Vertex 80V Fourier Transform Infra-Red (FTIR). It has a useful high spectral resolution (better than 0.2 cm^{-1}) for characterize temperature effects and it can be operated under vacuum conditions to remove atmospheric features from the spectra (Helbert and Maturilli, 2009). To cover the interested part of spectral range, from 1 to 16-18 µm, a liquid-nitrogen-cooled HgCdTe micro-thermocouple detector and a KBr beamsplitter were used to measure the coated steel blackbody and then the target. The spectrometer is coupled to an evacuated planetary simulation

chamber, having an automatic sample transport system (carousel, Fig. 3.1) to maintaining the vacuum while changing the samples. The steel of the sample cups is heated via a copper induction pancake coil, ensuring that the surrounding remains cold into the chamber. The emissivity measurements can be carried out at different steps of temperature and in vacuum (under 1 mbar of pressure; Maturilli et al. 2008), acquiring spectra between 1 and 16 µm at a resolution of 4 cm^{-1}. Radiance is collected by an Au-coated parabolic 90° off-axis mirror and reflected to the spectrometer entrance port.

Measurements of a calibration body are taken at 2 different temperatures to derive the instrumental response function (Ruff et al. 1997). The artifact called Christiansen feature (CF) (emissivity going to unity at a certain point in the spectrum) is used for the calibration procedure and to determine the temperature of the sample at the emitting skin. In this work, the prepared cups can be contemporary mounted in the carousel and then heated one at a time. For each sample, the first emissivity measure were carried out at 343 K. The high-T emissivity measurements were carried out at different steps of temperature (e.g., 400-500-600-700K), reaching the maximum temperature variation achievable by the PEL set-up within the range suggested for the surface of Mercury (Vasavada et al. 1999; Bauch et al. 2011).

After the heat-treatment, the samples appeared reworked, showing new distribution and color of grains. Basically, the Earth atmosphere humidity of the samples plays a special rule during the entire measure, delaying the air leakage and furthering oxidations or even worse structural variations. To check the actual occurred variations, olivine sample grain-size range 0-45 µm - the most seemingly reworked – was measured and re-characterized by X-Ray Diffractions. The single crystal XRD results have explained that no changes occurred at cell parameters - in particular no increasing occurred - hence surly there is no substitution of Fe^{3+} cations instead of Fe^{2+} cations. Powder XRD has explained the reddening of the grains as a coat of hematite (less than 1% in volume percentage). Since the reddening is confined to the bottom cup and the acquired spectra is relating to the upper 20 µm of the sample, the presence of hematite coat doesn't tamper with the main mineral phase on the resulting spectra features.

Concerning the schedule of the PEL measurements, a *pre-measure sample treatment* was scheduled in order to prepare samples devoid of humidity, mainly acting on the *vacuum condition timing* (especially acting on the air suction time to discharge more pressure from the intra-granular volumes), and on the *cup selection and preparation* (on the heating of the cups in order to reduce the thermal gradient between the bottom/rims and the surface or the sample). A summary of the protocol has been explained following.

The measures have been carried out at two different steps of temperature relative to a current intensity of 3 A and 6 A. Samples have been preheated in an oven at 50 °C for 24 h, removing the atmosphere humidity, and then placed into a drier chamber. The samples have been heated not over 50°C since higher temperatures could spark off a surface oxidation of the grains. Samples were placed into the heating chamber, which slowly led the best vacuum condition maintaining 0.8 mbar for one hour before to start heating. The first measure was obtained after 70 minutes at 3A, and the second after further 70 minutes at 6 A. Then the current has been shut-off and the sample got cold under vacuum condition for another hour, in order to avoid any possible oxidation during the cooling. Finally the samples were replaced into the drier chamber after 16 hours. In order to confirm a correct sample set-up, we replied on each particulate the XRD diffractions and compared the pre-PEL results with the post-PEL results.

Phase characterization: the phase will be well characterized at room conditions by single crystal X-ray diffraction (if necessary also by X-ray powder diffraction) and analyzed by electron microprobe (WDS method);

Cup selection and preparation: the produced size fractions will be placed into steel cups - which could be selected among different heights - without any pressure and constraint; *pre-measure sample treatment*: the cups could be heated in oven at a standard temperature for several hours, in order to reduce the amount of water in the particulate;

Cup placement and vacuum condition timing: each cup will be placed into the chamber, which will be evacuated in a given time; *current steps selection (I→T)*: the cup will be heated increasing the current, or it will be cooled decreasing the current; the measures will be instantaneous, referred to the free surface of the cup and carried out at different steps of heating or cooling.

3.2.3 Physical characters and temperature gradients

Effects due to the physical characters. The selected range of particle size and porosity of particulate mineral samples can affect the observed emissivity spectral features more than other physical characters - the emissivity spectra, indeed, are the result of both the absorption coefficient and the refractive index. This effect depends on the dominant scattering, which is just due to the dimensional relationship between the grain-size and the incident wave. Thus, coarse particulates are dominated by surface scattering and lead to strong reststrahlen bands in the emissivity spectra. Whereas fine particulate (<65 μm) materials are dominated by surface scattering – waves are refracted into particle interiors and then scattered or refracted back out – and lead to a reduced contrast in the reststrahlen bands accompanied by the appearance of additional features (Maturilli et al. 2008). About remote sensing, understanding this effect is important to distinguishing features due to scattering effects from those due to composition.

Effects due to the temperature. The effects of temperature *in situ* (sample measured at high-temperature) on the sample spectra cannot be easily described as no data in literature are reported to date, with the exception of one single datum obtained on a labradoritic plagioclase by Herbert and Maturilli (2009). An indication of what we could expect during our experiments can be retrieved by data of volume thermal expansion on minerals. We well know that minerals show a significant thermal expansion when they are under high-temperature conditions: such expansion strongly affects the vibrational modes at local scale and therefore can influence the TIR spectra of minerals within certain wavelengths (e.g. 2-15 μm). What we could expect from our measurements is a variable shift in the spectra peaks as a function of temperature. It is likely that such shift will be characteristic of every single mineral and then the measurements on different phases are necessary.

Effects due to the temperature gradient. Based on the effects that we could expect at point 2) it is clear that temperature gradients within the sample would give complex spectra as a result of different peak shift within the same sample (e.g. volume of the sample at zero K will be characterized by peak positions different with respect to those relative to volume of the same sample at 700K).

Figure 3.1. Sample preparation and vacuum chamber at PEL. a) Crystals of pyroxenes labeled DiMDCV. b) Grinding of crystals. c) Cups of samples in dryer chamber. d) Within the vacuum chamber, the cups are placed on a carousel.

3.3 Results and conclusions

Results and conclusions of chapter 3 are presented in a manuscripts in submission - entitle *"In-situ high-temperature emissivity spectra and thermal expansion of C2/c pyroxenes: the independency on the Mg/Fe ratio"* (par. 3.3.1). The manuscript reported the strong relationship between thermal expansions of minerals (induced by the highest daily variations of temperature occurred on the surface of Mercury) and *in situ* spectra collected in laboratory for *C*2/*c* pyroxenes. This study has been conducted with the essential collaboration of Fabrizio Nestola[1], Matteo Massironi[1,2], Alessandro Maturilli[3], Jörn Helbert[3], Matteo Alvaro[4], Maria Chiara Domeneghetti[4], Federico Zorzi[1].

Concerning this work, we thank Dr. Alessandro Guastoni of the Museum of Mineralogy of the University of Padua for providing the sample DiMDCV, and Raul Carampin of CNRPadova for WDS electron microprobe facilities. The research was supported by Seventh Framework Programme/EuroPlanet Research Infrastructure (EC Grant Agreement n° 228319), by Progetto di Ateneo 2011 of the University of Padua and by Italian Space Agency grant (n. I/060/10/0) for the MARS-XRD/ExoMars project.

[1]Department of Geosciences, University of Padua, Padova, Italy
[2]Astronomical Observatory of Padua, INAF, Padova, Italy
[3]Institute for Planetary Research, DLR, Berlin-Adlershof, Germany
[4]Department of Earth Sciences and Environment, University of Pavia, Pavia, Italy

3.3.1 In-situ high-temperature emissivity spectra and thermal expansion of *C*2/*c* pyroxenes: the independency on the Mg/Fe ratio

Abstract

Two *C*2/*c* augitic pyroxenes, with different Mg/Fe ratio, were investigated by in situ high-temperature thermal infrared spectroscopy and in situ high-temperature single-crystal X-ray diffraction up to about 750 and 770 K, respectively.

The emissivity spectra of the two samples show a significant band shift toward lower wavenumbers with increasing the temperature. The amount of band shifts appears to be surprisingly independent on the difference in Mg# number for these two samples (i.e. Mg# = 92 and 16). The analysis of the thermal expansion behavior for the two samples could help in explaining the above mentioned band shift similarity as the thermal expansion volume coefficient, α_V, is identical for the Mg-rich and Fe-rich samples, with α_V = 2.72(8) and 2.72(7)×10^{-5} K^{-1}, respectively, using the Berman (1988) equation.

Our results, even in case of the best spectral resolution performance from the Mercury Radiometer and Thermal Infrared Spectrometer (MERTIS) on board of BepiColombo mission, indicate that it is impossible to distinguish the difference in iron content for *C*2/*c* augitic pyroxenes.

Introduction

Ca-rich pyroxenes (clinopyroxenes, cpx) are among the most abundant silicate minerals of the Earth's crust and upper mantle (Stacher and Harris 2008). This has suggested to investigate their existence as a main constituent of other planetary body's shells, thus terrestrial, lunar and meteoritic clinopyroxenes have been largely investigated under different conditions of temperature and pressure (e.g. Tribaudino et al. 2002, Nestola et al. 2008 and reference therein), assuming a broader role for planetary geology. In a remote sense, past and on-going space missions and ground-based telescopes have collected spectra of different nature, in order to investigate the mineralogical composition of planetary body surface. Concerning Mercury, several ground-based observations pointed out that Ca-rich (and low-Fe) clinopyroxenes could be common constituent minerals of its surface, with diopside and augite considered as good possible candidates (i.e. Sprague et al. 2002; Sprague et al. 2007; Sprague et al. 2009). The overall knowledge of this planet has been further improved by the interpretation of a wide range of spectra (e.g. Visible and Near Infra-Red spectra, X-ray spectra and Gamma-ray spectra) provided by the on-going Mercury Surface Space ENvironment GEochemistry and Ranging (MESSENGER) NASA mission (Solomon et al. 2001). In particular, for the dominantly terrain of the surface of Mercury Warell et al. (2010) indicate that the Mg-rich clinopyroxenes could reach the 30% of (Hapke-modeled) mineral modal abundance. The next European Space Agency and Japan Aerospace Agency mission to Mercury, named BepiColombo, will carry on board the Mercury Radiometer and Thermal Infrared Spectrometer (MERTIS) (Hiesinger and Helbert 2010) that will be able to provide Thermal Infra-Red (TIR) emissivity spectra from 7 to 14 μm. This range of wavelength is very effectively to identify the fine-scale

structural properties of silicates (e.g. stretching and bending motions in the silicon-oxygen anions, metal–oxygen and lattice vibrations). In addition, for mineral families as pyroxenes, the emissivity peak positions (bands) are a good indicator of the composition (see Hamilton 2000 and reference therein). Previous interpretations of the spectra of Mercury have not considered the possible effects induced by the extreme daily surface temperature range on the surface minerals. Indeed, the temperature of the surface of Mercury can range in 44 earth-days between 70 and 725 K, depending on latitudes and longitudes (Strom and Sprague 2003). Known thermal models (Vasavada et al. 1999; Bauch et al. 2011) show that a point on the equatorial surface is subjected to a temperature variation greater than 400 K between sunrise days and the midday. These temperature variations significantly affect the crystal structure and density of minerals and, at the same time, they should affect the TIR spectral signature of each single mineral present on the surface of the planet. This behavior has been recently demonstrated for plagioclases and olivines, which show significant TIR spectral signature changes under the typical temperature variation of the surface of Mercury (Helbert and Maturilli 2009; Helbert et al. submitted), and could be even predicted for other candidates. To our knowledge, emissivity measures of Ca-rich pyroxenes within the TIR range have been always conducted at room conditions (Christensen et al. 2000; Hamilton et al. 2000 and reference therein) except one sample measured by Maturilli et al. (2008). In this work we have measured the thermal expansion and the TIR emissivity spectra at high temperature in situ of two Ca-rich clinopyroxenes with a strong different Fe content, in order to provide possible spectral signature changes within a typical temperature range of the surface of Mercury. Considering that MERTIS will collect TIR emissivity spectra likely from a clinopyroxene-bearing regolith, our work could improve the interpretation of the returned data.

Methodology

Samples characterization

Well-preserved natural crystals of diopside were selected from the Montefiascone Volcanic Complex (Di Battistini et al. 1998). In detail, the samples analysed were provided by the Museum of Mineralogy of the University of Padua (Omboni mineral collection) and labeled as DiMDCV. Crystals of hedenbergite, coming from the Elba Island (Tuscany region, Italy) and belonging to a private collection, were labeled HeE0125. Both phases were fully characterized at room conditions at the Department of Geosciences of the University of Padua by the following techniques:

(i) Both minerals were analyzed by Wavelength-Dispersive System (WDS) method. The analyses were carried out at the Geosciences Department of the University of Padova, using a CAMECA CAMEBAX SX50 electron microprobe, with a fine-focused beam (~1µm diameter), an acceleration voltage of 20 kV and a beam current of 20 nA, with 10 seconds counting times for both peak and total background. X-ray counts were converted to oxide wt% using the PAP correction program supplied by CAMECA (Pouchou and Pichoir 1991). Standards, spectral lines and analytical crystals used were albite (Amalia plagioclase, TAP, Ka) for Na, MgO (TAP, Ka) for Mg, Al_2O_3 (TAP, Ka) for Al, diopside (TAP, Ka) for Si and (PET, Ka) for Ca, $MnTiO_3$ (LIF 220, Ka) for Mn

and (PET, Ka) for Ti, Cr_2O_3 (LIF 220, Ka) for Cr and Fe_2O_3 (LIF 220, Ka). Analysis results are reported in Table 3.1.

(ii) X-ray powder diffraction was performed in order to identify possible minor phases present in the selected natural samples. Data were recorded on a Panalytical θ-θ diffractometer (Cu radiation) equipped with a long fine focus Cu X-ray tube operating at 40kV and 40mA and a real-time multiple strip (RTMS) detector (X'Celerator). The scan was performed over the range 3-80° 2θ with a step size of 0.017° 2θ and a counting time of 150 s/step. The program High Score Plus (PANalytical) was used for phase identification, quantitative phase analysis with Rietveld refinement (Rietveld 1967) and cell parameters determination with Le Bail method (Le Bail et al. 1988). A pseudo-Voigt function was employed for the profile shapes. Refined parameters were scale factors, zero-shift, background, lattice constants, and profile parameters (Gaussian and Lorentzian coefficients). Diffractograms are reported in Figure 1.

(iii) Single-crystal X-ray diffraction was performed on both samples by a STOE STADI IV 4-circle diffractometer equipped with Mo source (conditions: 50 kV, 40 mA) and an Agilent CCD in order to obtain a reliable cation distribution combining the X-ray data with the EMPA ones. The single crystals used for this analysis were twin- and inclusion free and had a sharp optical extinction. Their size ranged from 120 × 120 × 100 μm^3 (DiMDCV) to 450 × 200 × 100 μm^3 (HeE0125). Weighted structural refinements based on Fo^2 were performed using the SHELX-97 package (Sheldrick 1997) in the *C*2/*c* space group starting from the coordinates of Finger and Ohashi (1976). The atomic scattering factors were taken from the International Tables for X-Ray Crystallography (Wilson 1995). Neutral vs. ionized scattering curves were refined for the oxygen (O and O^{-2}) and silicon (Si and Si^{2+} atoms). Fully ionized scattering factors were used for Al^{3+}, Ti^{4+}, Cr^{3+}, Mg^{2+}, Fe^{2+}, Fe^{3+}, Mn^{2+}, Ca^{2+}, Na^{+}. Anisotropic thermal parameters were obtained for all atoms of the two samples. For crystal DiMDCV a residual electron-density maximum, located at 0.67 Å from the M2 site, was observed in the difference-Fourier map; the same maximum was not found in the HeE0125 sample. The maximum found in DiMDCV sample is known for Ca-rich *C*2/*c* pyroxenes and has been observed in previous studies (Rossi et al. 1987; Oberti and Caporuscio 1991; Boffa Ballaran et al. 1998) and attributed to the possible presence of Mg and Fe^{2+} at the M2 site, giving rise to the so called "M2' split position". Therefore, a further set of refinements were performed using Mg^{2+} and Fe^{2+} scattering factors for the isotropic M2' site. The analytical results are reported in Table 2.

High-temperature in situ single-crystal X-ray diffraction

The same two fragments analyzed by single-crystal X-ray diffraction at room conditions were used for the in situ high-temperature measurements. The high-temperature experiments were performed at the Dipartimento di Scienze della Terra e dell'Ambiente (Università di Pavia, Italy). Each crystal was loaded in a 0.5 mm inner diameter quartz vial 26 mm long closed at the top by using oxy-methane flame. In order to avoid any possible Fe oxidation during the annealing an iron wire was loaded as buffer in the vial together with the crystal. A small amount of quartz wool was used in order to avoid any mechanical stress, and any contact between the iron wire and the crystal. After alternately washing with Ar flux and vacuuming, the vial was sealed at the

open end (bottom) by using oxy-methane flame. The vial was then mounted into a short metal goniometer head on a Philips PW1100 diffractometer operated with FEBO software (a locally developed control software) working with MoKa radiation at 55 kV and 30 mA and using a 0.5 mm short collimator. A microfurnace consisting of a H-shaped Pt–Rh resistance and a Pt:Pt-Rh thermocouple inside a steel cylindrical cage 1 inch wide closed with a Kapton film, calibrated as in Cámara et al. (2012), was mounted on the diffractometer. The device allows the collection of diffraction data up to θ_{max} = 33°. The UB matrix was determined by peak search and indexing of the 24 most intense reflections. The UB matrix and unit cell parameters were firstly refined by measuring the Bragg angles of the selected 24 most intense reflections, using horizontal and vertical slits. Afterward, the Philips LAT procedure was used to obtain accurate and precise lattice constants and the UB matrix. The LAT procedure allowed the position of different reflections (with different nd-values), at positive and negative ω-2θ, to be measured. The reflection is firstly centred by using the vertical and horizontal slits, then a scan in ω-2θ is performed and the observed maxima are calculated. The observed nd-values were fit producing a relative d-value and its e.s.d.'s. The procedure was repeated on both crystals for each temperature step on a group of 60 selected reflections, and lattice parameters were calculated by least-squares fitting of all the observed d-values and are reported in Table 4.

Samples preparation for Thermal Infra-Red (TIR) emissivity measures

Regarding the particulate mineral samples, the selected range of particle size and porosity can affect the observed emissivity spectral features, which are the result of both the absorption coefficient and the refractive index. This influence depends on the dominant scattering, which is just due to the dimensional relationship between the grain-size and the incident wave. Thus, coarse particulates are dominated by surface scattering and lead to strong characteristic bands in the emissivity spectra, named reststrahlen bands. Whereas fine particulate (< 65 μm) materials are dominated by volume scattering – waves are refracted into particle interiors and then scattered or refracted back out – and lead to a reduced contrast in the reststrahlen bands accompanied by the appearance of additional features (Maturilli et al. 2008). Concerning remote sensing applications, understanding this effect is important to distinguishing features due to scattering effects from those due to the composition.

Emery et al. (1998) defined the size of the fine loose rocks (regolith) that constitute the surface of Mercury most likely between 30 μm and 100 μm. In order to avoid possible spectral features of volume scattering, DiMDCV and HeE0125 samples have been reduced in a jaw crusher between 90 μm and 125 μm, or toward the largest end-member (i.e. 100 μm) suggested by Emery et al. (1998). The selected particle range (90-125 μm) are likely immune to thermal gradient effects in the TIR range, which on the contrary should be remarkable in the finest particles of the surface of Mercury proposed in the literature. Therefore, this range allowed us to work very close to the presumable size of Mercurian regolith avoiding possible alterations of the TIR spectra besides those due to the mineral thermal expansion. The produced particulates have been placed into specific stainless steel cups, with a 3 cm internal diameter (Fig. 3.2) and 5 cm depth, and

then heated in oven at 325 K for almost 12 hours, in order to minimize the presence of intra-grains water. The cups were at last placed in a dryer chamber.

High-temperature in situ Thermal Infra-Red (TIR) emissivity spectroscopy

This kind of analysis is possible by means of vibrational spectroscopy, whose basic principle is that vibrational motions occur in a crystal lattice at particular frequencies, strictly associated to the crystal structure and elemental composition (Farmer 1974; Christensen et al. 2000). The spectral measurements have been performed at the Planetary Emissivity Laboratory (Institute of Planetary Research, Deutsches Zentrum fuer Luft- und Raumfahrt, Berlin). The instrument used is a Bruker Vertex 80V, with a liquid nitrogen cooled HgCdTe detector and a KBr beamsplitter. The spectrometer is coupled to an evacuated planetary simulation chamber, having an automatic sample transport system (carousel) to maintaining the vacuum while changing the samples. The steel of the sample cups is heated via a copper induction pancake coil, ensuring that the surrounding remains cold into the chamber. The emissivity measurements can be carried out at different steps of temperature and in vacuum (under 1 mbar of pressure; Maturilli et al. 2008), acquiring spectra between 1 and 16 µm at a resolution of 4 cm^{-1}. Radiance is collected by an Au-coated parabolic 90° off-axis mirror and reflected to the spectrometer entrance port. Measurements of a calibration body are taken at 2 different temperatures to derive the instrumental response function (Ruff et al. 1997). The artifact called Christiansen feature (CF) (emissivity going to unity at a certain point in the spectrum) is used for the calibration procedure and to determine the temperature of the sample at the emitting skin. In this work, the two prepared cups have been together mounted in the carousel and then heated one at a time. For each sample, the first emissivity measure has been carried out at 343 K, whereas the second at 723 K, in order to reach the maximum temperature variation achievable by the PEL set-up within the range suggested for the surface of Mercury (Vasavada et al. 1999; Bauch et al. 2011). The acquired emissivity spectra are showed in Figure 3.

Results and discussion

Chemical composition and single-crystal X-ray diffraction

The chemical compositions of our two samples were determined by EMPA analyses as described in the experimental section. The relative chemical formulas based on six oxygen atoms are the following:
sample DiMDCV: $Ca_{0.94}Na_{0.01}Fe^{tot}_{0.08}Mg_{0.95}Cr_{0.01}Ti_{0.01}Si_{1.92}Al_{0.08}O_6$
sample HeE0125: $Ca_{0.99}Na_{0.01}Mn_{0.02}Fe^{tot}_{0.82}Mg_{0.16}Si_{1.98}Al_{0.02}O_6$

The main difference between the two samples is related to the Mg-Fe substitution with an Mg# = 0.92 for DiMDCV and 0.16 for HeE0125.

Based on the same approach used in several previous works dedicated to the best refinement protocol for clinopyroxenes (e.g. Domeneghetti et al. 2005 and references therein, Nestola et al. 2007) we combined the EMPA results and the crystal structure

refinement ones to obtain a reliable cation distribution for both the samples here investigated. Based on such approach we obtained the following cation distribution:

DiMDCV: $^{[M2+M2']}(Ca_{0.95}Mg_{0.05})^{[M1]}(Mg_{0.91}Fe^{2+}_{0.08}Cr_{0.01})^{[T]}(Si_{1.95}Al_{0.05})O_6$

HeE0125: $^{[M2+M2']}(Ca_{0.98}Na_{0.02})^{[M1]}(Fe^{2+}_{0.76}Mg_{0.16}Fe^{3+}_{0.05}Cr_{0.01}Mn_{0.02})^{[T]}(Si_{1.95}Al_{0.05})O_6$

The charge balance for both the formulae is good: the sample DIMDCV showing 11.96 positive charges and the sample HeE0125 having 11.99 positive charges.

Based on Shannon (1976), the average cation radius of the M2-M2' sites are 1.10Å and 1.12Å for DiMDCV and HeE0125, respectively, with a limited difference of about 1.8%. The tetrahedral sites, instead, for both samples are identical in terms of chemistry and thus cation radius. As a consequence, the only difference affecting the structure of these two clinopyroxenes is relative to the M1site where the strong Mg/Fe cation substitution occurs. In detail, the average cation radius of M1 site for DiMDCV sample is 0.72 Å whereas it is 0.76 for the HeE0125 sample (i.e. a difference by about 5.3%). Such a difference is responsible for the strongly increased unit-cell volume at room conditions for HeE0125 sample, i.e. +2.8% (Table 4) as long as for the increase by about 2.1% of the <M1-O> distance for this sample. On the contrary the <M2-O> distances between the two samples only show a difference by about 0.7% (no differences are evident for the tetrahedral sites for the two samples investigated).

Thermal expansion behavior

Several studies have been dedicated to the high-temperature behavior of C2/c clinopyroxenes belonging to the pyroxene quadrilateral ($CaMgSi_2O_6$ - $CaFeSi_2O_6$ - $Mg_2Si_2O_6$ - $Fe_2Si_2O_6$) during the last forty years. However, most of such studies were mainly focused on the end-member compositions, i.e. diopside and hedenbergite (Cameron et al. 1973), diopside (Finger and Ohashi 1976), hedenbergite (Tribaudino et al. 2008). Despite augite compositions $(Ca,Mg,Fe)(Mg,Fe)Si_2O_6$ are actually among the most common rock forming pyroxenes, only one intermediate composition *C*2/*c* pyroxene has been investigated at high temperature, a synthetic $Ca_{0.8}Mg_{1.2}Si_2O_6$ (Benna et al. 1990).

In this work we measured at 14 different temperatures and up to 773 K the evolution of the unit-cell volumes of the two intermediate (augitic) pyroxene composition DiMDCV and HeE0125 samples. Unit-cell volume as a function of temperature for both the samples is shown in Figure 4. The two T-V curves appear to show similar trends. The increase in volume up to 773 K is 1.38% and 1.37% for DiMDCV and HeE0125, respectively, with a negligible difference.

In Table 5 the volume thermal expansion coefficients were reported for the two samples investigated in this work compared with other clinopyroxenes compositions. The data in Table were obtained by using the second order polynomial thermal expansion equation proposed by Berman 1988 (equation 1):

$$(1)\ V(T) = V_0\ [1 + a_0(T - T_r) + a_1(T - T_r)^2]$$

From which (2) $\partial V/\partial T = \alpha_{V,T} = a_0 + 2a_1(T - T_r)$. The equation (2) applied to our dataset provides the best fitting with a consistent agreement between observed and calculated unit cell volumes (δV) much smaller than 0.1 $Å^3$ for all the temperature steps from room *T* to the maximum temperature reached in this work (773 K). For purpose of comparison, the literature data reported in Table 5 were re-fit using the same Berman (1988) equation: the thermal expansion coefficients are reported in the same table.

To be remarked, previous works (i.e. Cameron et al. 1973) reported the thermal expansion coefficients for several *C*2/*c* pyroxenes, including the two end-members diopside and hedenbergite, performing linear least-square fittings of the unit cell volume by using the following equation:

$$(3)\ \alpha_x\ (K^{-1}) = 1/X_{24} \times (X_T - X_{24}) / (T - 298)$$

Equation (3) represents what they called "mean thermal expansion coefficient", where the terms X_{298} and X_T are the values of a single parameter at 298 K (room temperature) and at some higher temperature *T*, respectively. The quantity α_x represents a percentage increase per degree (actually percent × 10^{-2}/degrees) over the temperature range studied, and algebraically it is equivalent to the rate of increase with temperature divided by the room temperature value of the parameter. Their mean thermal expansion coefficients calculated as described above are 2.98 × 10^{-5} and 3.33 × 10^{-5} K^{-1} for diopside and hedenbergite, respectively. More recently, Tribaudino et al. (2008) reported the thermal expansion coefficient α for a synthetic pure hedenbergite sample. In this work the thermal expansion coefficient has been determined by fitting the experimental values of the unit-cell volume at the different temperatures using the following equation:

$$(4)\ \ln (V/V_0) = \alpha (T - T_0)$$

Equation (4) assumes that the thermal expansion coefficient α is independent from *T*. The resulting volume thermal expansion coefficient α_V = 2.92(7) × 10^{-5} K^{-1} is therefore very close to that of a linear approximation. However, Camara et al. (2012) clearly demonstrated that higher order polynomial equations would be more reliable for almost linear thermal expansion behavior. Thus for our two samples we did not consider linear approximations.

Using the data of thermal expansion in Table 5 it is possible to note a strong scatter in terms of Mg# number versus the relative volume thermal expansion coefficient (Figure 5). Without entering in the details of the reasons why such scatter is present, we will be not able to carry on any extrapolation of α_V as a function of composition.

Applying our high-temperature results to the environment present on the surface of Mercury, we could assume that possible augitic pyroxenes may undergo a temperature variation of 400 K over a time of 44 Earth-days. Using the equation (1) for our samples we can calculate a volume variation of 5.11 $Å^3$ for both DiMDCV and HeE0125 samples. If we focus on the Mg-rich sample (the most probable composition present on the surface of Mercury) we can observe that an increase in unit-cell volume by 5.11 $Å^3$ could be obtained by an increase of 400 K or by a decrease in the Mg# number of 20 (i.e. from 92 to 72 in case of the DiMDCV sample). This interpolation has been obtained considering the unit-cell volume of two end-members diopside and hedenbergite of Finger and Ohashi (1976) and Tribaudino et al. (2008) respectively, which are reported

in Table 5. Concerning TIR data acquired from satellites, this means that neglecting the effect of the temperature on the surface we could make significant mistakes in terms of composition. In fact, the available data of TIR spectra on clinopyroxenes are only referred to *room* temperature conditions (e.g. Christensen et al. 2000).

High-temperature thermal emissivity

In Figure 3, the main bands of *C*2/*c* clinopyroxenes belonging to the pyroxene quadrilateral between 1000 and 850 cm^{-1} are shown for the two samples studied in this work. Bands 1, 2 and 3 are the most intense in this spectral range and their exact position is a strong function of the iron abundance (Hamilton 2000). In detail, in Figure 3 we shown the spectra collected at 368 K (solid line) and 748 K (dashed line). For both the Mg-rich and Fe-rich samples we detected a shift of the bands, which can be expected as a function of the thermal expansion data discussed in the previous section. A detailed analysis of the peak positions is shown in Figure 6 where the band 1 position shifted toward higher wavenumbers. The shift corresponds to 14 cm^{-1} for DiMDCV sample and 17 cm^{-1} for HeE0125 sample as the temperature increases by 380 K. Band 2 and band 3 show more limited shifts but still we observe 10 cm^{-1} for band 2 and 4 cm^{-1} for band 3 of DiMDCV sample, and 8 cm^{-1} for band 2 and 2 cm^{-1} for band 3 of HeE0125 sample.

The BepiColombo MERTIS spectrometer will have a spectral resolution ranging from 9 to 20 cm^{-1}. Such resolution will allow ascertaining at least two of the three band shifts detected in this work for each composition. However, in terms of interpretation, our high-temperature in situ TIR data show that a Mg-rich augite should be interpreted as a Fe-richer augite only for high temperature range basing on the third band.

Sample	DiMDCV	HeE0125
Oxide wt.%		
Na_2O	0.11	0.16
MgO	17.46	2.70
Al_2O_3	1.89	0.37
SiO_2	52.60	48.33
CaO	24.07	22.60
TiO_2	0.26	0.01
Cr_2O_3	0.31	0.01
MnO	0.07	0.70
FeO_{tot}	2.68	24.12
Total	99.45	99.00
Formula		
Ca	0.94	0.99
Na	0.01	0.01
Mn	-	0.02
Fe	0.08	0.92
Mg	0.95	0.16
Ti	0.01	-
Cr	0.01	-
Al	0.08	0.02
Si	1.92	1.98
Total	4.00	4.00

Table 3.1. Electron microprobe analysis (oxide wt. %) and formula in atoms per formula unit based on six oxygen atoms for the crystals studied in this work.

Unit-cell par	DiMDCV	HeE0125
a	9.7443(1)	9.8268(2)
b	8.9147(1)	9.0045(1)
c	5.2591(1)	5.2527(1)
β	106.004(10)	105.023(1)
Vol.	439.135	448.899
Shift corr.	0.007	-0-01

Table 3.2. Unit cell parameters determined by X-ray powder diffraction using the Le Bail method (Le Bail et al. 1988) for the crystals studied in this work.

Crystal data	**DiMDCV**	**HeE0125**
Crystal system	Monoclinic	Monoclinic
Unit-cell parameters		
a	9.751(2) Å	9.838(1) Å
b	8.905(2) Å	9.009(1) Å
c	5.264(1) Å	5.2585(6) Å
β	106.08(2)°	105.00(1)°
Unit-cell volume	439.18 $Å^3$	450.15 $Å^3$
Space group	*C2/c*	*C2/c*
Z	4	4
Data collection		
Instrumentation	Four-circle STOE-STADI IV	
Temperature (K)	298(1)	
Radiation, wavelength (Å)	$Mo_{K\alpha}$, 0.71073	
$2\theta_{max}$ (º)	85.90	85.96
h, *k*, *l* ranges	-8 +18, -13 +15, -8 +8	-14 +15, -13 +16, -10 +2
Omega scan width (º), exposure time (s)	1, 20	1, 20
Unique reflections (R_{int})	1129 (0.030)	1136 (0.068)
Unique reflections $F > 4\sigma(F)$	710	722
Structure refinement		
Structure solution and Refinement software	SHELX	
Refinement method	Full-matrix least-squares on F^2	
Data/restraints/parameters	1129/17/83	1136/17/83
R_1 [$F > 4\sigma(F)$]	0.0224	0.0508
R_1 all	0.0541	0.0778
Goodness-of-fit on F^2	1.062	0.999
Weighting scheme	$\exp(2.55 \times s^2)/\sigma^2(F_o^2)$ where $s = \sin(\theta)/\lambda$	$\exp(2.55 \times s^2)/\sigma^2(F_o^2)$ where $s = \sin(\theta)/\lambda$

$R_{int} = \sum | F_o^2 - F_o^2 (mean)| / \sum F_o^2$

$R_1 = \sum | | F_o| - | F_c| | / \sum | F_o|$

GooF = $\{\sum[w(F_o^2 - F_c^2)^2]/(n - p)\}^{1/2}$, where n = number of reflections, p = number of refined parameters

Table 3.3. Unit cell parameters and structural refinement details for the single crystals studied in this work.

	DiMDCV	**HeE0125**
Si-O2	1.590(1)	1.585(1)
Si-O1	1.609(1)	1.608(1)
Si-O3	1.668(1)	1.670(1)
Si-O3	1.688(1)	1.690(1)
<Si-O>	1.639	1.638
M1-O2	2.046(1) ×2	2.078(1) ×2
M1-O1	2.056(1)×2	2.123(1) ×2
M1-O1	2.124(1)×2	2.155 (1) ×2
<M1-O>	2.075	2.119
M2-O2	2.334(1) ×2	2.348(1) ×2
M2-O1	2.364(1) ×2	2.359(1) ×2
M2-O3	2.560(1) ×2	2.611(1) ×2
M2-O3	2.718(1) ×2	2.730(1) ×2
<M2-O3>	2.494	2.512

Table 3.4. Bond-lengths (Å) for the crystals studied in this work.

Temperature (K)	V (Å^3)	V (Å^3)
	DiMDCV	**HeE0125**
298	437.27(7)	449.74(8)
323	437.55(8)	450.05(6)
*323	437.58(8)	450.00(7)
373	438.22(7)	450.60(8)
423	438.92(8)	451.20(7)
473	439.40(7)	451.85(7)
*498	439.69(8)	452.32(8)
523	440.06(9)	452.61(8)
573	440.68(10)	453.23(9)
623	441.31(8)	453.84(9)
673	442.06(9)	454.58(8)
*698	442.47(9)	454.92(8)
723	442.77(8)	455.36(7)
773	443.39(9)	455.98(8)

Note: the uncertainty on the temperature is estimated to be 1 K. *Data measured during the cooling.

Table 3.5. Unit-cell volumes as a function of temperature for samples DiMDCV and HeE0125.

Sample	Unit-cell V (Å^3)	α_V ($\times 10^{-5}$)	a_1 ($\times 10^{-9}$)	References
DiMDCV	437.33(3)	2.72(8)	5.0(1.9)	This work
HeE0125	449.75(3)	2.72(7)	5.0(1.6)	This work
Diopside	438.78(37)	3.36(41)	-0.4(4)	Cameron et al. (1973)
Diopside	439.09(17)	2.77(2)	8.3(3)	Finger and Ohashi (1976)
Hedenbergite	450.69(23)	2.35(24)	5.1(2.3)	Cameron et al. (1973)
Hedenbergite	450.94(15)	3.3(2)	-4.8(2.6)	Tribaudino et al. (2008)

Table 3.6. Thermal expansion coefficients for different *C*2/*c* pyroxenes obtained using the Berman (1988) equation. See the text for α_V and a_1.

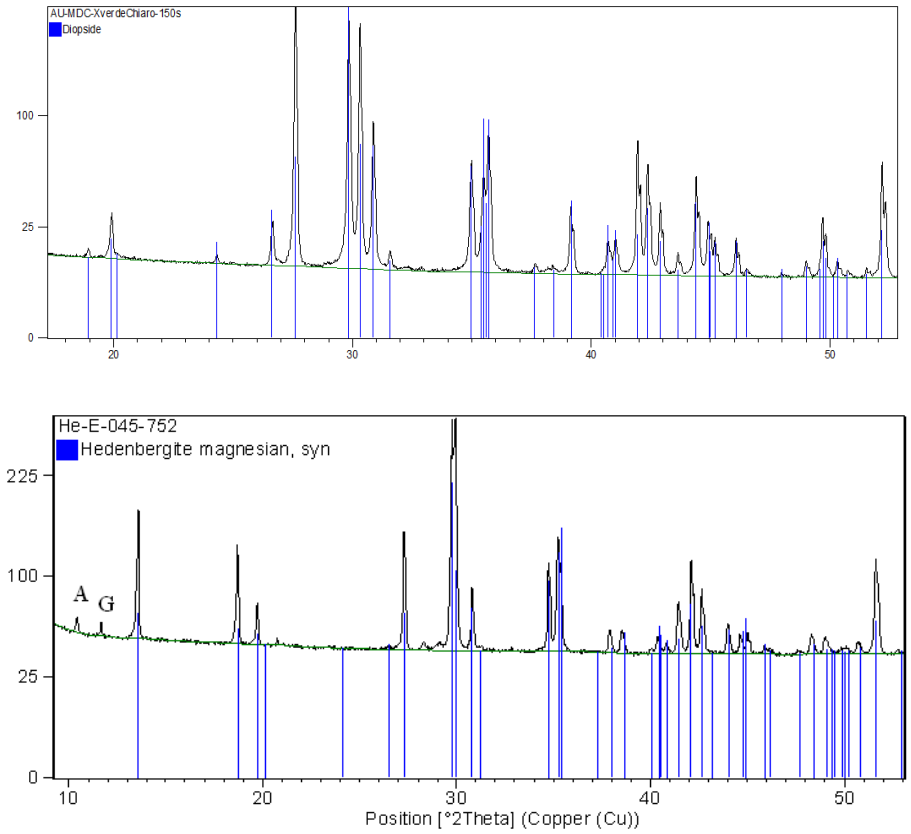

Figure 3.2. Powder X-ray diffraction of sample DiMDCV (top) and HeE0125 (bottom) samples. In blue the reference peaks of diopside (card 98-001-7094 of ICSD database), and hedenbergite magnesian (card 01-087-0702 of ICSD database).

Figure 3.3. Unheated samples of diopside (DiMDCV at 0-125 µm, left side) and hedenbergite (HeE0125 at 0-125 µm, right side) prepared for the TIR vacuum chamber (see the text).

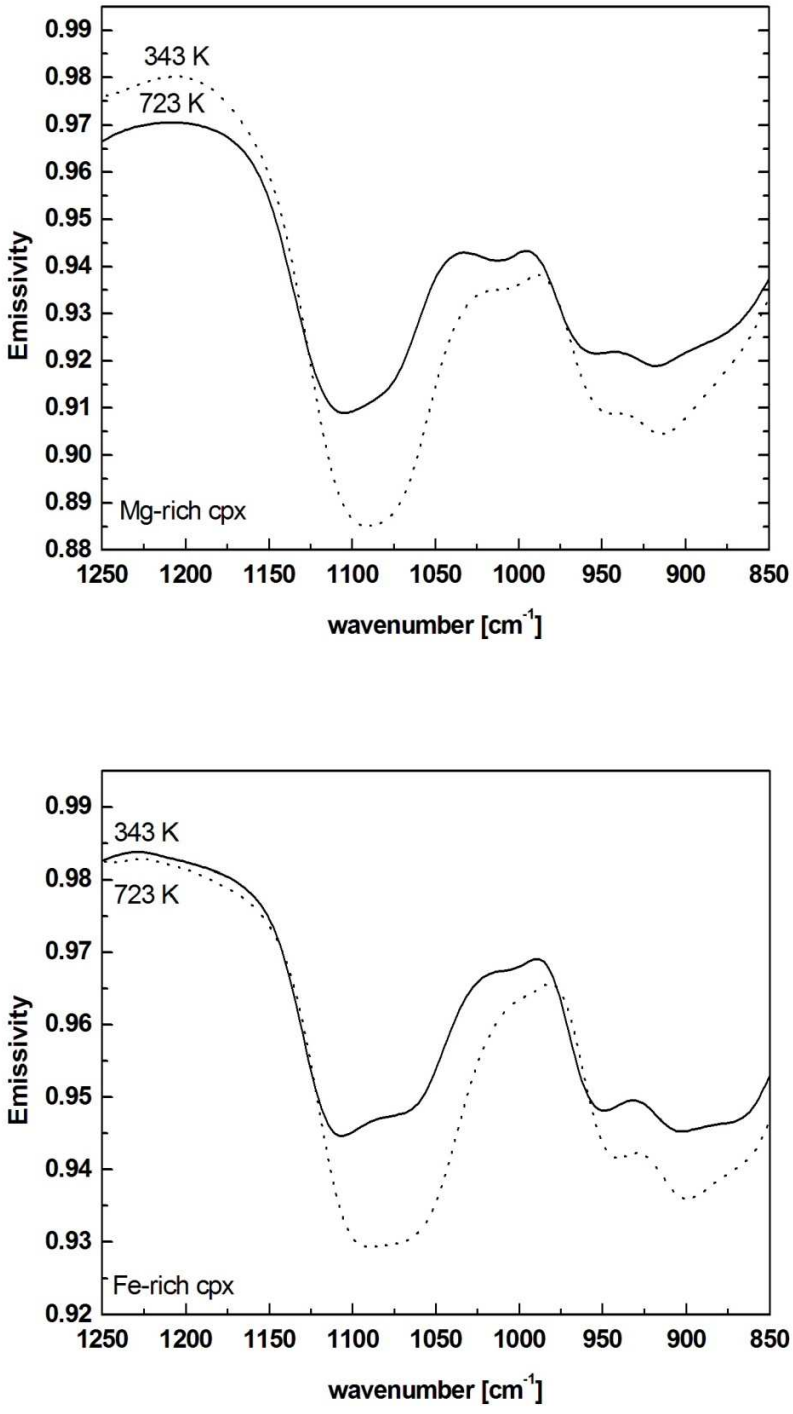

Figure 3.4. Emissivity spectra of a) diopside, sample DiMDCV at 0-125 µm and b) hedenbergite, sample HeE0125 at 0-125 µm, obtained at 345 K and 725 K.

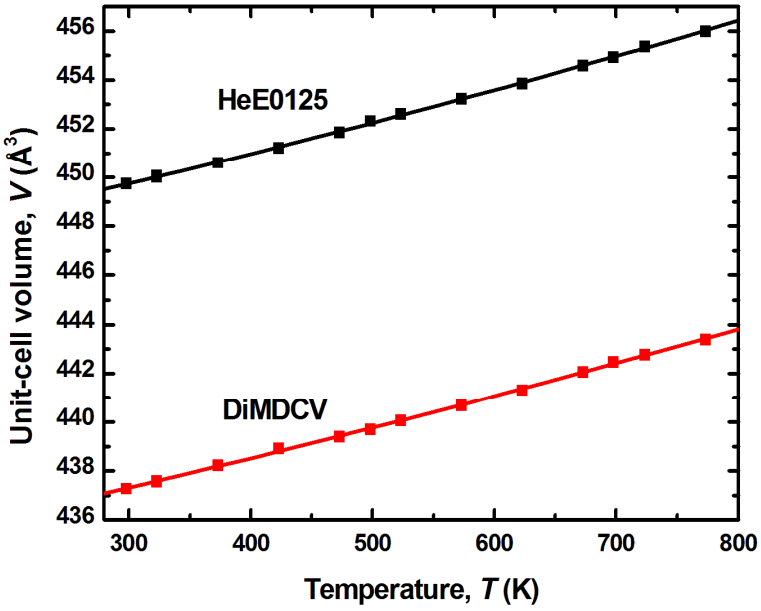

Figure 3.5. Unit-cell volume as a function of temperature ofor samples DiMDCV and HeE0125.

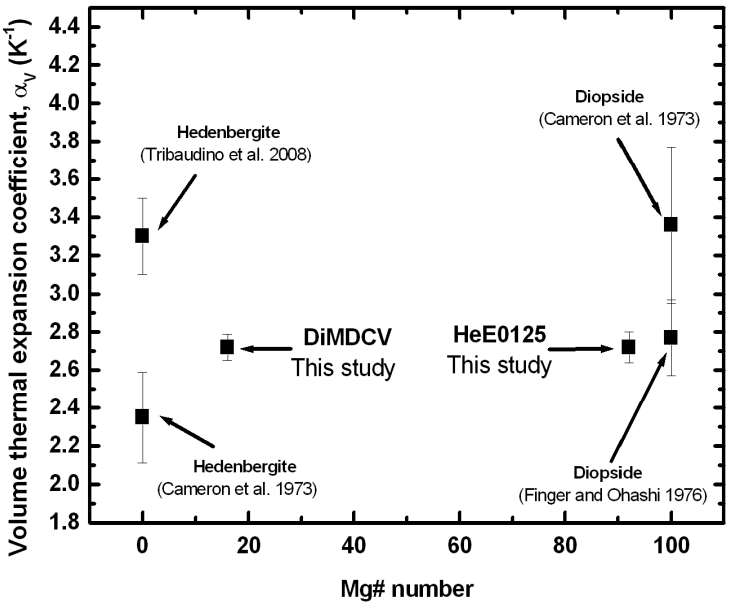

Figure 3.6. Volume thermal expansion coefficient as a function of Mg# number for different *C*2/*c* clinopyroxenes.

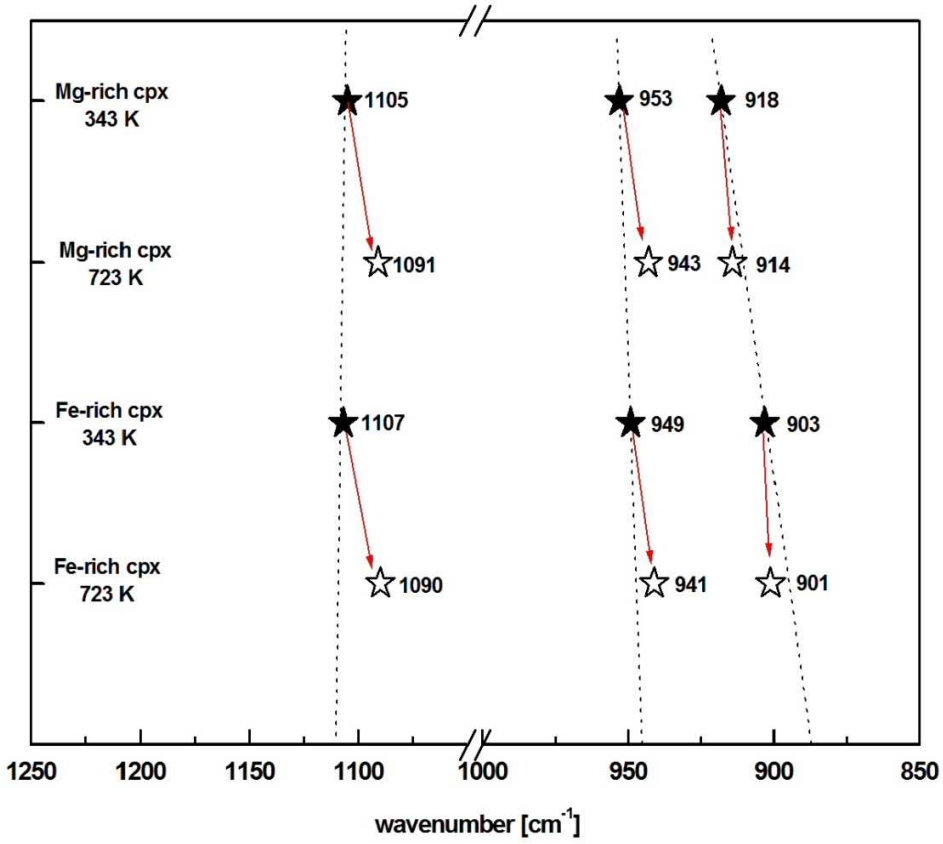

Figure 3.7. Band shift as a function of temperature for the DiMDCV (Mg-rich cpx in figure) and HeE0125 (Fe-rich cpx in figure) samples.

4 Conclusions

Each chapter ends with a punctual conclusion of the so different topics that we treated in this work. In a scientific point of view, this decade will benefit of the wide inheritance of MESSENGER mission on Mercury and several improvements on the knowledge of this planet and of the Solar System will be done. Next BepiColombo mission will have the possibility to clear all the unexpected inferences of MESSENGER as the extensive volcanism and the high-rate of sulfur and volatiles determined from the surface.

References

Bauch, K., Hiesinger, H., Helbert, J., 2011. Insolation and resulting surface temperatures of study regions on Mercury, 2257, 42rd Lunar Planet. Sci. C., The Woodlands, Texas.

Benkhoff, J., van Casteren, J., Hayakawa, H., Fujimoto, M., Laakso, H., Novara, M., Ferri, P., Middleton, H. R., Ziethe, R., 2010. BepiColombo - Comprehensive exploration of Mercury: mission overview and science goals, *Planet. Space Sci.*, 58, 2-20.

Benna, P., Tribaudino, M., Zanini, G. Bruno, E., 1990. The crystal structure of $Ca_{0.8}Mg_{1.2}Si_2O_6$ clinopyroxenes ($Di_{80}En_{20}$) at T=-130, 25, 400 and 700° C, *Z. Kristallogr.*, 192, 183-199.

Benz, W., Slattery, W. L., Cameron, A. G. W., 1988. Collisional stripping of Mercury's mantle, *Icarus*, 74, 516–528.

Berman, R. G., 1988. Internally-consistent thermodynamic data for minerals in the system Na_2O–K_2O-CaO-MgO-FeO-Fe_2O_3-Al_2O_3-SiO_2-TiO_2–H_2O-CO_2, *J. Petrol.*, 29, 445-522.

Blair, D. M., Freed, A. M., Byrne, P. K., Klimczak, C., Prockter, L. M., Ernst, C. M., Solomon, S. C., Melosh, H. J., Zuber, M. T., 2012. The origin of graben and ridges in Rachmaninoff, Raditladi, and Mozart basins, Mercury, *J. Geophys. Res.*, in press, 10.1029/2012JE004198.

Blewett, D. T., Hawke, B. R., Lucey, P. G., Robinson, M. S., 2007. A Mariner 10 color study of mercurian craters, *J. Geophys. Res.*, 112, E02005, 10.1029/2006JE002713.

Blewett, D. T., Robinson, M. S., Denevi, B. W., Gillis-Davis, J. J., Head, J. W., Solomon, S. C., McClintock, W. E., 2009. Multispectral images of Mercury from the first MESSENGER flyby: Analysis of global and regional color trends, *Earth Planet. Sci. Lett.*, 285, 272–282.

Boffa Ballaran, T., Carpenter, M., Domeneghetti, M. C., Tazzoli, V., 1998. Structural mechanisms of solid solution and cation ordering in augite-jadeite pyroxenes: I. A macroscopic perspective, *Am. Mineral.*, 83, 419-433.

Boynton, W. V., Sprague, A. L., Solomon, S. C., Starr, R. D., Evans, L. G., Feldman, W. C., Trombka, J. I., Rhodes, E. A., 2007. MESSENGER and the chemistry of Mercury's surface, *Space Sci. Rev.*, 131, 1-4, 85-104.

Brown, S. M., Elkins-Tanton, L. T., 2009. Compositions of Mercury's earliest crust from magma ocean models, *Earth Planet. Sci. Lett.*, 286, 446-455.

Bryan, W. B., 1973. Wrinkle-ridges as deformed surface crust on ponded mare lava, *Geochimic. Cosmochim. Acta,*, supp. 1, 93-106.

Byrne, P. K., Şengör, C., Klimczak, C., Solomon, S. C., Watters, T. R., 2012a. Large-scale crustal deformation on Mercury, 2118, 43rd Lunar Planet. Sci. C., The Woodlands, Texas.

Byrne, P. K., Watters, T. R., Murchie, S. R., Klimczak, C., Solomon, S. C., 2012b. A tectonic survey of the Caloris basin, Mercury, 1722, 43rd Lunar Planet. Sci. C., The Woodlands, Texas.

Byrne, P. K., Klimczak, C., Blair, D. M., Ferrari, S., Solomon, S.C., Freed, A. M., Watters, T. R., Murchie, S. L., 2013. Tectonic complexity within volcanically infilled craters and basins on Mercury, 44th Lunar Planet. Sci. C., The Woodlands, Texas, submitted.

Cámara, F., Gatta, G. D., Meven, M., Pasqual, D., 2012. Thermal expansion and high temperature structure evolution of zoisite by single-crystal x-ray and neutron diffraction, *Phys. Chem. Miner.*, 39, 1, 27-45.

Cameron, M., Sueno, S., Prewitt, C. T., Papike, J. J., 1973. High temperature crystal chemistry of acmite, diopside, hedenbergite, jadeite, spodumene, and ureyite, *Am. Mineral.*, 58, 594-618.

Cameron, M., Papike, J. J., 1981. Structural and chemical variations in pyroxenes, *Am. Mineral.*, 66, 1-50.

Chapman.....

Christensen, P. R., Bandfield, J. L., Hamilton, V. E., Howard, D. A., Lane, M. D., Piatek, J. L., Ruff, S. W., Stefanov, W. L., 2000. A thermal emission spectral library of rock-forming minerals, *J. Geophys. Res.*, 105, E4, 9735-9739.

Cintala, M., Grieve, R., 1998. Scaling impact melting and crater dimensions: Implications for the lunar cratering record, *Meteorit. Planet. Sci.*, 33, 889-912.

Crater Analysis Techniques Working Group, 1978. Standard techniques for presentation and analysis of crater size-frequency data, 1-24, *Tech. Memo*, NASA, Washington, D.C., 79730.

Denevi, B. W., Robinson, M. S., Solomon, S. C., Murchie, S. R., Blewett, D. T., Domingue, D. L., McCoy, T.J., Ernst, C. M., Head, J. W., Watters, T. R., Chabot, N. L., 2009. The evolution of Mercury's crust: a global perspective from MESSENGER, *Science*, 324, 613-618, 10.1126/science.1172226.

Dombard, A. J., Hauck, S. A., 2008. Despinning plus global contraction and the orientation of lobate scarps on Mercury: Predictions for MESSENGER, *Icarus*, 198, 1, 274–276.

Domeneghetti, M. C., Zema, M., Tazzoli, V., 2005. Kinetics of Fe^{2+}- Mg order-disorder in $P2_1/c$ pigeonite, *Am. Mineral.*, 90, 1816-1823.

Dzurisin, D., 1978. Tectonic and volcanic chronology of Mercury as inferred from studies of scarps, ridges, troughs, and other lineaments, *J. Geophys. Res.*, 83, 4883-4906.

Emery, J. P., Sprague, A. L., Witteborn, F. C., Colwell, J. E., Kozlowski, R. W. H., Wooden, D. H., 1998. Mercury: thermal modeling and mid-infrared (5-12 μm) observations, *Icarus*, 136, 104-123.

Farmer, V. C., 1974. *The infrared spectra of minerals*, monograph n.4, The Mineralogical Society, London.

Fassett, C. I., Head, J. W., Blewett, D. T., Chapman, C. R., Dickson, J. L., Murchie, S. R., Solomon, S. C., Watters, T. R., 2009. Caloris impact basin: Exterior geomorphology, stratigraphy, morphometry, radial sculpture, and smooth plains deposits, *Earth Planet. Sci. Lett.*, 285, 297-308.

Fassett, C. I., Head, J. W., Baker, D. M., H., Zuber, M. T., Smith, D. E., Neumann, G. A., Solomon, S. C., Klimczak, C., Strom, R. G., Chapman, C. R., Prockter M. L., Phillips, R. J., Oberst, J., Preusker, F., 2012. Large impact basins on Mercury: Global distribution, characteristics, and modification history from MESSENGER orbital data, *J. Geophys. Res.*, 117, E00L08, 10.1029/2012JE004154.

Fegley, B., Cameron, A. G. W., 1987. A vaporization model for iron/silicate fractionation in the Mercury protoplanet, *Earth Planet. Sci. Lett.*, 82, 207-222.

Ferrari, S., Massironi, M., Rothery, D. A., Cremonese, G., 2011. Beagle Rupes and Rembrandt scarp: A comparison on Mercury surface, EPSC-DPS2011-963-1, European Planetary Science Congress 2011.

Ferrari, S., Nestola, F., Maturilli, A., Massironi, M., Helbert, J., Redhammer, G. R., 2011, X-ray diffraction as a function of temperature for Fo_{92}-Fa_{8}: implications for the hermean surface, EPSC-DPS2011-1435, European Planetary Science Congress 2011.

Ferrari, S., Massironi, M., Klimczak, C., Byrne, P. K., Cremonese, G., Solomon, S. C., 2012. Complex history of the Rembrandt basin and scarp system, Mercury, EPSC-2012-874, European Planetary Science Congress 2012.

Finger, L. W., Ohashi, Y., 1976. The thermal expansion of diopside to 800°C and a refinement of the crystal structure at 700°C, *Am. Mineral.*, 61, 303-310.

Fleitout, L., Thomas, P. G., 1982. Far-field tectonics associated with a large impact basin: applications to Caloris on Mercury and Imbrium on the Moon, *Earth Planet. Sci. Lett.*, 58, 104-115.

Freed, A. M., Blair, D. M, Watters, T. R., Klimczak, C, Byrne P. K., Solomon, S. C., Zuber, M. T., Melosh, H. J., 2012. On the origin of graben and ridges within and near volcanically buried craters and basins in Mercury's northern plains, *J. Geophys. Res.*, 117, E00L06, 10.1029/2012JE004119.

Gillis-Davis, J. J., Blewett, D. T., Gaskell, R. W., Denevi, B. W., Robinson, M. S., Strom, R. G., Solomon, S. C., Sprague, A. L., 2009. Pit-floor craters on Mercury: Evidence of near-surface igneous activity, *Earth Planet. Sci. Lett.*, 285.

Gold, R. E. and 29 others, 2001.The MESSENGER Mission to Mercury: scientific payload, *Planet. Space Sci.*, 49, 1467-1479.

Golombek, M. P., Plescia, J. B., Franklin, B. J., 1991. Faulting and folding in the formation of planetary wrinkle ridges, *Proc. Lunar Planet. Sci. Conf.*, 21, 679–693.

Hamilton, V. E., 2000.Thermal infrared emission spectroscopy of the pyroxene mineral series., *J. Geophys. Res.*, 105, 9701–9716.

Hamilton, V. E., 2010. Thermal infrared (vibrational) spectroscopy of Mg-Fe olivines: A review and applications to determining the composition of planetary surfaces, *Chem. Erde*, 70, 7-33.

Harder, H., Schubert, G., 2001. Sulfur in Mercury's core?, *Icarus*, 151, 1, 118-122.

Hawkins, S. E., Boldt, J. D., Darlington, E. H., Espiritu, R., Gold, R. E., Grey, M. P., Hash, C. D., Hayes, J. R., Jaskulek, S. E., Kardian, C. J., Keller, M. R., Malaret, E. R., Murchie, S. R., Murphy, P. K., Peacock, K., Prockter M. L., Reiter, R. A., Robinson, M. S., Schaefer, E. D., Shelton, R. G., Sterner, R. E., Taylor, H. W., Watters, T. R., Williams, B. D., 2007. The Mercury Dual Imaging System on the MESSENGER Spacecraft, *Space Sci. Rev.*, 131, 247–338, 10.1007/s11214-007-9266-3.

Head, J. W., Murchie S. L., Prockter, L. M., Solomon, S. C., Chapman, C. R., Strom, R. G., Watters, T. R., Blewett, D. T., Gillis-Davis, J. J., Fassett C. I., Dickson, J. L., Morgan, G. A., Kerber, L., 2009. Volcanism on Mercury: Evidence from the first MESSENGER flyby for extrusive and explosive activity and the volcanic origin of plains, *Earth Planet. Sci. Lett.*, 285, 227–242.

Head, J. W., Chapman, C. R., Strom, R. G., Fassett, C. I., Denevi, B. W., Blewett, D. T., Ernst, C. M., Watters, T. R., Solomon, S. C., Murchie, S. L., Prockter M. L., Chabot, N. L., Gillis-Davis, J. J., Goudge, T. A., Baker, D. M., H., Hurvitz, D. M., Ostrach, L. R., Xiao, Z., Merline, W. J., Kerber, L., Dickson, J. L., Oberst, J., Byrne, P. K., Klimczak, C., Nittler, R. L., 2011. Flood volcanism in the northern high latitudes of Mercury revealed by MESSENGER, *Science*, 333, 1853-1856, 10.1126/science.1211997.

Helbert, J., Jessberger, E., Benkhoff, J., Arnold, G., Banaszkiewicz, M., Bischoff, A., Blecka, M., Calcutt, S., Coangeli, L., Coradini, A., Erard, S., Fonti, S., Killen, R., Knollenberg, J., Kührt, E., Mann, I., Mall, U., Moroz, L., Peter, G., Rataj, M., Robinson, M. S., Spohn, T., Sprague, A., Stöffler, D., Taylor, F., Warrell, J., 2005. MERTIS – a thermal infrared imaging spectrometer for the Bepi-Colombo mission, 36th Lunar Planet. Sci. C., The Woodlands, Texas.

Helbert, J., Maturilli, A., 2009. The emissivity of a fine-grained labradorite sample at typical Mercury dayside temperatures, *Earth Planet. Sci. Lett.*, 285, 347-354.

Hiesinger, H., Head, J. W., Wolf, U., Jaumann, R., Neukum, G., 2002. Lunar mare basalt flow units: Thicknesses determined from crater size-frequency distributions, *Geophys. Res. Lett.*, 29, 8, 1-4, 10.1029/2002GL014847.

Hiesinger, H., Helbert, J., MERTISCo-I team, 2010. The Mercury Radiometer and Thermal Infrared Spectrometer (MERTIS)for the Bepi Colombo mission, *Planet. Space Sci.*, 58, 144–165.

Hiesinger, H., van der Bogert, C. H., Pasckert, J. H., Funcke, R., Giacomini, L., Ostrach, L. R., Robinson, M. S., 2012. How old are young lunar craters?, *J. Geophys. Res.*, 117, E00H10, 1-15, 10.1029/2011JE003935.

Holsapple, K. A., Housen, K. R., 2007, Ejecta from Impact Craters, *Icarus*, 187, 1, 345–356.

Hugh-Jones, D., 1997. Thermal expansion of $MgSiO_3$ and $FeSiO_3$ ortho- and clinopyroxenes, *Am. Mineral.*, 82, , 689-696.

Kennedy, T., Freed, A. M., Solomon, S. C., 2008. Mechanisms of faulting in and around

Caloris basin, Mercury, *J. Geophys. Res.*, 113, E08004.

King, S. D., 2008. Pattern of lobate scarps on Mercury's surface reproduced by a model of mantle convection, *Nature Geosc.*, 1, 229-232, 10.1038/ngeo152.

Klimczak, C., Watters, T. R., Ernst, C. M., Freed, A. M., Byrne, P. K., Solomon, S. C., Blair, D. M., Head, J. W., 2012. Deformation associated with ghost craters and basins in volcanic smooth plains on Mercury: Strain analysis and implications for plains evolution, *J. Geophys. Res.*, 117, E00L03, 10.1029/2012JE004100.

Kneissl, T., van Gasselt, S., Neukum, G., 2011. Map-projection-independent crater size-frequency determination in GIS environments – New software tool for Arc-GIS, *Planet. Space Sci.*, 59, 1243-1254.

Mann, P., 2007. Global catalogue, classification and tectonic origins of restraining and releasing bends on active and ancient strike-slip fault systems, Cunningham, W.D., and Mann, P.

Marchi, S., Mottola, S., Cremonese, G., Massironi, M., Martellato, E., 2009. A new chronology for the Moon and Mercury, *Astron. J.*, 137, 4936-4948.

Marchi, S., Massironi, M., Cremonese, G., Martellato, E., Giacomini, L., Prockter M. L., 2011. The effects of the target material properties and layering on the crater chronology: The case of Raditladi and Rachmaninoff basins on Mercury, *Planet. Space Sci.*, 59, 1968-1980.

Massironi, M., Cremonese, G., Marchi, S., Martellato, E., Mottola, S., Wagner, R. J., 2009. Mercury's geochronology revised by applying Model Production Function to Mariner 10 data: Geological implications, *Geophys. Res. Lett.*, 36, L21204, 10.1029/2009GL040353.

Massironi, M., Di Achille, G., Ferrari, S., Giacomini, L., Popa, C., Pozzobon, R., Zusi, M., Cremonese, G., Palumbo, P., 2012. Strike-slip kinematics on Mercury: evidences and implications, 1924, 43rd Lunar Planet. Sci. C., The Woodlands, Texas, .

Maturilli, A., Helbert, J., Witzke, J., Moroz, L., 2006. Emissivity measurements of analogue materials for the interpretation of data from PFS on Mars Express and MERTIS on Bepi-Colombo, *Planet. Space Sci.*, 54, , 1057-1064.

Maturilli, A., Helbert, J., Moroz, L., 2008, The Berlin emissivity database (BED), *Planet. Space Sci.*, 56, , 420-425.

Maxwell, T. A., El-Baz, F., Ward, S. W., 1975. Distribution, morphology, and origin of ridges and arches in Mare Serenitatis, *Geol. Soc. Am. Bull.*, 86, , 1273-1278., ,

McEwen, A. S., Bierhaus, E. B., 2006. The importance of secondary cratering to age constraints on planetary surfaces, *Annu. Rev. Earth Plan. Sci.*, 34, 535-567.

Melosh, H. J., Dzurisin, D., 1978. Mercurian global tectonics: A consequence of tidal despinning?, *Icarus*, 35, 227-236.

Melosh, H. J., McKinnon, W.B., 1988. The tectonics of Mercury, *Mercury*, F. Vilas, C. R. Chapman, and M. S. Matthews, Univ. of Ariz. Press, Tucson.

Melosh, H. J., 1989. Impact Cratering: a geological process, 11, *Oxford Monographs on*

Geology and Geophysics, Oxford University Press, New York, NY.

Michel, N.C., Hauck, S. A., Solomon, S. C., Phillips, R. J., Roberts, J. H., Zuber, M. T, 2011. Implications of MESSENGER observations for mantle convection on Mercury., 1671, 43rd Lunar Planet. Sci. C., The Woodlands, Texas.

Melosh, H. J., Dzurisin, D., 1978. Mercurian global tectonics: A consequence of tidal despinning?, *Icarus*, 35, , 227 236.

Melosh, H. J., 2011. *Planetary Surface Processes*, H. J. Melosh, Purdue University, Indiana.

Murchie, S. L., Watters, T. R., Robinson, M. S., Head, J. W., Strom, R. G., Chapman, C. R., Solomon, S. C., McClintock, W. E., Prockter M. L., Domingue, D. L., Blewett, D. T., 2008. Geology of the Caloris basin, Mercury: a new view from MESSENGER, *Science*, 321, 73-76.

Murray, B. C., 1975. The Mariner 10 pictures of Mercury: an overview, *J. Geophys. Res.*, 80, 2342– 2344.

Neukum, G., Horn, P., 1975. Effects of lava flows on lunar crater populations, *The Moon*, 15, 205-222.

Neukum, G., Ivanov, B. A., Hartmann, W. K., 2001a. Cratering records in the inner solar system in relation to the lunar reference system, *Space Sci. Rev.*, 96, 55-86.

Neukum, G., Oberst, J., Hoffmann, H., Wagner, R., Ivanov, B. A., 2001b. Geologic evolution and cratering history of Mercury, *Planet. Space Sci.*, 49, 1507-1521.

Nestola, F., Tribaudino, M., Boffa Ballaran, T., Liebske, C., Bruno, M., 2007. The crystal structure of pyroxenes along the jadeite-hedenbergite and jadeite-aegirine joins, *Am. Mineral.*, 92, 1492-1501.

Nestola, F., Ballaran, T. B., Liebske, C., Thompson, R., Downs, R. T., 2008. The effect of the hedenbergitic substitution on the compressibility of jadeite, *Am. Mineral.*, 93, 7, 1005-1013.

Nittler, R. L., Starr, R. D., Weider, S. Z., McCoy, T. J., Boynton, W. V., Ebel, D. S., Ernst, C. M., Evans, L. G., Goldsten, J. O., Hamara, D. K., Lawrenc e, D. J., McNutt, R. L., Schlemm, C. E., Solomon, S. C., Sprague, A. L., 2011. The major-element composition of Mercury's surface from MESSENGER X-ray spectrometry, *Science*, 333, 1847-1850, 10.1126/science.1211567.

Oberti, R., Caporuscio, F.A., 1991. Crystal chemistry of clinopyroxenes from mantle eclogites: a study of the key role of the M2 site population by means of crystal-structure refinement, *Am. Mineral.*, 76, 1141-1152.

Peplowsky, P. N., Evans, L. G., Hauck, S. A., McCoy, T. J., Boynton, W. V., Gillis-Davis, J. J., Gillis-Davis, J. J., Ebel, D. S., Goldsten, J. O., Hamara, D. K., Lauwrence, D. J., McNutt, R. L., Nittler, R. L., Solomon, S. C., Rhodes, E. A., Sprague, A. L., Starr, R. D., Stockstill-Cahill, K. R., 2011. Radioactive elements on Mercury's surface from MESSENGER: Implications for the planet's formation and evolution, *Science*, 333, 1850-1852, 10.1126/science.1211576.

Philip, H., Cisternas, A., Gvishiani, A., Gorshkov, A., 1989. The Caucasus: an actual

example of the stages of continental collision, *Tectonophysics,* 161, 1-21.

Platz, T., Michael, G. G., Neukum, G., 2010, Confident thickness estimates for planetary surface deposits from concealed crater populations, *Earth Planet. Sci. Lett.*, 293, 3-4, 388–395.

Pouchou, J. L., Pichoir, F.,, 1991, Quantitative analysis of homogeneous or stratified microvolumes applying the model “PAP”, 31-76, , Electron Probe Quantitation, Heinrich K., Newbury D., , Plenum Press, New- York.

Preusker, F., Oberst, J., Head, J. W., Watters, T. R., Robinson, M. S., Zuber, M. T., Solomon, S. C., 2011. Stereo topographic models of Mercury after three MESSENGER flybys, *Planet. Space Sci.*, 59, 1910-1917.

Preusker, F., Oberst, J., Blewett, D. T., Gwinner, K., Head, J. W., Murchie, S. R., Robinson, M. S., Watters, T. R., Zuber, M. T., Solomon, S. C., 2012. Digital Terrain Models of Mercury from MESSENGER Stereo Images, 1913, 43rd Lunar Planet. Sci. C., The Woodlands, Texas.

Prockter M. L., Ernst, C. M., Denevi, B. W., Chapman, C. R., Head, J. W., Fassett, C. I., Merline, W. J., Solomon, S. C., Watters, T. R., Strom, R. G., Cremonese, G., Marchi, S., Massironi, M., 2010. Evidence for young volcanism on Mercury from the third MESSENGER flyby, *Science,* 329, 668-671, 10.1126/science.1188186.

Rayner, M. A., McCubbin, F. M., Lucey, P. G., Jeffrey Talyor, G., Gillis-Davis, J. J., 2010. Mercury surface composition: Integrating petrologic modeling and remote sensing data to place constraints on FeO abundance, *Icarus,* 209, 301-313.

Roberts, J. H., Barnouin, O. S., 2012. The effect of the Caloris impact on the mantle dynamics and volcanism of Mercury, *J. Geophys. Res.,* 117, E02007, 10.1029/2011JE003876.

Robinson, M. S., Lucey, P. G., 1997. Recalibrated Mariner 10 color mosaics: implications for mercurian volcanism, *Science,* 275, 197-200.

Robinson, M. S., Murchie, S. L., Blewett, D. T., Domingue, D. L., Hawkins, S. E., Head, J. W., Holsclaw, G. M., McClintock, W. E., McCoy, T. J., McNutt, R. L., Prockter, L. M., Solomon, S. C., Watters, T. R., 2008. Reflectance and color variations on Mercury: indicators of regolith processes and compositional heterogeneity, *Science,* 321, 66-69.

Rossi, G., Oberti, R., Dal Negro, A., Molin, G. M., Meilini, M., 1987. Residual electron density at the M2 site in C2/c clinopyroxenes: relationships with bulk chemistry and sub-solidus evolution, *Phys. Chem. Miner.,* 14, 514–520.

Ruff, S. W., Christensen, P. R., Barbera, P. W., Anderson, D. L., 1997. Quantitative thermal emissions pectroscopy of minerals: A laboratory technique for measurement and calibration, *J. Geophys. Res.,* 102, 14, 899-913.

Ruiz, J., Lòpez, V., Dohm, J. M., Fernàndez, C., 2012. Structural control of scarps in the Rembrandt region of Mercury, *Icarus,* 219, , 511-514.

Schultz, R. A., 2000. Localization of bedding-plane slip and backthrust faults above blind thrust faults: keys to wrinkle ridge structure, *J. Geophys. Res.*, 105, 12035-

12052.

Schultz, R. A., Hauber, E., Kattenhorn, S. A., Okubo, C. H., Watters, T. R., 2010. Interpretation and analysis of planetary structures, *J. Struct. Geol.*, 32, , 855-875.

Shannon, R. D., 1976. Revised effective ionic radii and systematic studies of interatomic distances in halides and chalcogenides, *Acta Crystallogr. A*, 32, 751-767.

Sheldrick, G. M., Programs for Crystal Structure Analysis (Release 97-2), Institüt für Anorganische Chemie der Universität, Göttingen, Germany,

Smith, D. E., Zuber, M. T., Phillips, R. J., Solomon, S. C., Hauck, S. A., Lemoine, F. G., Mazarico, E., Neumann, G. A., Peale, S. J., Margot, J., Johnson, C. L., Torrence, M. H., Perry, M. E., Rowlands, D. D., Goossens, S., Head, J. W., Taylor, A. H., 2012. Gravity field and internal structure of Mercury from MESSENGER, *Science,* 336, 214-217, 10.1126/science.1218809.

Solomon, S. C., Head, J. W., 1980. Lunar mascon basins: Lava filling, tectonics, and evolution of the lithosphere, *Rev. Geophys. Space Phys.*, 18, 107-141.

Solomon, S. C., McNutt, R. L., Gold, R. E., Acuña, M. H., Baker, D. N., Boynton, W. V., Chapman, C. R., Cheng, A. F., Gloeckler, G., Head, J. W., Krimigis, S. M., McClintock, W. E., Murchie, S. L., Peale, S. J., Phillips, R. J., Robinson, M. S., Slavin, J. A., Smith, D. E., Strom, R. G., Trombka, J. I., Zuber, M. T., 2001. The MESSENGER mission to Mercury: scientific objectives and implementation, *Planet. Space Sci.*, 49, 1445–1465.

Solomon, S. C., McNutt, R. L., Gold, R. E., Domingue, D. L., 2007. MESSENGER Mission Overview, *Space Sci. Rev.*, 13, 3-39, 10.1007/s11214-007-9247-6.

Solomon, S. C., McNutt, R. L., Watters, T. R., Lawrence, D. J., Feldman, W. C., Head, J. W., Krimigis, S. M., Murchie, S. R., Phillips, R. J., Slavin, J. A., Zuber, M. T., 2008. Return to Mercury: a global perspective on MESSENGER's first Mercury flyby, *Science,* 321, 59-62.

Sprague, A. L., Deutsch, L. K., Hora, J., Fazio, G. G., Ludwig, B., Emery, J., Hoffmann, W. F., 2000. Mid-infrared (8.1–12.5 μm) imaging of Mercury, *Icarus,* 147, 421-432.

Sprague, A. L., Emery, J. P., Donaldson, K. L., Russell, R. W., Lynch, D. K., Mazuk, A. L., 2002. Mercury: Mid-infrared (3–13.5 lm) observations show heterogeneous composition, presence of intermediate and basic soil types, and pyroxene, *Meteorit. Planet. Sci.*, 37, 1255–1268.

Sprague, A., Warell, J., Cremonese, G., Langevin, Y., Helbert, J., Wurz, P., Veselovsky, I., Orsini S., Milillo, A., 2007. Mercury's surface composition and character as measured by ground-based observations, *Space Sci. Rev.*, 132, 399–431.

Sprague, A. L., Donaldson Hanna, K. L., Kozlowski, R. W. H., Helbert, J., Maturilli, A., Warell, J. B., Hora, J. L., 2009. Spectral emissivity measurements of Mercury's surface indicate Mg- and Ca-rich mineralogy, K-spar, Na-rich plagioclase, rutile, with possible perovskite, and garnet, *Planet. Space Sci.*, 57, 364–383.

Spudis, P. D., Guest, E. J., 1988. Stratigraphy and geologic history of Mercury, 118-164, *Mercury,* F. Vilas, C. R. Chapman, and M. S. Matthews, Univ. of Ariz. Press, Tucson.

Strom, R. G., 1972. Lunar mare ridges, rings and volcanic ring complexes, *Mod. Geol.*, II, 133-157.

Strom, R. G., Trask, N. J., Guest, E. J., 1975. Tectonism and volcanism on Mercury, *J. Geophys. Res.*, 80, 2478-2507.

Strom, R. G., 1987. *Mercury. The elusive planet*, R. G. Strom, Smithsonian Institution Press, Washington, D.C.

Strom, R. G., Sprague, A. L., 2003. *Exploring Mercury: The Iron Planet*, Springer/Praxis, New York.

Strom, R. G., Malhotra, R., Ito, T., Yoshida, F., Kring, D. A., 2005. The origin of planetary impactors in the inner solar system, *Science*, 309, 1847–1850.

Thomas, P. G., 1997. Are there other tectonics than tidal despinning, global contraction and Caloris related events on Mercury? A review of questions and problems, *Planet. Space Sci.*, 45, 1, 1-13.

Toksöz, M. N., Press, F., Anderson, K., Dainty, A., Latham, G., Ewing, M., Dorman, J., Lammlein, D., Sutton, G., Duennebier, F., Nakamura, Y., 1972. Lunar crust: Structure and composition, *Science*, 176, 1012–1016.

Trask, N. J., Guest, E. J., 1975. Preliminary Geologic Terrain Map of Mercury, *J. Geophys. Res.*, 80, 17, 2461-2477, 10.1029/JB080i017p02461.

Tribaudino, M., Nestola, F., Cámara, F., and Domeneghetti, M. C., 2002, The high-temperature $P2_1/c$-$C2/c$ phase transition in Fe-free pyroxene ($Ca_{0.5}Mg_{1.5}Si_2O_6$): Structural and thermodynamic behaviour, *Am. Mineral.*, 87, 648–657.

Tribaudino, M., Nestola, F., Meneghini, C., Bromiley, G. D., 2003. The high-temperature *P*2/*c*(1)-*C*2/*c* phase transition in Fe-free Ca-rich *P*2(1)/*c* clinopyroxenes, *Phys. Chem. Miner.*, 30, 9, 527-535.

Tribaudino, M., Nestola, F., Bruno, M., Boffa Ballaran, T., Liebske, C., 2008. Therma expansion along the $NaAlSi_2O_6$-$NaFe^{3+}Si_2O_6$ and $NaAlSi_2O_6$-$CaFe^{2+}Si_2O_6$, *Phys. Chem. Miner.*, 35, 241-248.

Vasavada, A. R., Paige, D. A., Wood, S. E., 1999. Near surface temperatures on Mercury and the Moon and the stability of polar ice deposits, *Icarus*, 141, 179-193.

Vilas, F.,1985. Mercury: Absence of crystalline Fe^{2+} in the regolith, *Icarus*, 64, 1, 133-138.

Warell, J. B., Sprague, A. L., Emery, J. P., Kozlowski, R. W. H., Long, A., 2006. The 0.7-5.3 µm IR spectra of Mercury and the Moon: Evidence for high-Ca clinopyroxene on Mercury, *Icarus*, 180, 281-291.

Warell, J. B., Sprague, A. L., Kozlowski, R. W. H., Rothery, D. A., Lewis, N., Helbert, J., Cloutis, E., 2010. Constraints on Mercury's surface composition from MESSENGER and ground-based spectroscopy, *Icarus*, 209, 138–163.

Watters, T. R., 1988. Wrinkle ridge assemblages on the terrestrial planets, *J. Geophys. Res.*, 93, 10236-10254.

Watters, T. R., Robinson, M. S., Cook, A. C., 1998. Topography of lobate scarps on

Mercury: new constraints on the planet's contraction, *Geology*, 26, 991-994. , , ,

Watters, T. R., Robinson, M. S., Cook, A. C., Bina, C. R., Spudis, P. D., 2004. Thrust faults and the global contraction of Mercury, *Geophys. Res. Lett.*, 31, L04071.

Watters, T. R., Nimmo, F., Robinson, M. S., 2005. Extensional troughs in the Caloris Basin of Mercury: Evidence of lateral crustal flow, *Geology*, 33, 669-672.

Watters, T. R., Solomon, S. C., Robinson, M. S., Head, J. W., Andrè, S. L., Hauck, S. A., Murchie, S. L., 2009a. The tectonics of Mercury: The view after MESSENGER's first flyby, *Earth Planet. Sci. Lett.*, 285, 283-296.

Watters, T. R., Head, J. W., Solomon, S. C., Robinson, M. S., Chapman, C. R., Denevi, B. W., Fassett, C. I., Murchie, S. L., Strom, R. G., 2009b. Evolution of Rembrandt impact basin on Mercury, *Science*, 324, 618-621, 10.1126/science.1172109.

Watters, T. R., Murchie, S. L., Robinson, M. S., Solomon, S. C., Denevi, B. W., André, S. L., Head, J. W., 2009c. Emplacement and tectonic deformation of smooth plains in the Caloris basin, Mercury, *Earth Planet. Sci. Lett.*, 285, 309-319.

Watters, T. R., Nimmo, F., 2010. The tectonics of Mercury, 15-79, *Planetary Tectonics*, T. R. Watters and R. A. Schultz, Cambridge Univ. Press, Cambridge.

Watters, T. R., Solomon, S. C., Klimczak, C., Freed, A. M., Head, J. W., Ernst, C. M., Blair, D. M., Goudge, T. A., Byrne, P. K., 2012a. Extension and contraction within volcanically buried impact craters and basins on Mercury, *Geology*, 40, 1123-1126, 10.1130/G33725.1.

Watters, T. R., Solomon, S. C., Robinson, M. S., Head, J. W., Strom, R. G., Klimczak, C., Byrne, P. K., Enns, A. C., Ernst, C. M., Prockter, L. M., Murchie, S. L., Oberst, J., Preusker, F., Zuber, M. T., Hauck, S. A., Phillips, R. J., 2012b. Tectonic Features on Mercury: An Orbital View with MESSENGER, 1659, 43rd Lunar Planet. Sci. C., The Woodlands, Texas.

Watters, T. R., Cook, A. C., Robinson, M. S., 2001. Large-scale lobate scarps in the southern hemisphere of Mercury, *Planet. Space Sci.*, 49, 1523-1530.

Weidenschilling, S. J., 1978. Iron/silicate fractionation and the origin of Mercury, *Icarus*, 35, , 99-111.

Wilson, A. J. C., 1995. International Tables for Crystallography, Vol. C, Dordrecht: Kluwer Academic Publishers.

Zuber, M. T., Smith, D. E., Phillips, R. J., Solomon, S. C., Neumann, G. A., Hauck, S. A., Peale, S. J., Barnouin, O. S., Head, J. W., Johnson, C. L., Lemoine, F. G., Mazarico, E., Sun, X., Torrence, M. H., Freed, A. M., Klimczak, C., Margot, J., Oberst, J., Perry, M. E., McNutt, R. L., Balcerski, J. A., Michel, N., Talpe, M. J., Yang, D., 2012. Topography of the northern hemisphere of Mercury from MESSENGER Mercury Altimetry, *Science*, 336, 217-220.

Appendix

EPSC Abstracts
Vol. 5, EPSC2010-712, 2010
European Planetary Science Congress 2010

Geo-structural mapping and age determinations of Rembrandt Basin region

S. Ferrari (1), **M. Massironi** (1,2), L. Giacomini (1), E. Martellato (2), G. Cremonese (3), D. A. Rothery (4), L. M. Prockter (5) and S. Marchi (6)
(1) Dipartimento di Geoscienze, Università di Padova, Italy, (2) CISAS, Università di Padova, Italy, (3) INAF - Osservatorio Astronomico di Padova, Italy, (4) Open University, Milton Keynes, United Kingdom, (5) Johns Hopkins University Applied Physics Laboratory, Laurel, Mariland, USA, (6) Dipartimento di Astronomia, Università di Padova, Italy
(sabrina.ferrari@studenti.unipd.it / Fax: +39-049-8722010)

Abstract

During its second and third flybys, MESSENGER imaged a new large and well-preserved basin called Rembrandt Basin [1] in Mercury's southern hemisphere. In attempt to reveal the basin evolution, we used MESSENGER MDIS mosaics to map its geological units and infer - where possible - their stratigraphic relationships. Thus, we fixed the contractional and extensional local patterns and the global tectonic features. In addition, we performed crater counts on several of these units and derived age estimates by applying the Model Production Function (MPF) [2].

1. Introduction

Rembrandt basin is a 715-km-diameter impact feature which displays a distinct, hummocky rim, broken up by the presence of several large impact craters. Its interior is partially filled by volcanic materials, that extend up to the southern, eastern and part of the western rims [1], and is crossed by a marked lobate scarp. In this work we have performed a geological mapping and age determination of several units of the basin as well as a structural and kinematic analysis mainly focused on the mayor Rembrandt scarp.

2. Geo-structural mapping

Rembrandt Basin displays evidence of both global-scale and basin-localized deformations, in some cases possibly controlled by the rheological layering within the crust. Extensional features are essentially radial and confined to the *Inner Plains*, displaying one or more uplifts episodes of the inner basin. The more widespread wrinkle ridges form a polygonal pattern of radial and concentric features on the whole floor, probably due to one or more near-surface compressional stages [1]. Thus, through their cross-cutting relationships, we attempted to distinguish the cascade of events. About global landforms, we focused on the 1000-km long Rembrandt scarp. The structures can be subdivided into three branches: the southern one with clear evidences of a right-lateral strike slip movement acting together with an inverse kinematics, the northern one with some evidences of a left-lateral component, well-recorded in the displacement of a younger 60-km diameter crater, (fig. 1) and the central sector without any evidence of strike slip movements.

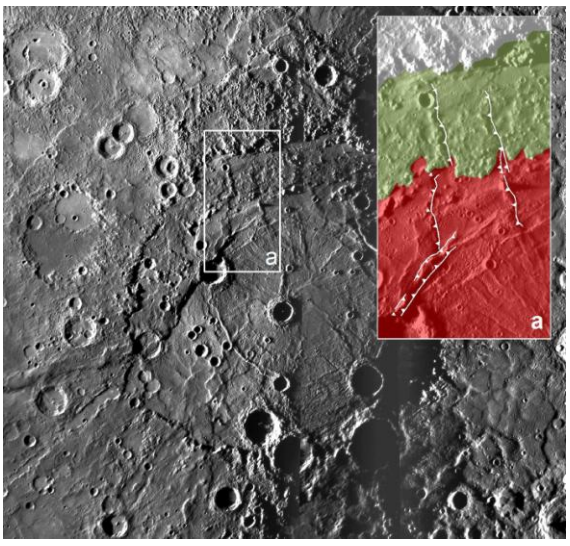

Figure 1: Rembrandt Basin from MESSENGER MDIS-NAC image and (a) geological sketch of the northern-branch of Rembrandt scarp.

The resulting bow shape geometry could be compared with the Beagle Rupes feature despite Rembrandt structure does not show a clear frontal ramp but two lateral ramps converging in a narrow cusp. Similarly, it may imply special conditions of

weakness inside the crust [4]. The main phase responsible of the Rembrandt scarp build-up was followed by minor compressional structures detected within younger craters and possibly associated to a slowing down phase of the global contraction.

3. Age determinations

We subdivided the basin into two main systems for age determination purposes: the volcanic *Inner Plains*, that flooded the crater floor after the impact, and the *Hummocky-Rim Area*, that includes both rim materials and fallout proximal ejecta. The age assessment was obtained by adopting Marchi et al.' (2009) chronological model [2], because it takes into account both (1) the Main Belt Asteroids (MBAs) and the Near Earth Objects (NEOs) projectile populations and (2) the uppermost layering of the target [5]. More in detail, we adopted a lunar-like crustal structure and set fractured silicates of variable thickness on top of a bulk anorthositic crust in turn laying above a peridotitic mantle. In the case of the Rembrandt basin systems, the adopted layering for MPF age determination was well constrained by the good statistics and crater-diameter range of the data set. Indeed, the Crater Size-Frequency Distribution (CSFD) of the hummocky *Rim Area* shows a typical kink, which likely reflects a layer of fractured material with a thickness of about 8 km on the other hand the *Inner Plains* do not show any kink despite the wide crater diameter range that characterize its population. Considering these constraints on the crustal layering and an MBA population, MPF ages of Rim Area and Inner Plain are about 3.7 and 3.6 Ga, respectively [6].

4. Conclusions

The derived MPF ages of Rembrandt Basin inner units imply a short stage of volcanism straight after the basin formation at around 3.6 Ga [6], while our structural analysis shows a long lasting activity of global contraction well-expressed along the Rembrandt scarp. In addition, as well as the Beagle Rupes case, the Rembrandt scarp displays geometries and kinematic indicators suggesting the presence of a basal detachment.

References

[1] Watters, T. R., Head, J. W., Solomon, S. C., Robinson, M. S., Chapman, C. R., Denevi, B. W., Fassett, C. I., Murchie, S. L., and Strom, R. G.: Evolution of the Rembrandt Impact Basin on Mercury, Science, Vol. 324, pp. 618-621, 2009.

[2] Marchi, S., Mottola, S., Cremonese, G., Massironi, M., and Martellato, E.: A new Chronology for the Moon and Mercury, Astronomical Journal, vol. 137, pp. 4936-4948, 2009.

[3] Spudis, P.D. and Guest, J.E.: Stratigraphy and geologic history of Mercury. In: Vilas, F., Chapman, C.R. and Matthews, M.S., Editors: Mercury, The University of Arizona Press, 1988.

[4] Rothery, D. A. and Massironi, M.: Beagle Rupes – evidence for a basal decollement of regional extent in Mercury's lithosphere, Icarus (In Press), 2010.

[5] Massironi, M., Cremonese, G., Marchi, S., Martellato, E., Mottola, S. and Wagner, R. J.: Mercury's geochronology revised by applying Model Production Function to Mariner 10 data: Geological implications, Geophys. Res. Lett., vol. 36, L21204, 2009.

[6] Martellato, E., Massironi. M., Cremonese. G., Marchi, S., Ferrari, S. and Prockter, L. M.: Age Determination of Raditladi and Rembrandt Basins and related Geological Units, LPSC, 2148, 2010.

EPSC Abstracts
Vol. 6, EPSC-DPS2011-963-1, 2011
EPSC-DPS Joint Meeting 2011

Beagle Rupes and Rembrandt scarp: a comparison on Mercury surface.

S. Ferrari (1), M. Massironi (1,2), D. A. Rothery (3), G. Cremonese (4)
(1) Dipartimento di Geoscienze, Università degli Studi di Padova, Italy, (2) CISAS, Università degli Studi di Padova, Italy, (3) Open University, Milton Keynes, United Kingdom, (4) INAF - Osservatorio Astronomico di Padova, Italy
(sabrina.ferrari@studenti.unipd.it / Fax: +39-049-8729134)

Abstract

Areas of crustal convergence and shortening on Earth, Mars and Venus are often characterized by structural domains where thrust faults are associated with strike-slip systems [1]. In the case of Mercury most structures maintain a wide elongated frontal scarp and only few of them show kinematic indicators of lateral slip. The comparison between two Mercurian linked fault systems like Beagle Rupes [2] [3] and Rembrandt scarp [4] could aid understanding of whether diverse hermean strike-slip structures are influenced by geological context such as surface heterogeneity and crustal layering or have different deformational history.

1. Introduction

During these last decades several contractional forms had been recognized and mapped on Mercury, firstly using Mariner10 and then MESSENGER data [5]. In cross section, the structures consist of a steeply sloping scarp and a gently sloping back scarp [6] forming an arched planar shape, so they are usually called lobate scarps. Usually regarded as caused by gradual cooling of the planet, these features are the clearest evidence of crustal deformation present on Mercury, being the surface expression of thrust faulting initiated after the period of Heavy Bombardment (3.8 Gyr ago) [8]. However, other origins such as despinning and mantle convection have been suggested to explain common orientations and regional vergences of some structures [9]. Despite the plethora of studies dealing with lobate scarps on Mercury and other planetary surfaces (Mars and Moon), very few structures have been recognized as linked fault systems. Among them Beagle Rupes seems to be the most prominent one, although also the Rembrandt scarp may show some evidence of linkages between fault segments (fig. 1).

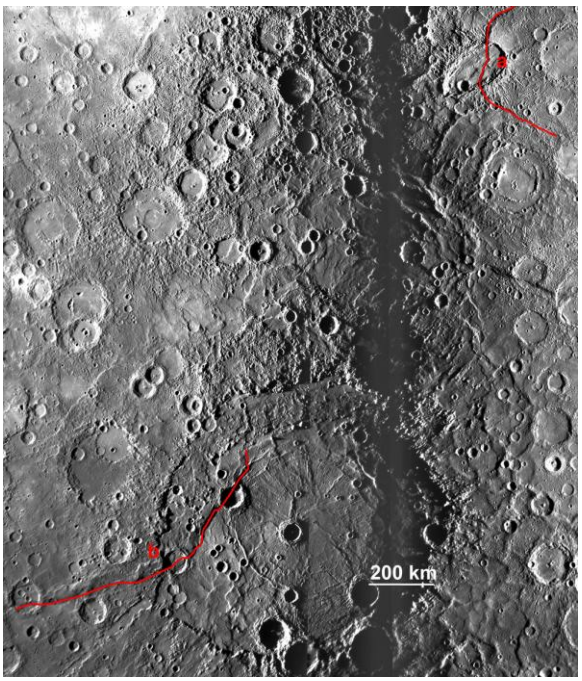

Figure 1: MESSENGER MDIS-NAC image showing both (a) Beagle Rupes at the equatorial area (upper right) and (b) Rembrandt scarp (lower left), which partially cross-cuts the 715-km-diameter Rembrandt impact basin centered at 33.2 S - 88.2 E. The image is courtesy of USGS Astrogeology Science Center http://astrogeology.usgs.gov and http://messenger.jhuapl.edu

2. Beagle Rupes and Rembrandt scarp linked fault systems

In the context of the development of giant tectonic structures like lobate scarps, the equatorial Beagle Rupes can be considered a special case, because it has been interpreted as a component of a linked fault system by Rothery and Massironi [3]. They suggest that Beagle Rupes displays a frontal scarp terminated by transpressive lateral ramps. Indeed, the structure

consists of two linked north–south trending arcs that turn at the ends to become straight scarps trending northeast and southeast. These straight scarps have been interpreted to be lateral oblique ramps bounding a thrust sheet [10][11], which transfer motion to a series of younger fault scarps by out-of-sequence thrusting [3]. The inferred dip angle of the main thrust seems to decrease with depth and to be as low as to imply an along-dip displacement. A low angle and the presence of other diagnostic features are coherent with a basal decollement that occurs within or at the base of Mercury's lithosphere. Candidates for the decollement must imply a change in mechanical properties and therefore could be the base of the elastic lithosphere, the base of the crust, or a regional low-angle discontinuity within the crust. The single example of Beagle Rupes provides no clear basis for deciding among the global chances and the structure seems not to be affected by any visible regional discontinuity like buried basins [5] [6].

Another wide structure recently discovered on the south hemisphere of Mercury and named Rembrandt scarp [4] appears to be a linked fault system, but shows important differences from Beagle Rupes. In particular the scarp partially cuts the large Rembrandt Basin and has two distinct branches with opposite strike-slip component converging towards a narrow cusp. This unusual geometry could be the result of multiple episodes of deformation which may have reworked some inherited structures now representing parts of the final scarp. Alternatively, the Rembrandt Basin may have severely affected the shape and development of the scarp constraining its geometry. Indeed, the structures inside and outside Rembrandt basin display different behavior. The crustal layering, which can be hypothesized is likely to be inhomogeneous in the region of the Rembrandt scarp where it cuts through the huge Rembrandt basin.

The timing of formation of the lobate scarp thrust faults can be constrained by the age of the materials they deform - 3.6 Ga for the Rembrandt Basin inner plains [12]. However we have observed minor compressional structures within younger craters cutting the main scarp, so the contractional activity in this area seems to be prolonged.

References

[1] Watters, T. R.: System of tectonic features common to Earth, Mars and Venus, Geology, Vol. 20, pp. 609-612, 1992.

[2] Solomon, S. C., McNutt, R. L., Watters, T. R., Lawrence, D. J., Feldman, W. C., Head, J. W., Krimigis, S. M., Murchie, S. L., Phillips, R. J., Slavin, J. A. and Zuber, M. T.: Return to Mercury: a global perspective on MESSENGER's first Mercury flyby, Science, Vol. 321, pp. 59-62, 2008.

[3] Rothery, D. A. and Massironi, M.: Beagle Rupes - Evidence of a basal decollement of regional extent in Mercury's lithosphere, Icarus, Vol. 209, pp. 256-261, 2010.

[4] Watters, T. R., Head, J. W., Solomon, S. C., Robinson, M. S., Chapman, C. R., Denevi, B. W., Fassett, C. I., Murchie, S. L., and Strom, R. G.: Evolution of the Rembrandt Impact Basin on Mercury, Science, Vol. 324, pp. 618-621, 2009.

[5] Watters, T. R., Robinson, M. S., Bina, C. R. and Spudis, P. D.: Thrust faults and the global contraction of Mercury, Geophysical Research Letters, Vol. 31, L04071 doi:10.1029/2003GL019171, 2004.

[6] Watters, T. R., Robinson, M. S. and Cook, A. C.: Large-scale lobate scarps in the southern hemisphere of Mercury, Planet. Space Sci., Vol. 49, pp. 1523-1530, 2001.

[7] Strom, R. G., Trask, N. J. and Guest, J. E.: Tectonism and volcanism on Mercury, J. Geophys. Res., Vol. 80, pp. 2478-2507, 1975.

[8] Watters, T. R., Schultz, R. A., Robinson, M. S. and Cook, A. C.: The mechanical and thermal structure of Mercury's early lithosphere, Geophys. Res. Lett., Vol. 29, 1542, 2002.

[9] Dombard, A. J. and Hauck, S. A.: Despinning plus global contraction and the orientation of lobate scarps on Mercury, Icarus, Vol. 198, pp. 274-276, 2008.

[10] Boyer, S. E. and Elliot, D.: Thrust systems, Bull. Am. Assoc. Petrol. Geol., Vol. 66, pp. 1196-1230, 1982.

[11] Morley, C. K.: A classification of thrust fronts, Bull. Am. Assoc. Petrol. Geol., Vol. 70, pp. 12-25, 1986.

[12] Martellato, E., Massironi. M., Cremonese. G., Marchi, S., Ferrari, S. and Prockter, L. M.: Age Determination of Raditladi and Rembrandt Basins and related geological units, 41st Lunar and Planetary Science Conference, 1-5 March 2010, The Woodlands, Texas, 2010.

EPSC Abstracts
Vol. 6, EPSC-DPS2011-1435, 2011
EPSC-DPS Joint Meeting 2011

X-ray diffraction as a function of temperature for Fo_{92}-Fa_8: implications for the hermean surface.

S. Ferrari (1), F. Nestola (1), A. Maturilli (2), M. Massironi (1, 3), J. Helbert (2), G. Redhammer (4) and SIMBIO-SYS team
(1) Dipartimento di Geoscienze, Università degli studi di Padova, Italy, (2) Institute for Planetary Research, DLR, Berlin-Adlershof, Germany, (3) CISAS, Università degli studi di Padova, Italy (4) Institute for Crystallography for the RWTH, Aachen, Germany
(sabrina.ferrari@studenti.unipd.it / Fax: +39-049-8729134)

Abstract

It is well known that the surface of Mercury shows temperature variations extremely large at specific locations [1]. Such a range can cause strong crystal structure changes and, as a consequence, the detected spectral signature could be significantly affected. Here we investigated the low-high temperature behaviour of one of the olivine, which has been recently considered as a possible constituent of the Mercury surface [2]. Aim of the work is to determine which expansion the olivine undergoes within a temperature range typical of the Mercury surface in order to verify which could be the effect of thermal expansion on a spectra.

1. An *in situ* approach

The temperature on the surface of Mercury can range in 44 earth days between 70 and 725 K at different latitudes and such variation affect significantly the crystal structure and density of the minerals and rocks present on the surface of the planet [2] [3]. As a consequence, several kinds of remote information linked to mineral structures, including relative spectral signatures, are strictly dependent on the environmental conditions and vary according to the surface temperature [4] [5]. Thus, we need to investigate the behaviour of planetary geological materials *in situ*, or under extreme temperature environments, and improve the geological interpretation and compositional inferences by applying the knowledge acquired to the analysis of available remote sensing data.

The BepiColombo Mercury Planetary Orbiter (scheduled launch in 2014) will have on board the MERTIS spectrometer (Mercury Radiometer and Thermal Infrared Spectrometer) [6] allowing to obtain crucial information on the identification and mapping of silicate minerals like feldspars, pyroxenes and olivines, that are considered among the most abundant phases for Earth planets. MERTIS will collect mineral spectral signatures in the range 7-14 μm. In fact, in such wavelength range the spectra can be used very effectively to identify the fine-scale structural properties of silicates (e.g. stretching and bending motions in the silicon-oxygen anions, metal – oxygen and lattice vibrations) and for some important mineral family, like olivine, the peak positions in this range are good indicator of their composition [7].

Here we present a new *in situ* multi-methodological laboratory approach comprehensive of high-temperature X-ray diffraction (single-crystal and powder materials) and TIR spectroscopy (in the range 7 to 14 μm). In particular, we investigated a sample of olivine with composition $Mg_{1.84}Fe_{0.16}SiO_4$ as this is among the major component of Earth's mantle, meteorites, and has been identified on the surfaces of planetary bodies, and in the spectra of astronomical targets [8]. First of all, the phase has been well characterized at room conditions by single crystal X-ray diffraction and X-ray powder diffraction, then analyzed by electron microprobe. Subsequently, each single mineral phase has been reduced in a likely grain-sizes range about the hermean surface regolith: 100-160 μm [9]. High temperature powder X-ray diffraction measurements (5° - 100° in 2θ, continuous scan mode) were carried out in the temperature range 295 K - 1273 K at the Institute for Crystallography for the RWTH in Aachen, Germany. The results emphasize an important increase of the cell volume in the hermean surface temperature range (fig. 1).

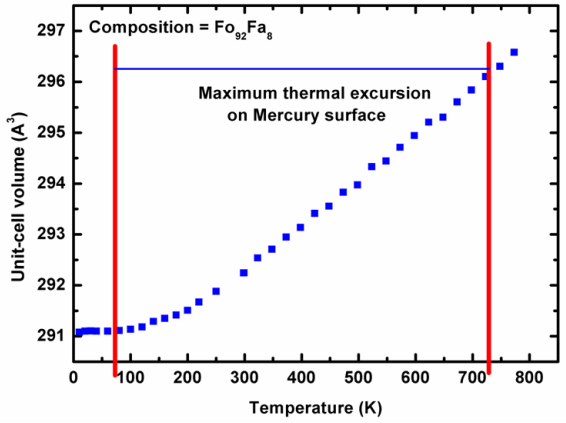

Figure 1: Cell-volume derived from high-temperature powder X-ray diffraction measurements on $Fo_{92}Fa_8$.

Comparing these results with those of Nestola et al. (2011), we could obtain the same cell variation at room conditions increasing the iron content. This means that such an increase of temperature lead to a *virtual* mineral enriched in iron content.
Concerning the TIR spectroscopy we performed laboratory measurements at the Planetary Emissivity Laboratory (PEL) at the German Aerospace Center (Deutsches Zentrum fuer Luft- und Raumfahrt in Berlin), where is available a high-temperature and vacuum spectrometer. The PEL has been build up over the last 5 years to study systematically the effect of temperature on TIR spectral signature of single mineral phases [10] and mixtures, and build up a new spectral library taking these effects into account. In our case, the sample has been investigated at four different steps and the calibrated temperatures reach 718 K. Comparing the obtained high temperature spectra with the earth-environmental spectra of ASU spectral library [11], we measure a significant shift of the major absorption features toward longer wavelength. This is in agreement with a virtual enrichment of iron in the olivine phase.

2. Conclusions

This work demonstrates that under strong temperature ranges, like the ones experienced by Mercury surface, thermal expansion is an unavoidable process and could strongly mask the actual chemistry of the mineral phases since they can appear variable through time and from place to place as a function of solar irradiation. This could drive to important misinterpretations and limit our capability of inferring compositions and rheological properties of materials from remote sensing acquisition.

References

[1] Strom, R. G.: Mercury: the elusive planet, solar system series, Smithsonian Institution Press, Washington, D. C.,1987.

[2] Vernazza, P., De Meo, F., Nedelcu, D. A., Birlan, M., Doressoundiram, A., Erard, S. and Volquardsen, E.: Resolved spectroscopy of Mercury in the near-IR SpeX/IRTF, Icarus, Vol. 209, pp. 125-137, 2010.

[3] Warell, J., Sprague, A., Kozlowski, R., Rothery, D. A., Lewis, N., Helbert, J. and Cloutis, E.: Constraints on Mercury's surface composition from MESSENGER and ground-based spectroscopy, Icarus, Vol. 209, pp. 138-163, 2010.

[4] Singer, R. B. and Roush, T. L.: Effects of Temperature on Remotely Sensed Mineral Absorption Features, Journal of Geophysical Research, Vol. 90, pp. 12434-12444, 1985.

[5] Bowey, J. E., Lee, C., Tucker, C., Hofmeister, A. M., Ade, P. A. R. and Barlow, M. J.: Temperature effects on the 15-85 μm spectra of olivines and pyroxenes, Mon. Not. R. Astron. Soc., Vol. 325, pp. 886-896, 2001.

[6] Hiesinger, H., Helbert, J., MERTIS Co-I Team: The Mercury Radiometer and Thermal Infrared Spectrometer (MERTIS) for the BepiColombo mission, Planetary and Space Science, Vol. 58, pp. 144-165, 2010.

[7] Koike, C., Chihara, H., Tsuchiyama, A., Suto, H., Sogawa, H. and Okuda, H.: Compositional dependence of infrared absorption spectra of crystalline silicate – II Natural and synthetic olivines, Astronomy and Astrophysics, Vol. 399, pp. 1101-1107, 2003.

[8] Hamilton, V. E.: Thermal infrared (vibrational) spectroscopy of Mg–Fe olivines: a review and applications to determining the composition of planetary surfaces, Geochemistry, Vol. 70, pp. 7-33, 2010.

[9] Emery, J. P., Sprague, A., Witteborn, F. C., Colwell, J. E., Kozlowski, R. W. H. and Wooden, D. H.: Mercury: thermal modeling and Mid-infrared (5-12 μm) observations, Icarus, Vol. 136, pp. 104-123, 1998.

[10] Helbert, J. and Maturilli, A.: The emissivity of a fine-grained labradorite sample at typical Mercury dayside temperatures, Earth and Planetary Science Letters, Vol. 285, pp. 347-354, 2009.

[11] Christensen, P. R., Bandfield, J. L., Hamilton, V. E., Howard, D. A., Lane, M. D., Piatek, J. L. Ruff, S. W., Stefanov, W. L.: A thermal emission spectral library of rock-forming minerals, Journal of Geophysical Research, Vol. 105, pp. 9735-9739, 2000.

EPSC Abstracts
Vol. 7 EPSC2012-874 2012
European Planetary Science Congress 2012

Complex history of the Rembrandt basin and scarp system, Mercury

Sabrina Ferrari (sabrina.ferrari@studenti.unipd.it) (1), Matteo Massironi (1,2), Christian Klimczak (3), Paul K. Byrne (3), Gabriele Cremonese (4) and Sean C. Solomon (3). (1) Department of Geosciences, University of Padua, Padova, Italy, (2) CISAS, University of Padua, Padova, Italy, (3) Department of Terrestrial Magnetism, Carnegie Institution of Washington, Washington DC 20015, USA, (4) Astronomical Observatory of Padua, INAF, Padova, Italy.

1. Introduction

During its second and third flybys, the MESSENGER spacecraft [1] imaged the well-preserved Rembrandt basin in Mercury's southern hemisphere. With a diameter of 715 km, Rembrandt is the second largest impact structure recognized on Mercury after the 1550-km-diameter Caloris basin. Rembrandt is also one of the youngest major basins [2] and formed near the end of the Late Heavy Bombardment (~3.8 Ga). Much of the basin interior has been resurfaced by smooth, high-reflectance units interpreted to be of volcanic origin [3]. These units host sets of contractional and extensional landforms generally oriented in directions radial or concentric to the basin, similar to those observed within the Caloris basin [4-6]; these structures are probably products of multiple episodes of deformation [2,7,8].

Of particular note in the Rembrandt area is a 1,000-km-long reverse fault system [9] that cuts the basin at its western rim and bends eastward toward the north, tapering into the impact material. On the basis of its shape, the structure has previously been characterized as a lobate scarp. Its formation and localization have been attributed to the global contraction of Mercury [2].

From MESSENGER flyby and orbital images, we have identified previously unrecognized kinematic indicators of strike-slip motion along the Rembrandt scarp, together with evidence of interaction between the scarp orientation and the concentric basin-related structural pattern described above. Here we show through cross-cutting relationships and scarp morphology that the development of the Rembrandt scarp was strongly influenced by tectonics related to basin formation and evolution.

2. Mapping of the Rembrandt area

Through morphological and structural analysis of Mercury Dual Imaging System (MDIS) images at different spatial resolutions, combined with stereo-derived topography [10], we created a geological map of the Rembrandt area (Fig. 1).

On the basis of spectral and textural properties of the surface, we subdivided the Rembrandt basin into three main units: (1) the *Hummocky Area*, a mixture of impact melt and breccias that in places has been reworked by smaller impacts; this unit is mainly confined along the northern part of the basin (Fig. 1); (2) the *Proximal Ejecta*, present just outside the basin rim (Fig. 1); this unit formed during the Rembrandt impact event and thus is coeval with the hummocky material; and (3) the volcanic *Inner Plains*, which flooded the crater floor (Fig. 1) after the impact and can be distinguished in sub-units through color variations (which we interpret as indicators of differences in composition, maturity, or both).

From structural mapping, we distinguish between global-scale and basin-localized structures (Fig. 1). The Rembrandt scarp, as the main global structure, represents the surface expression of a large-scale thrust fault that verges toward the south (outside the basin) to southeast (inside the basin). The thrust is accompanied by a gentle back-thrust and displays kinematic indicators of lateral shearing. We divide the Rembrandt scarp into two parts, on the basis of these lateral kinematic indicators: the portion of the scarp outside the basin shows clear evidence of right-lateral strike slip movement whereas that portion inside the basin shows some evidence of a left-lateral component.

3. Discussion

Unlike smaller lobate scarps elsewhere on the planet, the Rembrandt scarp shows unusual structural and morphological characteristics, including the abrupt change in strike direction, the contrasting lateral shearing indicators [11,12], and marked differences in scarp elevation outside and inside Rembrandt basin. We interpret this suite of features as evidence that the basin had a fundamental role in the development of the scarp. This influence could have been active or passive, depending on the relative time of the basin-forming impact event.

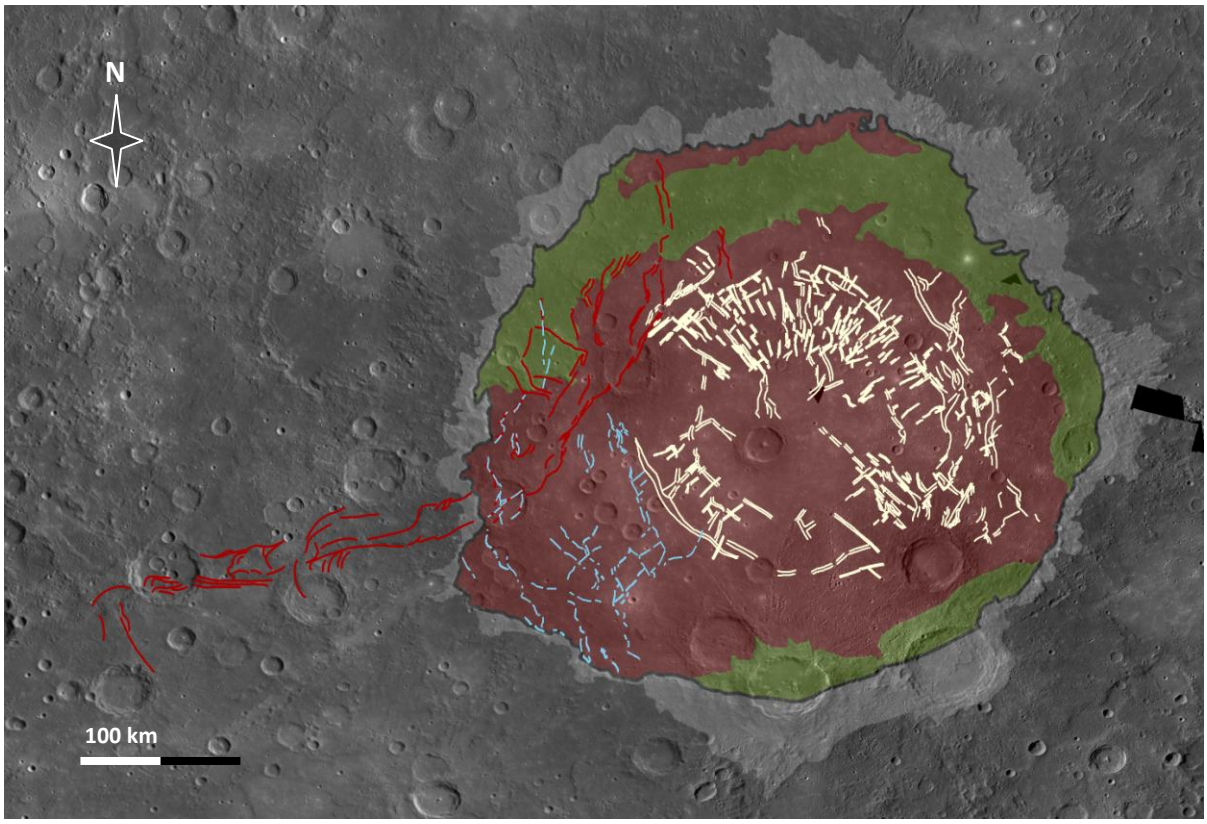

Fig. 1: Geological map of the Rembrandt basin and scarp system centered at 33°S, 81°E, on a MESSENGER MDIS mosaic at 250 m/px. Hummocky Area (green unit); Proximal Ejecta (pale grey unit); Inner Plains (red unit); Rembrandt scarp reverse fault system (red lines); basin-related structures (white lines); secondary features of uncertain origin (blue lines).

If the impact came before initiation of thrust faulting, it probably led to the generation of basin-related structures and an inhomogeneous crustal layering that passively influenced the development and final geometry of the scarp. On the other hand, if the impact event occurred during activity along the thrust, it could have led to a substantial change in the (regional) stress field as well as a local reworking of the structure. These effects could have induced changes in scarp vergence, the appearance of later strike-slip structures, and passive control of basin structures on scarp evolution.

4. Conclusion

The morphological and structural interpretation of MESSENGER flyby and orbital images (Fig. 1) and topography [10] has allowed us to study complex relationships between the Rembrandt basin and its through-going scarp. In particular, we find strong evidence for interaction between Rembrandt basin-scale and regional-scale stress fields, which have acted to influence the orientation and kinematic development of the Rembrandt scarp. Future analysis will focus on determining the sequence of formation for these features, i.e., whether the scarp predates or postdates the basin.

References

[1] S. C. Solomon et al. (2008) *Science*, 321, 59. [2] T. R. Watters et al. (2009) *Science*, 324, 618. [3] B. W. Denevi et al. (2009) *Science*, 324, 613. [4] S. L. Murchie et al. (2008) *Science*, 321, 73. [5] T. R. Watters et al. (2009) *EPSL*, 285, 283. [6] P. K. Byrne et al. (2012) LPS, 43, 1722. [7] R. G. Strom (1972) *Mod. Geol.*, 2, 133. [8] T. R. Watters et al. (2005) *Geology*, 33, 669. [9] P. K. Byrne et al. (2012) *LPS*, 43, 2118. [10] F. Preusker et al. (2011) *PSS*, 59, 1910. [11] S. Ferrari et al. (2011) *EPSC-DPS*, 963. [12] M. Massironi et al. (2012) *LPS*, 43, 1924.

Earth Moon Planets (2010) 107:267–297
DOI 10.1007/s11038-011-9378-3

Benefits of the Proposed Magia Mission for Lunar Geology

M. Massironi · L. Giacomini · S. Ferrari · E. Martellato · G. Cremonese · S. Marchi · A. Coradini

Received: 20 September 2010 / Accepted: 19 February 2011 / Published online: 10 March 2011

Abstract Age of geological units, surface mineralogical composition, volcanism, tectonics and cratering are major keys for unravelling the geodynamic and geological history of a planet. Thanks to the extensive exploration of the 1960s and 1970s and the compositional mapping of the 1990s missions (Galileo, Clementine and Luna Prospector), the Moon has a unique geological dataset among the extraterrestrial Solar System bodies. The recent and on-going missions, along with the future plans for lunar exploration, will together acquire an extraordinary amount of data. This should provide a solid basis to meet broad objectives like the constraints on the heterogeneity of Lunar composition and the presence of water deposits, the understanding of volcanic and tectonic evolution as well as more specific issues such as the genetic classification of volcanic domes, origin of the dark-halos craters, lava flow emplacement mechanisms, and the kinematics and deformational styles of tectonic structures. The Italian small mission MAGIA (Missione Altimetrica Gravimetrica geochImica lunAre) will be equipped with an integrated context camera and imaging spectrometer, a high resolution camera and a radar altimeter. The spatial and spectral resolution of these instruments will provide data products complementing past and ongoing Lunar mission data, particularly for the polar regions where a full resolution coverage is planned. A general review of some still unanswered questions on lunar surface

M. Massironi (✉) · L. Giacomini · S. Ferrari
Dipartimento di Geoscienze, Università di Padova, via Giotto 1, 35137 Padova, Italy
e-mail: matteo.massironi@unipd.it

M. Massironi · E. Martellato
CISAS, Università di Padova, via Venezia 11, 35131 Padova, Italy

G. Cremonese
INAF, Osservatorio Astronomico di Padova, Vicolo dell'Osservatorio 3, 35122 Padova, Italy

S. Marchi
Departement Cassiopée, Universite de Nice—Sophia Antipolis, Observatoire de la Côte d'Azur, CNRS, Nice, France

A. Coradini
INAF-IFSI, Via del Fosso del Cavaliere 100, 00133 Rome, Italy

Revision R1, November 5th

Olivine thermal emissivity under extreme temperature ranges: implication for Mercury surface

Helbert J. [1], Nestola F. [2,*], Ferrari S. [2], Maturilli A. [1], Massironi M. [2, 3], Redhammer G. J. [4], Capria M.T. [5], Carli C. [5], Capaccioni F. [5], Bruno M.[6]

(1) Institute for Planetary Research, DLR, Berlin-Adlershof, Germany
(2) Dipartimento di Geoscienze, Università degli Studi di Padova, Italy
(3) CISAS, Università degli studi di Padova, Italy
(4) Department of Materials Engineering & Physics, University of Salzburg, Austria
(5) IAPS-INAF Roma, Italy
(6) Dipartimento di Scienze della Terra, Università di Torino, Italy.

*Correponding author: fabrizio.nestola@unipd.it

Abstract

The work shows, for the first time experimentally and numerically, how the thermal emissivity spectra of a Mg-rich olivine (i.e. $Mg_{1.84}Fe_{0.16}SiO_4$, $Fo_{92}Fa_8$, with Fo = Mg_2SiO_4 and Fa = Fe_2SiO_4) significantly change as a function of temperature. An increase of 420 K modifies the olivine spectrum shifting in wavelength its emissivity features, simulating the spectrum of an olivine strongly enriched in iron (a Fa abundance increase from 8 to 20%). This "chameleon-like behaviour" indicates that the spectroscopic investigations of the surface of Mercury must take into account the local solar time dependency to properly infer the compositions of planetary materials by remote sensing acquisition of future space missions.

TECTONIC COMPLEXITY WITHIN VOLCANICALLY INFILLED CRATERS AND BASINS ON MERCURY. Paul K. Byrne[1], Christian Klimczak[1], David M. Blair[2], Sabrina Ferrari[3], Sean C. Solomon[1,4], Andrew M. Freed[2], Thomas R. Watters[5], and Scott L. Murchie[6]. [1]Department of Terrestrial Magnetism, Carnegie Institution of Washington, Washington DC, 20015, USA (pbyrne@dtm.ciw.edu); [2]Department of Earth, Atmospheric, and Planetary Sciences, Purdue University, West Lafayette, IN 47907, USA; [3]Dipartimento di Geoscienze, Università degli Studi di Padova, Padua, Italy; [4]Lamont-Doherty Earth Observatory, Columbia University, Palisades, NY 10964, USA; [5]Center for Earth and Planetary Studies, National Air and Space Museum, Smithsonian Institution, Washington DC, 20013, USA; [6]Johns Hopkins University Applied Physics Laboratory, Laurel, MD 20723, USA.

Introduction: The dominant form of tectonic deformation on Mercury is contractional. Extension is almost entirely restricted to impact craters and basins that host volcanic smooth plains [e.g., 1–4]. However, extensional and compressional tectonic landforms within those impact features vary enormously in structural complexity—from sets of graben that describe polygonal patterns in craters tens of kilometers in diameter [5] to collocated basin-radial, -circumferential, and -oblique graben and contractional wrinkle ridges within the 1,640-km-diameter Caloris basin [6].

Here we describe the progression in tectonic complexity from some of the smallest to the largest impact features on Mercury, together with the implications of recent numerical modeling for the Caloris basin in particular, and for impact basin formation, tectonics, and volcanism on the innermost planet in general.

Impact crater/basin tectonics: We include map patterns for tectonic structures within four representative volcanically flooded impact features on Mercury: (a) a "ghost crater," (b) the Mozart basin, (c) the Rembrandt basin, and (d) the Caloris basin (**Fig. 1**).

(a) Ghost crater. Ghost craters are impact features that have been entirely covered by lavas, their presence today marked by a ring of tectonic features localized above the buried crater rim [e.g., 2]. The crater in **Fig. 1a**, situated in the northern volcanic plains [7] and outlined by a ridge ring ~100 km in diameter, contains a set of graben with no preferred orientations that divide the plains infill into polygonal blocks [3]. The graben extend from the crater center to half its radius (r_{GC}). Contractional ridges external to the crater terminate at its peripheral ridge and do not penetrate the interior. This structural arrangement is characteristic of graben-bearing ghost craters, which primarily occur in the northern and circum-Caloris smooth plains [3,5].

(b) Mozart basin. The 235-km-diameter Mozart basin contains both graben and ridges, though these structures occur only within its peak ring [4] (**Fig. 1b**). Basin-circumferential graben form an annulus ~0.2–0.4 r_M concentric to the basin center. From this annulus to the peak ring at ~0.5 r_M, graben occur in a mix of basin-radial, -circumferential, and -oblique orientations. Ridges lie within the annular graben and show no preferred orientations. Structures are absent from the southwestern sector of basin infill within Mozart's peak ring. This general tectonic pattern is also observed within the peak rings of the similarly sized Raditladi and Rachmaninoff basins [4].

(c) Rembrandt basin. The 715-km-diameter Rembrandt basin is riven by a northeast–southwest-trending 1,000-km-long array of scarps interpreted to be a fold-and-thrust belt (FTB) [6]. Apart from the FTB, however, the basin floor is heavily deformed by extensional and contractional structures [8,9] (**Fig. 1c**). Col-located basin-radial sets of graben and ridges form a fan-like pattern centered on the basin outward from ~0.2 r_R and are bounded by circumferential ridges at ~0.5 r_R (and circumferential graben along the northern portion of the ridges). Local clusters of ridges without preferred orientations occur in the southwestern and eastern basin interior beyond ~0.5 r_R [9].

(d) Caloris basin. The largest impact basin recognized on Mercury also hosts the most tectonically deformed smooth plains on the planet, Caloris Planitia [6] (**Fig. 1d**). A basin-radial graben set, Pantheon Fossae [e.g., 1], the dominant extensional assemblage in the basin, originates from a point near the center and extends to ~0.55 r_C. Pantheon Fossae is bounded by circumferential graben that form a near-complete annulus from ~0.45 to 0.55 r_C. Outward, extension is manifest by basin-oblique graben that define a complex polygonal map pattern and steadily decrease in width, depth, and length towards the basin margin [6].

Basin-circumferential ridges are the most abundant type of contractional structure, and extend from ~0.1 to 0.7 r_C. Radially orientated ridges also occur within this zone but are less common than their Caloris-concentric counterparts. Outside ~0.7 r_C, ridges show no orientation preference and so also form a polygonal pattern that becomes less prominent toward 1.0 r_C [6].

Formation hypotheses: Almost every tectonically deformed impact structure on Mercury is characterized by a scarcity of definitive cross-cutting relations, challenging recognition of a developmental sequence for attendant structures. Where ridges and graben spatially coincide within ghost craters, their superposition relations are often unclear [3]; they do not coincide in Mozart at all [4]. Extensional structures appear to be superposed on, and so postdate, contractional landforms

in Rembrandt and Caloris [e.g., 1], but no clear dip- or strike-slip offsets are observed in either basin.

However, finite-element modeling results for ghost craters [10] and mid-sized basins such as Mozart [4] may provide insight into the deformation that shaped Rembrandt and Caloris. Thermal contraction of thick, rapidly emplaced lava flows produces horizontal extensional stresses that favor the formation of mixed-orientation graben in volcanic plains, whereas horizontal shortening in response to cooling and contraction of the planet's interior or flexure due to volcanic loading was likely responsible for the formation of ridges in both ghost craters and Mozart basin [2,4,10]. Moreover, models of thermally contracting lavas also show that a buried basin ring strongly localizes radial extensional stress and circumferential graben formation [4].

Implications: Previous studies suggested that the prominent fossae within Caloris may have formed due to dike propagation [11] or to flexural uplift of the basin center, in response either to the volcanic emplacement of the circum-Caloris smooth plains [12] or to inward flow of the lower crust [13]. No extensive plains are observed exterior to Rembrandt [14], suggesting intrusive activity or inward crustal flow may be responsible for the fossae in at least that basin. Graben of mixed orientation in Caloris and Rembrandt may attest to near-isotropic horizontal extension of rapidly emplaced lavas; the decrease in graben size with increasing distance from the basin center likely indicates steadily reducing plains thickness [5,10] and thus original basin depth. If the pronounced circumferential graben within these basins reflect extension above a buried basin ring, Rembrandt and Caloris may be multi-ring basins—a class of impact feature not yet clearly documented for Mercury [15]. Finally, the ridges within these basins may primarily be the result of global contraction on Mercury. If so, the differences in orientation from basin-circumferential or -radial to -oblique could reflect a transition of the responsible stress field from strongly basin–shape-influenced to horizontally isotropic with increasing distance from basin center.

Informed by new tectonic maps of Caloris and Rembrandt (**Fig. 1**), these inferences can be tested numerically in the manner of recent models for ghost craters and basins [4,12], with the goal of reproducing the full range of tectonic complexity within flooded impact features on Mercury.

References: [1] Murchie S. L. et al. (2008) *Science*, *321*, 73. [2] Watters T. R. et al. (2009) *EPSL*, *285*, 309. [3] Watters T. R. et al. (2012) *Geology*, *40*, 1123. [4] Blair D. M. et al. (2013) *JGR*, *118*, in press. [5] Klimczak C. et al. (2012) *JGR*, *117*, E00L03. [6] Byrne P. K. et al. (2012) *LPS, 43*, abstract 1722. [7] Head J. W. et al. (2011) *Science*, *333*, 1853. [8] Watters T. R. et al. (2009) *Science*, *324*, 618. [9] Ferrari S. et al. (2012) *EPSC Abstracts*, *7*, abstract 2012-874. [10] Freed A. M. et al. (2012) *JGR*, *117*, E00L06. [11] Head J. W. et al. (2008) *Science*, *321*, 69. [12] Freed A. M. et al. (2009) *EPSL*, *285*, 320. [13] Watters T. R. et al. (2005) *Geology*, *33*, 669. [14] Denevi B. D. et al. (2012) *EPSC Abstracts*, *7*, abstract 2012-812. [15] Fassett, C. I. et al. (2012), *JGR*, *117*, E00L08.

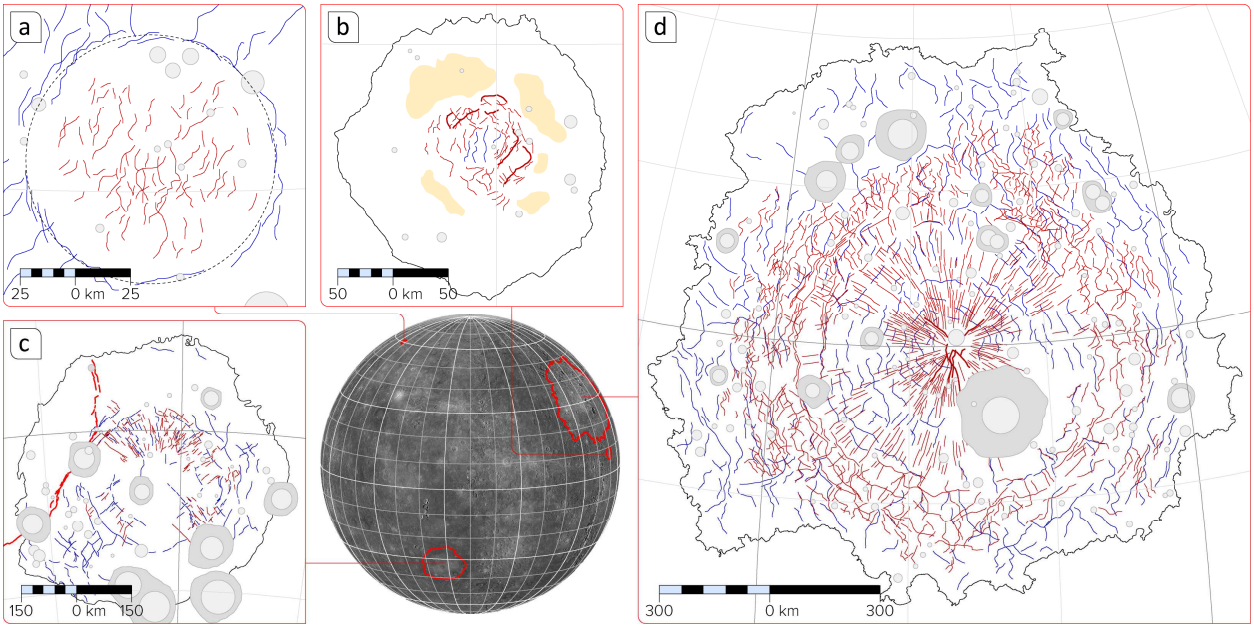

Figure 1. Structural sketch maps of exemplar flooded impact features.(a) Ghost crater; (b) Mozart basin; (c) Rembrandt basin (after [9]); and (d) Caloris basin. Orthographic projections centered at: (a) 60.3°N, 36.7°E; (b) 7.8°N, 169.6°E; (c) 33.5°S, 88°E; and (d) 30°N, 161°E. Sketches feature graben (dark red lines), ridges (dark blue), superposed craters and ejecta (light and dark grey), and Mozart peak ring (sand).

Asia Oceania Geosciences Society, 10th Annual Meeting - 24 to 28 June 2013
Brisbane Convention & Exhibition Centre, Australia

Mineral Phases in Mercury's Surface Regolith from mid-infrared measurements

Ann Sprague[1], Jorn Helbert[2], Alesandro Maturilli[2], Sabrina Ferrari[3] and Frabrizio Nestola[3].

[1]Lunar and Planetary Laboratory, The University of Arizona, Tucson, Arizona, US
[2]Institute for Planetary Research, DLR, Berlin-Adlershof, Germany
[3]Dipartimento de Geoscienze, Universita degli Studi di Padova, Italy

Mid-infrared spectroscopic data of Mercury's surface are studied to identify mineral phases present in surface rocks and minerals. Spectra were obtained with the Mid-InfraRed Spectrometer and Imager (MIRSI), a camera system built at Boston University for ground-based observing. Observations were made at NASA's Infrared Telescope Facility (IRTF). When used on the IRTF MIRSI has a plate scale of 0.27 arc seconds per pixel and a field of view large enough to include Mercury's Earth facing disk. The optics provide diffraction-limited spatial resolution and a spectral resolving power of $\lambda/\Delta\lambda$ of 200 in the 7 to 14 μm spectral range. Three spectra from Mercury's surface are compared to individual and linear combinations of laboratory spectra obtained at the Planetary Emissivity Laboratory (PEL) in Berlin, Germany During the last five years a suite of chemically characterized rock and mineral samples (grain sizes 0-25 μm, 25-63 μm, 63-125 μm and 125-250 μm) have been measured in a vacuum environment at temperatures comparable to the known temperatures of Mercury's surface (300 to 700K). Heating and cooling of samples results in slight volume changes of crystalline lattice structures and results in small shifts in the wavelength of major and minor spectral features within the measured spectrum. The spectral features are well known to be associated with the specific elemental cations present in the lattice (Mg, Fe, Ca, etc.) and their relative concentration. The wavelengths of emissivity maxima and minima associated with composition are documented for spectra obtained at room temperature and pressure, usually in a spectrometer using a nitrogen purge. Here we compare Mercury's surface spectra to the new, spectral library appropriate for Mercury's temperature and pressure. Results provide an opportunity to predict what the MERcury Radiometer and Thermal infrared Imaging Spectrometer (MERTIS) on the ESA-JAXA mission BepiColombo will achieve.